216 + 120 Fast Reactor
11-20-69 A+B Format

PLR

1097

AI-AEC-12767

MASTER

STUDIES OF BOILING INITIATION FOR SODIUM FLOWING IN A HEATED CHANNEL

AEC Research and Development Report

Atomics International
North American Rockwell

DISCLAIMER

Printed in the United States of America
Available from
Clearinghouse for Federal Scientific and Technical Information
National Bureau of Standards, U.S. Department of Commerce
Springfield, Virginia 22151
Price: Printed Copy $3.00; Microfiche $0.65

AI-AEC-12767
REACTOR
TECHNOLOGY

STUDIES OF BOILING INITIATION FOR SODIUM FLOWING IN A HEATED CHANNEL

By

D. LOGAN
C. J. BAROCZY
J. A. LANDONI
H. A. MOREWITZ

Atomics International
North American Rockwell

CONTRACT: AT(04-3)-701
ISSUED: SEPTEMBER 30, 1969

DISTRIBUTION

This report has been distributed according to the category "Reactor Technology" as given in the Standard Distribution for Unclassified Scientific and Technical Reports, TID-4500.

ACKNOWLEDGMENT

The authors are grateful for the significant contributions made to this work by L. M. Haba, who performed loop operation and assembly, data acquisition, and assisted in data reduction; R. L. Randall, for development of the boiling detection systems and associated equipment; A. G. Pard, for preparing heater surface replicas and electron microscope stereo photographs; and Dr. Louis Bernath for many useful suggestions and stimulating discussions.

CONTENTS

CONTENTS

TABLES

FIGURES

FIGURES

FIGURES

ABSTRACT

Data are presented for incipient boiling superheat for sodium flowing upward in a vertical annulus formed by a heated stainless steel tube of 1/4-in. diameter located inside a tube of 1/2-in. diameter. The data cover the following ranges: heat flux, 0.09×10^6 to 0.825×10^6 Btu/hr-ft^2; pressure, 2 to 15 psia; inlet subcooling, 20 to 300°F; sodium velocity, 2 to 6 ft/sec; and wall superheat, 0 to 241°F. All-liquid heat transfer relationships permit clear identification of the major trends due to heat flux, velocity, and inlet subcooling and thereby allow improved interpretation of the incipient boiling data.

The application of various boiling inception theories to forced convection, liquid metal systems is examined and evaluated. For the maximum observed superheats, consideration of the dominant physical forces results in a dimensionless plot of wall superheat vs Reynolds number and shows the trends to be expected for forced convection laminar and turbulent flow in LMFBR systems.

THIS PAGE

WAS INTENTIONALLY

LEFT BLANK

I. INTRODUCTION

The occurrence of boiling, under certain flow and/or power conditions in a Liquid Metal Cooled Fast Breeder Reactor (LMFBR) can potentially initiate a major accident through the increase in reactor power caused by the insertion of positive reactivity associated with coolant voiding. However, the analysis of boiling and two-phase flow of sodium depends upon data in which large apparent discrepancies exist in the values reported for boiling initiation superheat,[1] for void fraction,[2] and for measured and predicted values of two-phase flow pressure drop.[3] In addition, the bulk of the incipient boiling superheat data[1] has been obtained under conditions which do not even remotely resemble those existing in a Liquid Metal Fast Breeder Reactor (LMFBR).

The boiling inception theories developed to date either have serious shortcomings or do not apply to liquid metals. For example, Hsu's thermal criterion[4] requires a pronounced temperature gradient through the growing bubble whereas in sodium at high heat fluxes, the growing bubble is in a virtually isothermal environment. As other examples, boiling inception theories dependent on "Trapped Gas in Cavity Models" such as those advanced by Holtz,[5] Chen,[6] and Dwyer,[7] emphasize the initial presence of non-condensible gas in the active cavity. Recent corrosion experiments,[8] however, show that flowing sodium at 1200°F removes the "as received" surface of Type 304 stainless steel tubing in several hundred hours, leaving the surface grains highly polished, and produces conical etch pits (40 to 80 μin. in diameter and depth) in the grain boundaries. As a result of this thorough wetting, the effect of non-condensible gas in the cavity, on boiling inception, in flowing sodium should be negligible. These theories[5, 6, 7] also ignore the possible influence of heat flux and fluid velocity on incipient boiling superheat despite substantial experimental evidence of this influence. For incipient boiling of sodium, examination of the relative magnitude of bubble drag, surface tension, and buoyant forces indicates that wall superheat and bubble size can be expected to be strongly influenced by fluid velocity in turbulent flow.

Thus, to provide a more realistic basis for safety analysis of LMFBR's, there are requirements both for obtaining accurate, reliable data and for developing an improved model of the incipient boiling of sodium under conditions

approaching those of LMFBR operation. Such an investigation has been made on forced convection, sodium boiling initiation superheat utilizing electrically powered, high flux heaters which simulate the thermal and hydraulic characteristics of LMFBR fuel pins.

II. EXPERIMENTAL APPARATUS

A. INTRODUCTION

To obtain meaningful superheat data for LMFBR design use, certain experimental conditions are necessary. The heating surface must be of the same material and geometry as used in the LMFBR, and the heat transfer to the sodium must take place at a discrete surface. The surface heat fluxes must be at least 0.5×10^6 Btu/hr-ft^2 at a boiling temperature of about 1800°F. The all-liquid sodium velocity in the flow passages must be 5 to 30 ft/sec. The physical condition of the heating surface must be known and be related to the incipient boiling superheat data. The wall superheat (heating surface wall temperature minus sodium saturation temperature) should be measured directly.

The present single channel experiment meets the material, pin geometry, and heating mode requirements, but does not meet the general multi-channel geometry requirement. The heat flux requirement is exceeded and temperatures of up to 1600°F are reached. Velocities of up to 6 ft/sec are attained. During the experiment, periodic examination and stereo-photographs of electron microscopy projections of replicas of the heating surfaces have been performed and related to superheat data. The heated surfaces do not have attached thermocouples or other artificial boiling sites. Though the experiment uses pressure measurement techniques to determine sodium saturation temperature, the absence of heating surface thermocouples requires the use of the all-liquid film coefficient to calculate the wall temperature, and hence the wall superheat.

B. FORCED CONVECTION LOOP

The performance characteristics of the Forced Convection Loop were established by the requirements discussed in A, above, to create conditions representative of those that could exist during boiling in an LMFBR, within the limits of experimental technology. The present loop was developed from an existing loop used in forced convection boiling studies.[9][10]

The Forced Convection Loop shown in Figures 1 and 2 is composed of a pump, economizer, preheater, test section, high flux heater, condenser, subcooler, and cold trap. The principal features of the loop are listed below:

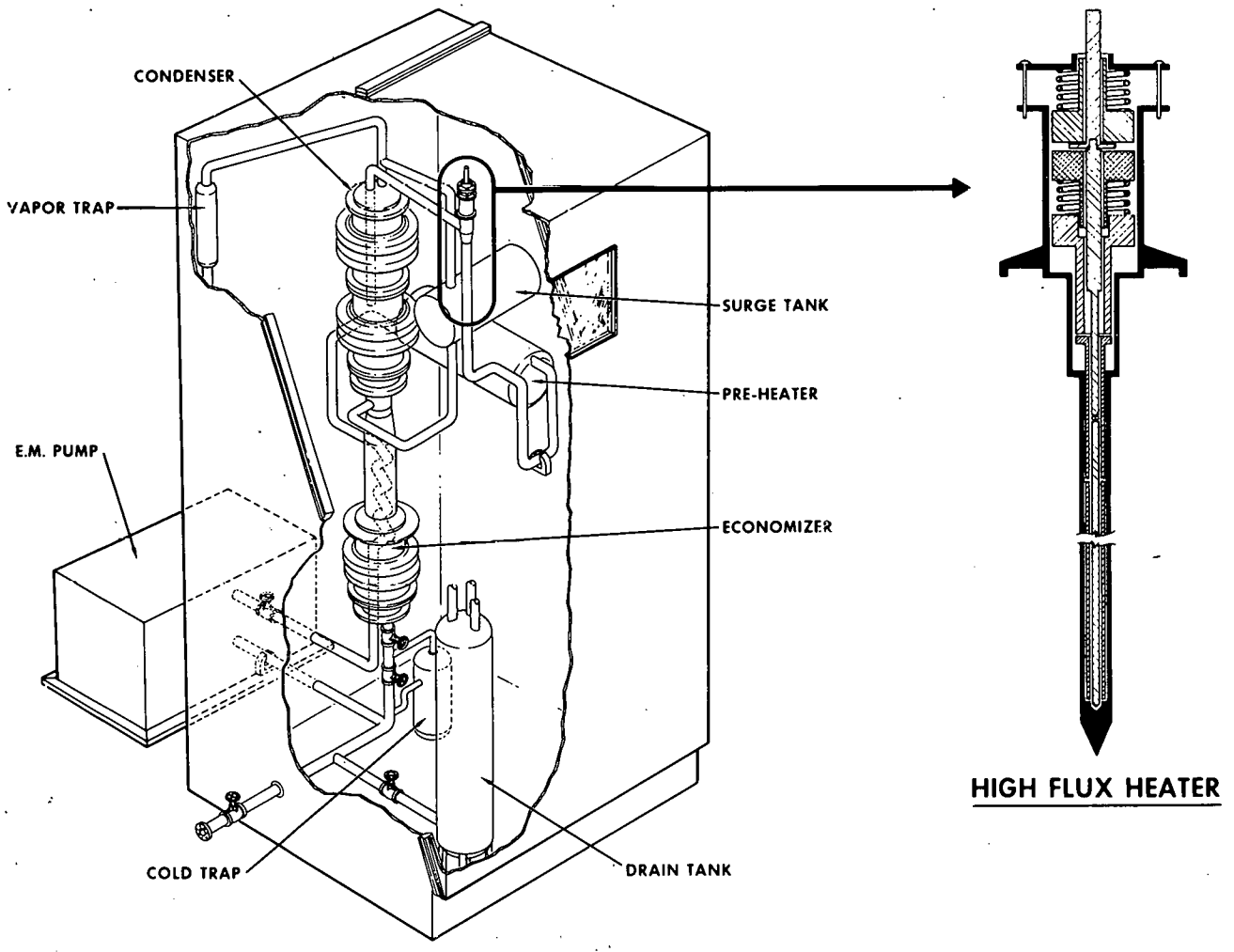

9-JA10-005-33

Figure 1. Forced Convection Loop Schematic

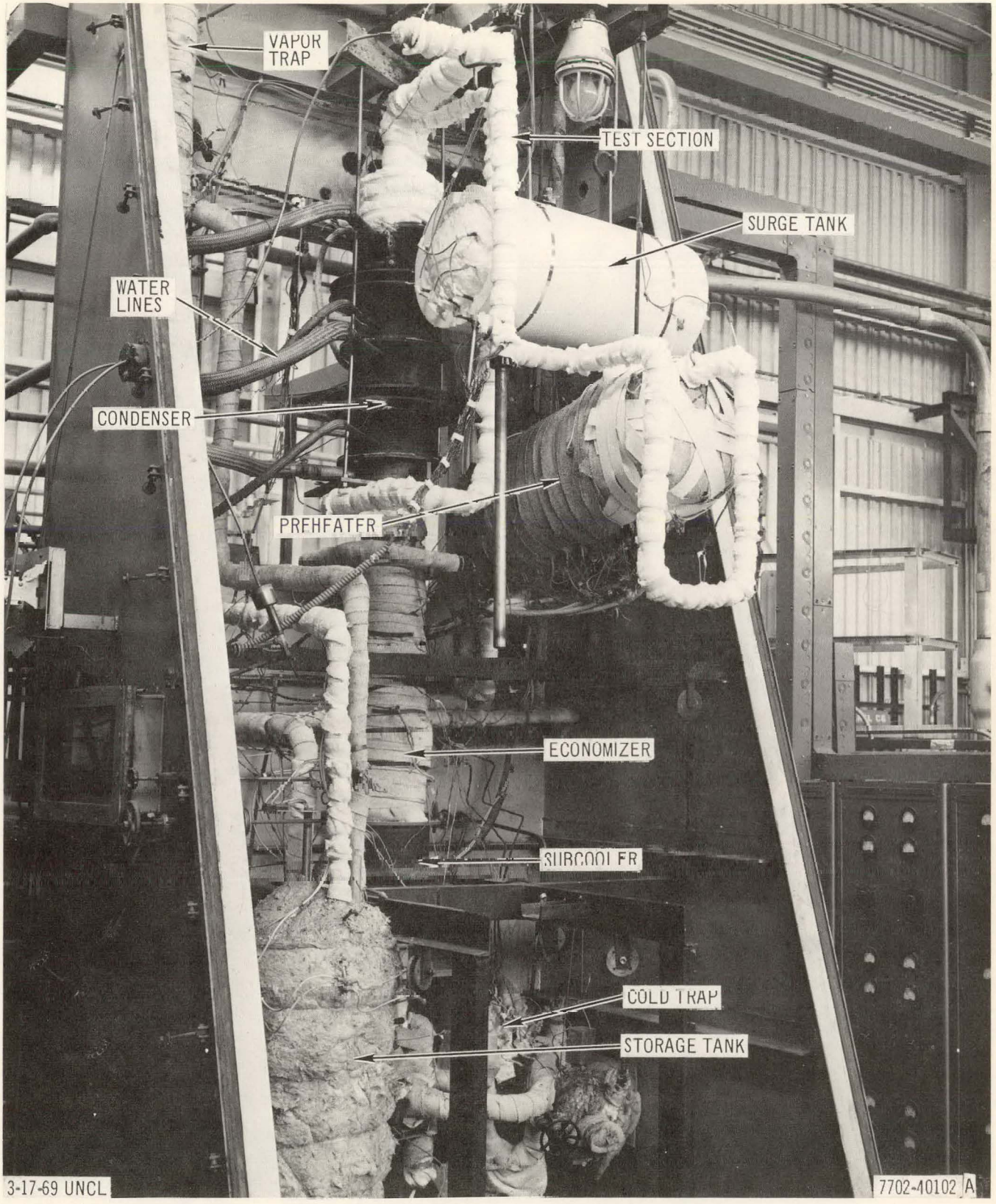

Figure 2. Forced Convection Loop

Material	
Loop, most components, and high flux heater cladding	Type 304 Stainless Steel
Preheater, subcooler, and some original piping	Type 347 Stainless Steel
Flow Rate	16 gpm maximum
Sodium Temperature	1850°F maximum
Maximum Heat Flux	1×10^6 Btu/hr-ft^2

Temperature, flow rate, pressure, and electrical power are measured and monitored at various locations.

1. Pump

Heat transfer loops in which boiling occurs tend to be hydrodynamically unstable. To stabilize the system, a large steady pressure drop is provided by a high-pressure pump and a throttling valve. The pump assembly, shown in Figure 3, consists of two electromagnetic, multipass, linear-induction pumps connected in series; it is designed to produce 200 psi at 6 gpm, using a 3-phase, 230-volt power supply. Each pump consists of two 18-in. long by 6 in. deep

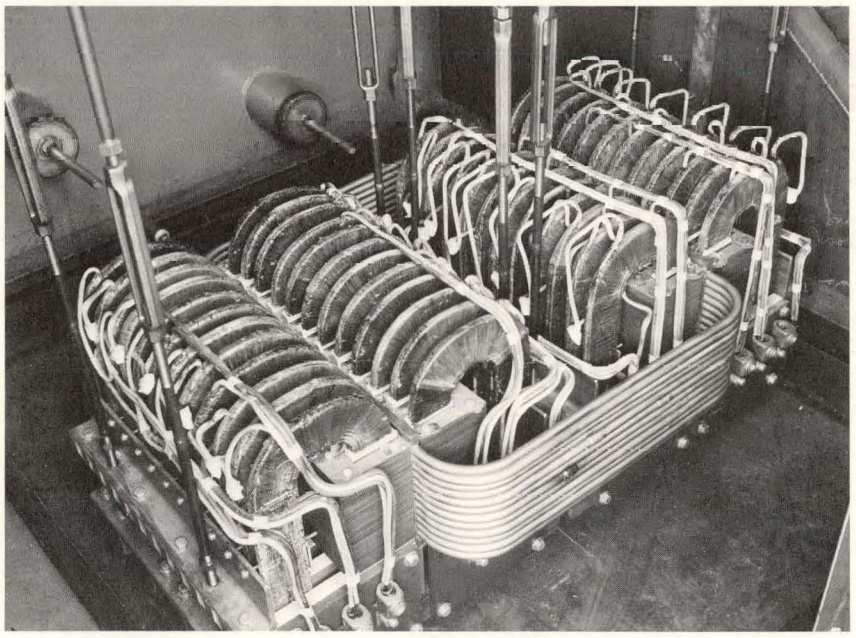

7519-54441

Figure 3. Electromagnetic Pump

stators positioned about the throat. This throat, or pumping section assembly, is constructed of two parallel Type 304 stainless steel tubes, 1/2-in. OD by 0.028-in. wall, wound into a six-pass rectangular coil, 26 in. long by 21 in. wide and brazed together in the pumping region with high-temperature nickel braze alloy. Nickel wires are brazed into the cusps between the tubes in the throat region, and nickel plated copper bars are brazed on the top and bottom of the throat to provide external return paths for induced eddy currents. The sodium flow, on entering the throat, splits into two parallel paths at the suction nozzle and rejoins on leaving the pump. The stator assemblies, mounted on aluminum bases, are freely suspended to allow free movement between the pump components during thermal expansion. To improve the power factor and to balance this highly inductive load, 3-phase capacitors are connected across the pump. Figure 4 shows the head developed by the pump and its efficiency as a function of flow rate.

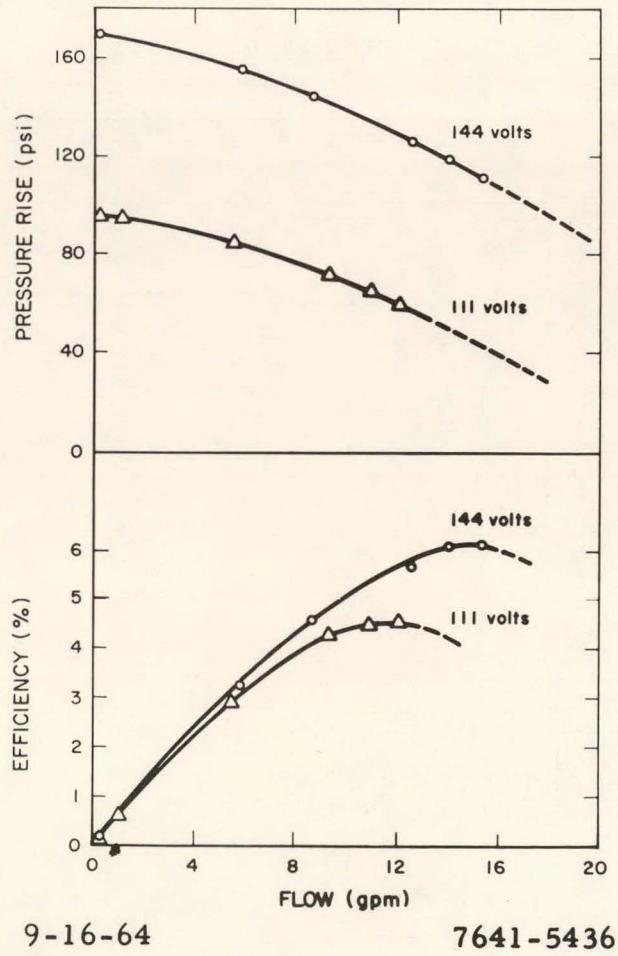

Figure 4. Performance Curves for the Multipass Linear Induction Sodium Pump at 750°F

2. Main Heat Exchanger and Preheater

The main heat exchanger consists of a condenser, an economizer, and a subcooler.

The A condenser, shown in Figure 5, was used for all the experimental runs through KC 25 and was constructed so that the sodium entered the top of the condenser and fell approximately 2 ft through the argon cover gas before reaching the surface of the sodium pool in the condenser. The A condenser design was such that gas entrainment could be anticipated as the flow rate increased. To reduce the probability of gas entrainment, a new condenser (B of Figure 5) was designed and installed in the loop and was used on all runs after KC 25. The B condenser is constructed so that the hot sodium entering the condenser is released below the surface of the sodium pool through 48-1/2 in. diameter transverse holes in a vertical 2-in. diameter pipe. In both condenser arrangements, the heat is removed by a close fitting, water-cooled, outer container. Heat transfer across the narrow annular gap between the outer container and the inner container of the condenser is by means of radiation and forced convection of argon.

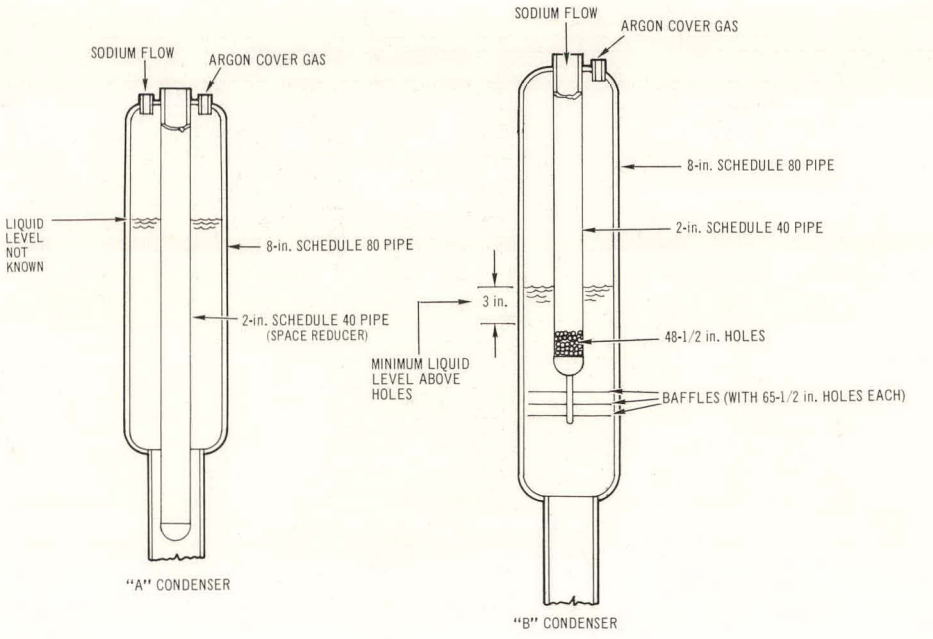

Figure 5. "A" and "B" Condensers

The countercurrent flow economizer, consisting of a coiled tube inside an annulus, is used to cool the sodium entering the subcooler while heating the sodium entering the preheater.

The subcooler consists of an inner and an outer container. The design of the water-cooled outer container is similar to that of the outer container of the condenser. In the inner container, the sodium flows in an annulus which has a stagnant air space in the center. The purpose of the subcooler is to insure that the temperature of the sodium entering the pump is below 750°F and to thereby provide sufficient subcooling to prevent cavitation at the pump entrance.

The pool type preheater, shown in Figure 6, can dissipate 80 kw into the flowing sodium. Inlet and outlet lines are located near the top at opposite ends of the vessel. The preheater is constructed from a Schedule 60 type 347 stainless steel pipe section, 26 in. long x 12 in. in diameter, which is welded to two pipe end caps. This vessel is suspended by two hangers welded to its top and is positioned at a 15° angle to the horizontal to permit easy draining through a bottom tap. Twenty-five 3750 watt, Inconel sheathed, immersion heaters are welded to the bottom of the vessel. These heaters are attached through specially

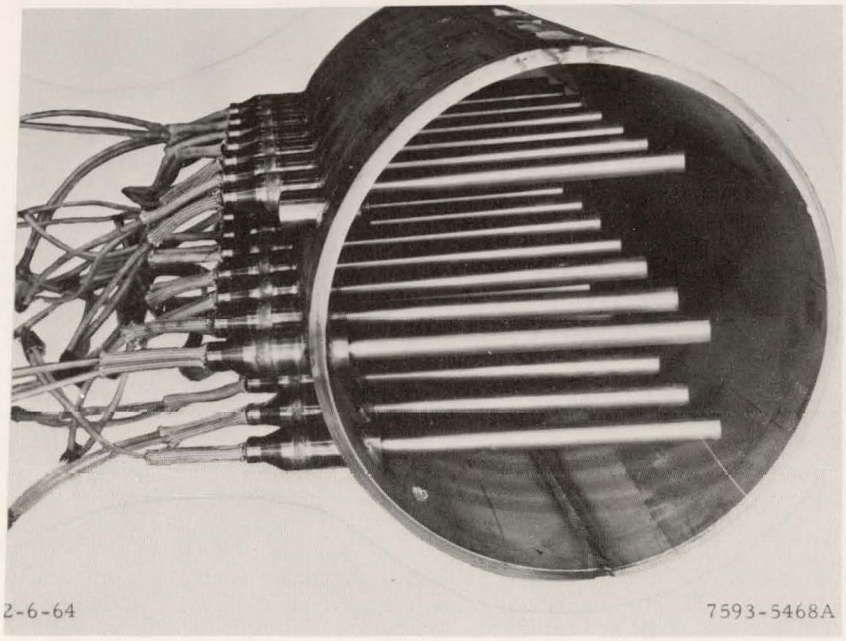

Figure 6. Sodium Preheater

designed fittings to allow replacement of burned out units; they are welded at a true vertical position to insure uniform vapor release from the heater surface and to prevent heater burnout from vapor blanketing. The power to the heaters is provided by a variable transformer.

3. Cold Trap

The cold trap shown in Figure 7 is designed so that its temperature gradient can be controlled by circulating ethylene glycol through a coil which is bonded with Thermon to the outside of the cold trap. The glycol is circulated from a storage vessel that can be heated or cooled. Control of the cold trap temperature gradient permits variation of the oxide level in the loop. During the experiments, the cold trap was usually operated at 245°F, thus ensuring an oxygen concentration of ~3 ppm.

4. Instrumentation

a. Data Acquisition

Temperature, flow, pressure, heater current and heater voltage signals are scanned, digitized, converted to engineering units and recorded on a line printer or magnetic tape by a centralized data acquisition system. Analog signals in the range from zero to ±100 mv are coupled by direct cable to the data logger through a remote data gathering box which has 25 sequentially scanned channels. The heater current shunt and the thermocouples at the upper edge of the heated zone require high scan rates, so each is connected to five different channels. They are thus recorded five times as often as instrument outputs connected to a single channel. The data logger can scan and record data on magnetic tape at the rate of 25 bits every 3-1/2 seconds. When using the line printer, the scan rate is 25 bits every 6-1/2 seconds.

As shown in Table 1, the arithmetic section of the data logger,* is programmed to provide direct conversion of instrument signals to engineering units, enabling direct on-line evaluation of test data and simplifying data analysis.

The analog signals in the range of ±100 mv are measured with a resolution of 0.01 mv. In the case of non-linear sensors, such as thermocouples, an

*Beckman Instrument Co., Model 210 Data Logger

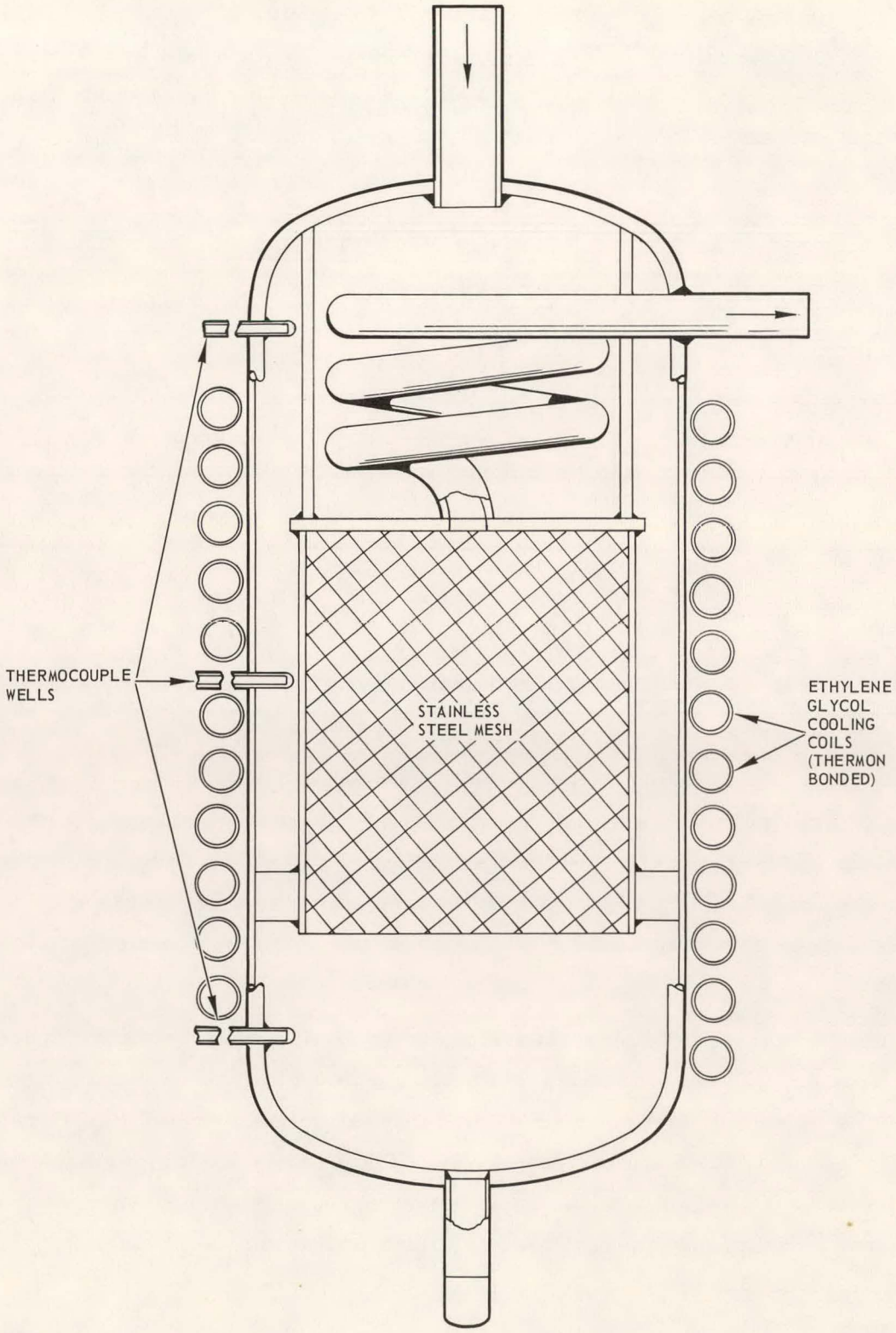

Figure 7. Cold Trap Schematic

internal comparator automatically selects the appropriate scale and offset factors for each voltage level. The measured value, with scale and offset correction, is then recorded with 4-digit resolution on the line printer or magnetic tape. Readout resolution for the various measurements are shown in Table 1.

TABLE 1
READOUT RESOLUTION

Measurement	Range-Resolution	Nominal Accuracy*
Temperature (°F)	9999	±4°F
Flow (mv)	99.99	±0.05 mv
Voltage (v rms)	999.9	±0.5 ± 1% of value†
Current (amp rms)	999.9	±0.5 ± 1% of value†
Pressure (psia)	99.99	±0.05 ± 1% of value†

*Depends also on scan rate and time dependence of sensor output
†Limited by accuracy of signal conditioning converters

b. Boiling Detector and Heater Protection System

Several boiling detectors are used to protect the high flux heater from burnout due to vapor blanketing and to indicate the onset of boiling.* One detector consists of an electronic circuit which analyzes signals obtained from the electromagnetic (EM) flowmeter located at the inlet of the test section. These signals are amplified, filtered, and coupled to a rate- and level-sensing comparator which trips a relay, cutting off power to the high flux heater after a selected time delay.

A second boiling detector uses signals from an accelerometer† mounted on the test section. These signals are amplified and filtered to discriminate against background noise and are coupled to an integrating circuit and comparator as well as to a loudspeaker in the test area. The circuit is designed to cut off heater power within 2 or 3 seconds if the integral of sound intensity exceeds a preset limit. Spurious intermittent acoustic emissions associated with temperature changes do not trip the comparator.

*An earlier version of the EM boiling detector is described in References 11 and 12; a detailed description of boiling detector development is in Reference 13.
†Endevco Model 2235M-10 Accelerometer.

A third boiling detector uses the signal from an electronic pressure transducer.* The signal is amplified, filtered with a high pass filter, and coupled to a comparator. Pressure transients observed at the outlet of the test section at the onset of boiling are damped sinusoids at about 6 cps. The NaK-filled coupling lines, the bellows, and the mechanical linkage to the ferrite cam detector combine to act as a band pass filter which responds with high sensitivity to void formation. The comparator cuts off heater power if the oscillations on the observed pressure signal exceed a preselected threshold.

These devices permit the heater to operate without danger of burnout caused by surface boiling at power levels comparable to, or in excess of, those of a LMFBR fuel element. If the heater were allowed to operate at full power during surface boiling conditions, the temperature would rise at rates approaching 1800°F/sec. (Prior to the installation of this boiling detector circuitry, heater failure usually occurred within one to five boiling tests. However, with the aid of this boiling detection system, more than 150 successful sodium boiling tests under various flow, power, and pressure conditions were carried out with each of several high flux heaters.)

In addition to the boiling detectors, a current-rate-change system is also used to detect sudden changes in heater electrical resistance, which would indicate failure or electrical breakdown of the insulation material. In this system, the signal from the ammeter shunt, which is in series with the high flux heater, is rectified, filtered, differentiated, and coupled to a comparator. This circuit is designed to detect sudden changes in the current applied to the heater under test. The system automatically trips input power if heater current changes by more than 5% of full scale at a rate exceeding about 10%/sec. Response time, including power relay, is less than 50 msec. The use of a current-sensing detector permits a single sensitivity setting to be used for a graphite heater of any length. The various components of the heater protective system are summarized in Table 2.

5. Test Section

The test section consists of an annular passage formed by two concentric Type 304 stainless steel tubes. The 0.250-in. OD inner tube is the sheath of

*Barton Model 296 Absolute Pressure Transducer

TABLE 2

HEATER PROTECTION SYSTEM

Events	Problems	Sensors	Methods of Detection
Boiling in test section simulating LMFBR fuel element and flow channel	Burnout of electrical heater, partial channel blockage during transient boiling tests	EM flow meter at inlet to test section	Rate of change of noise amplitude in 1 to 10-cps band
		Accelerometer mounted on test section	Rate of change of integral of noise amplitude in 1 to 3-kc band
		Pressure at outlet of test section	Amplitude of noise in 1 to 10-cps band
Electrical breakdown of ceramic insulation in high flux heaters	Heaters burn in two, destroying evidence of failure mechanism and damage instrumented test section	Current	Rate of change of 60-cps heater input current

the high flux heater. The outer tube is 0.75-in. OD with a 0.120-in. thick wall through which the thermocouples, pressure taps, and heater centering pins are mounted. Figure 8 shows the test section used before Run B22; however, except for an increased number of instrumentation penetrations, the construction and general appearance of the most recent test section is very similar to the one shown.

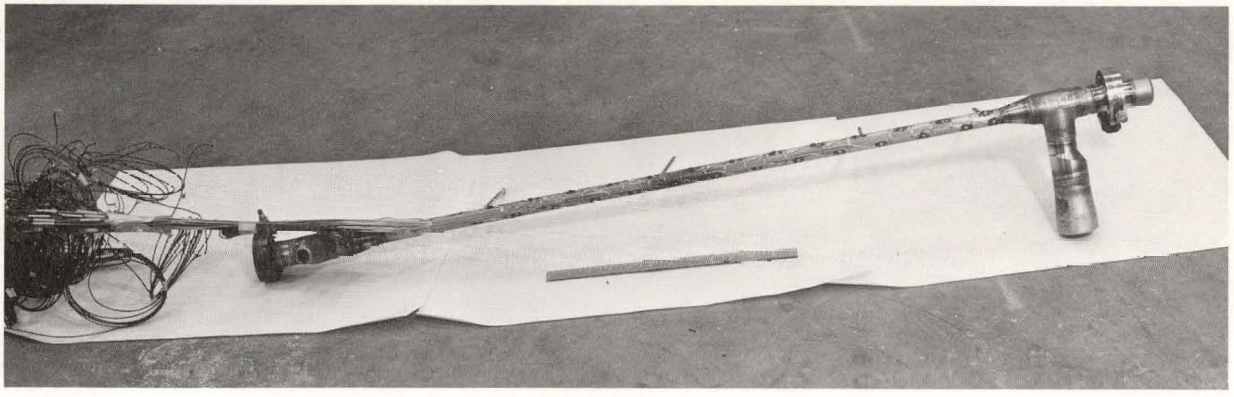

7702-4003

Figure 8. Sodium Liquid Superheat Test Section

The heater is centered in the test section by 12 centering pins the locations of which are shown in Figure 9. Four pins are located 90° apart, 3/4 in. above the heated zone of the heater. Two pins are located 180° apart, 4-1/2 in. below the upper edge of the heated zone. Two other pins are located 180° apart, 6-1/2 in. below the upper edge of the heated zone and are rotated 90° from the pins at the 4-1/2 in. position. Four pins are located 90° apart, 14 in. below the upper edge of the heated zone. When originally fabricated, the centering pins had essentially zero clearance from a heater which was nearly perfectly centered. After many boiling transients, an estimated 2-mil clearance developed between the centering pins and the heater.

Several pressure taps are built into the test sections, but only one tap was used throughout all the tests. This tap is located 1/2 in. above the downstream edge of the heated zone of the heater and is a drilled hole, 0.152-in. in diameter. Figure 10 shows a typical thermocouple and pressure tap installation as well as the upper part of the test section.

There are 27 chromel-alumel thermocouples (0.062-in. diameter, Type 304 stainless steel sheath) in the test section. The thermocouples are installed through the test section wall so that they probe 1/16 in., ±5 mils, into the sodium annulus surrounding a heater. Table 3 lists the location of each thermocouple.

6. High Heat Flux Heater

In its present developmental state, the high flux, electrically powered heater shown in Figure 11 is fabricated by project personnel. It is a replaceable element that produces a uniform heat flux of known magnitude ($>10^6$ Btu/hr-ft^2) at sodium temperatures of 1600°F. The main components of the heater consist of a body assembly, Type 304 stainless steel sheath, graphite heating element, boron nitride insulating sleeve, and electrode. The boron-nitride sleeve is slip-fitted into the sheath and insulates all but the grounded end of the graphite heating element from the sheath. A spring-loaded electrode, which is maintained in alignment by insulated bushings, permits an input of up to 48 kw of ac power to a 30-in. long heater. The sodium at the grounded end of the electrode provides a short current return path to the outer wall of the test section.

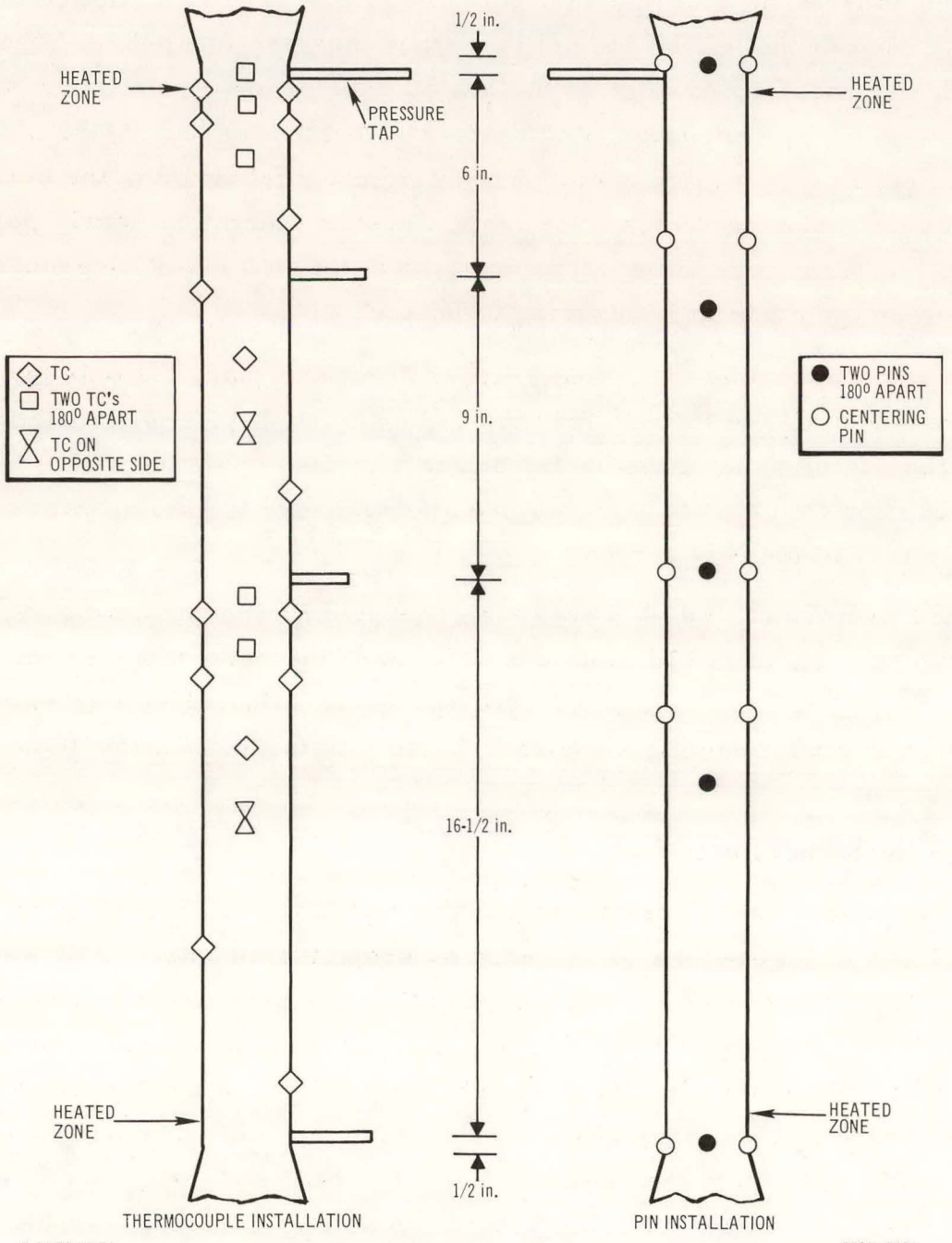

Figure 9. Centering Pins and Thermocouple Locations on Test Section

TABLE 3

THERMOCOUPLE LOCATIONS

Thermo-couple	Inches From Upper Edge of Heated Zone	Degrees Rotated From Pressure Taps
1	1/2 above	90
2	1/2 above	270
3	0	0
4	0	180
5	1/2 below	90
6	1/2 below	270
7	1 below	0
8	1 below	180
9	2 below	90
10	2 below	270
11	4 below	0
12	6 below	180
13	8 below	270
14	10 below	90
15	12 below	0
16	15 below	90
17	15 below	270
18	15-1/2 below	0
19	15-1/2 below	180
20	16-1/2 below	90
21	16-1/2 below	270
22	17-1/2 below	0
23	17-1/2 below	180
24	19-1/2 below	270
25	21-1/2 below	90
26	25-1/2 below	180
27	29-1/2 below	0

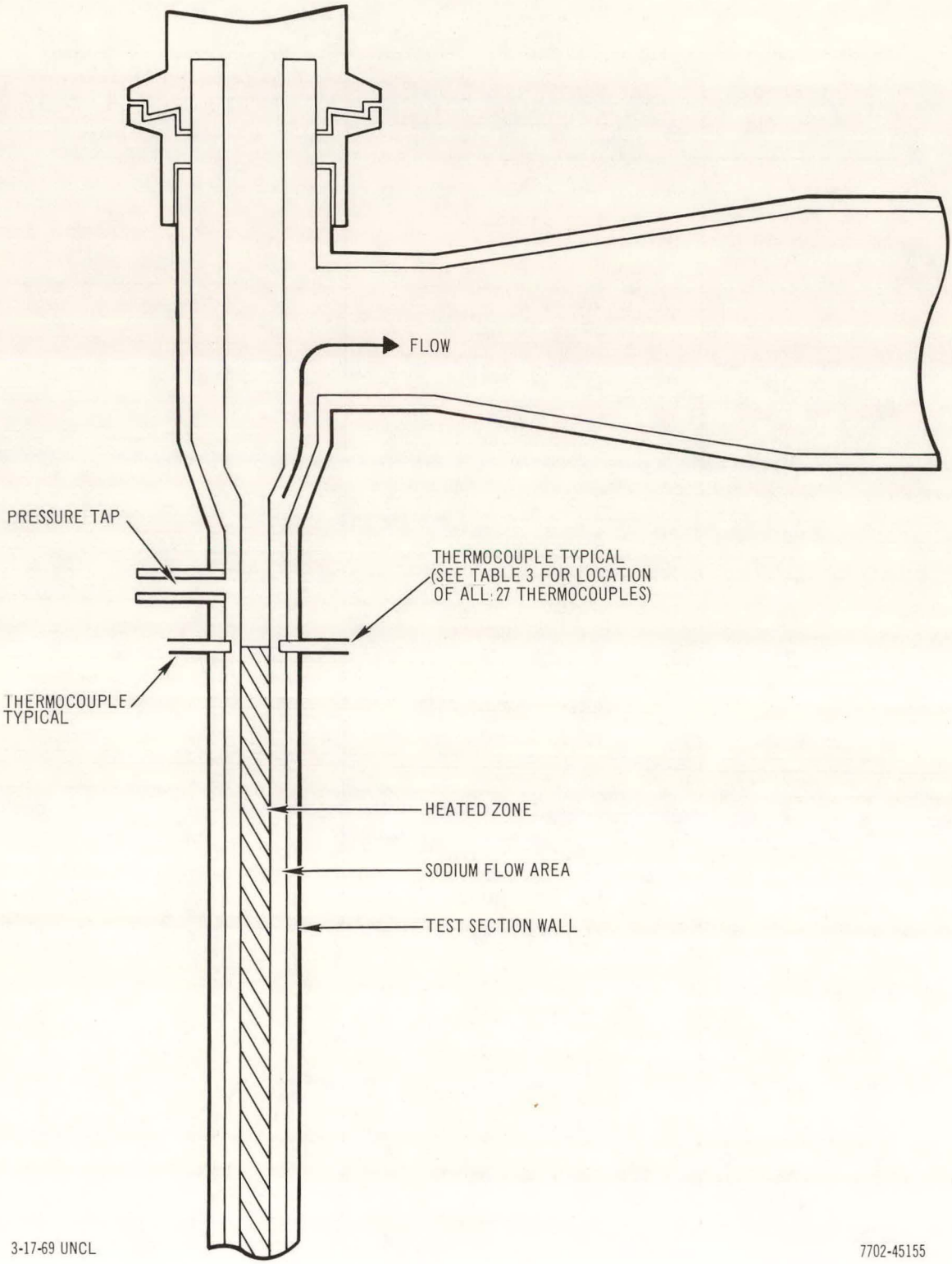

Figure 10. Thermocouple and Pressure Tap Installation

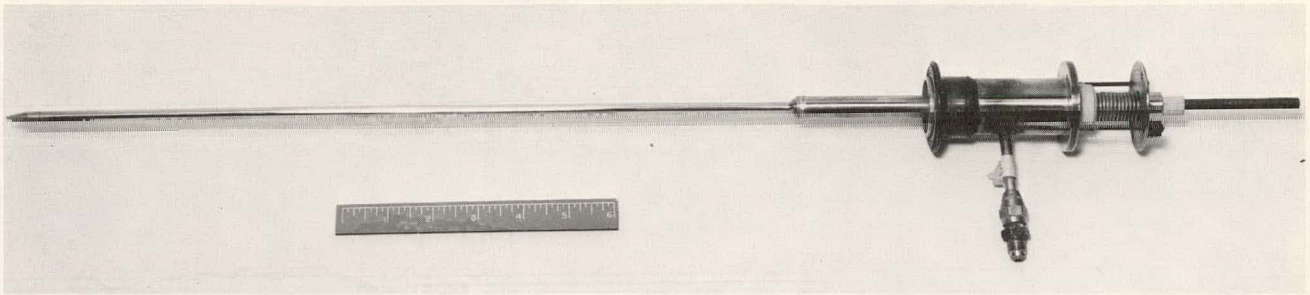

7702-40113

Figure 11. 15 in. Graphite High Flux Heater

Most of the liquid superheating runs used 15 in. long heaters; however, some runs were made with a 30 in. heater.

7. Auxiliary Systems

Auxiliary systems to the loop include an argon-air loop, a water loop, a sodium storage tank, a sodium vapor trap, and a vacuum system. With the exception of the pump, throttle valve, and primary flow meter, the loop is enclosed in an argon-filled, 1/4-in. thick, carbon steel containment box. The argon atmosphere quickly smothers fires from sodium leaks thus minimizing damage. The pump is located in a separate compartment to permit air cooling of the stator coils.

III. EXPERIMENT

A. TEST PROCEDURE

1. Discussion

The sodium liquid superheat needed to initiate boiling in an annular channel was studied over a range of variables by use of the Forced Convection Loop described in Section II. The experimental data (tabulated in Appendix 1) consists of 642 runs divided into 17 groups. Operating conditions covered the following ranges: saturation pressure, 2 to 15.3 psia (1290° to 1626°F); liquid sodium velocity, 2 to 6 ft/sec; heat flux 0.09×10^6 to 0.825×10^6 Btu/hr-ft^2; inlet subcooling, 20° to 300°F; wall superheat 0° to 241°F.

In most experiments the pressure, flow rate, and inlet sodium temperature were maintained constant throughout the run, while the power to the high flux heater was raised until boiling occurred.* For a few experiments (P type data) the flow rate, inlet sodium temperature, and power to the high flux heater were maintained constant throughout the run, while the pressure in the test section was lowered until boiling occurred.

In both procedures, as boiling was approached, the heater power, flow rate, test section pressure, and several temperatures at various locations were recorded. The results do not appear to depend on which of the two procedures was used.

2. Surface Preparation

The surface finish of each heater on which liquid superheating tests were performed was initially one of three types (Table 4). The initial surface was (1) as-received, (2) refinished with 600 grit abrasive, or (3) refinished with

*As measured by signals from one of the boiling detectors. In many cases the onset of boiling was so smooth that sound intensity signals from the accelerometer and wall pressure fluctuation signals from the Barton pressure transducer occurred for several seconds before the integrated signal tripped the comparator and cut off heater power. In these cases the sodium temperature did not climb after boiling started even though heater power continued to increase. When some bulk superheat existed before boiling was initiated, a violent transition from non-boiling to boiling occurred and tripped the EM flowmeter boiling detector.

TABLE 4

INITIAL HEATER SURFACE FINISH

Heater Run Group	rms Reading on Heater Surface μin.	As-Received Sample	Surface Refinished		
			With 320 Grit Abrasive	With 600 Grit Abrasive	With 23μ Abrasive
Ref. 8	15 - 25		X		
A	Not measured	X			
B	~2*	X			
C	25 - 30	X			
CA	2 - 8			X	
J	~2	X			
JA	2 - 8			X	
JB	2 - 8			X	
JC	2 - 8			X	
JD	2 - 8			X	
K	~2	X			
L	8 - 12	X			
KA	~2				X
KB	~2				X
KC	~2				X
KD	~2				X
MA	2 - 8			X	
NA	2 - 8			X	

*This reading is believed to be for Heater "B" as-received tubing; however, the sample marking was smeared and could not be positively identified.

23μ abrasive. However, most of the liquid superheating tests were performed on surfaces that had been mildly corroded by sodium during experimental operation. A stereo photograph pair of a replica* of an "as-received" tubing sample used in the FBR Fuel Cladding and Structural Materials Program is shown

*The replica was prepared by standard electron microscopy replica transfer techniques from a collodion film first shadowed with chromium, then covered with evaporated graphite.

in Figure 12a.[8] Figure 12b is a stereo photograph pair of the same tubing after 589 hours of operation, at a surface heat flux of 10^6 Btu/hr-ft^2, sodium velocity of 20 ft/sec, and sodium temperature of 1210°F. The tubing for the FBR Fuel Cladding and Structural Material Program is prepared by grinding with a 320 grit abrasive and has an rms reading of 15 to 25μ. Thus, Figures 12a and 12b show the range of surface change expected to be experienced by the cladding of a typical LMFBR fuel element. This surface change was used as a reference for the heater surfaces in this program by first preparing the surface of the tubing to a smoother finish than shown in Figure 12a by first grinding with 600 grit or 23μ abrasive and then by running boiling transients with the heater until the surface was corroded more than shown in Figure 12b. This process assured a surface roughness range which spanned that which would occur for typical LMFBR fuel pin cladding. Figure 13 is a stereo photograph pair of a replica of the surface of heat K "as-received" tubing. The grain boundary etching of this surface would indicate that the tubing was pickled during its fabrication process. Figure 14 is a stereo photograph pair of the same heater surface after the K runs, which took 85 minutes heater running time. Figure 15 is a stereo photograph pair of a typical surface after refinishing with 23μ abrasive.

In its latter runs, heater B surface was severely pitted by high temperature sodium. Figure 16 is a stereo photograph pair of the heater B surface after 170 runs. (Corrosion of the heater surface to the extent shown in the figure definitely reduces the superheating capabilities.)

3. Flowmeter Calibration

The flowmeter in the test loop had previously been calibrated by a volumetric method, but another calibration was made as considerable time had elapsed since this procedure. Under all-liquid conditions, the output of the pump flowmeter was compared with the output of another calibrated* flowmeter at the end of the test section. The new calibration based on magnetic field strength, and the original volumetric calibration compared very closely as shown following.

*This flowmeter was calibrated at the Liquid Metal Engineering Center, Santa Susana, California by measuring the strength of the magnetic field and then calculating the flow constant for the flowmeter by means of a computer program. Prior experiments have verified this method.

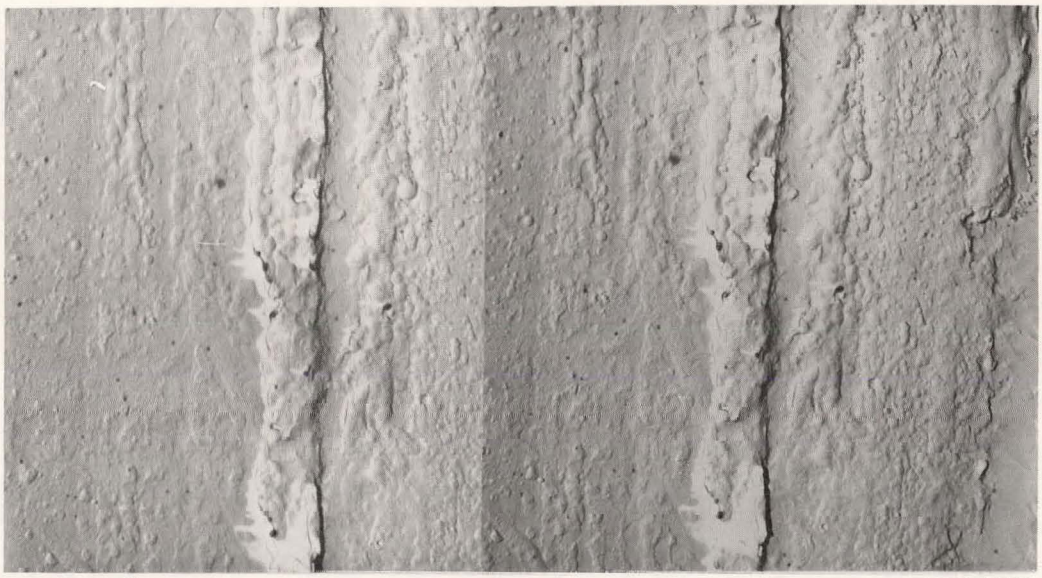

2-24-69 UNCL 7702-45136

A. "AS-RECEIVED" TUBING FOR HEATER NO. 36

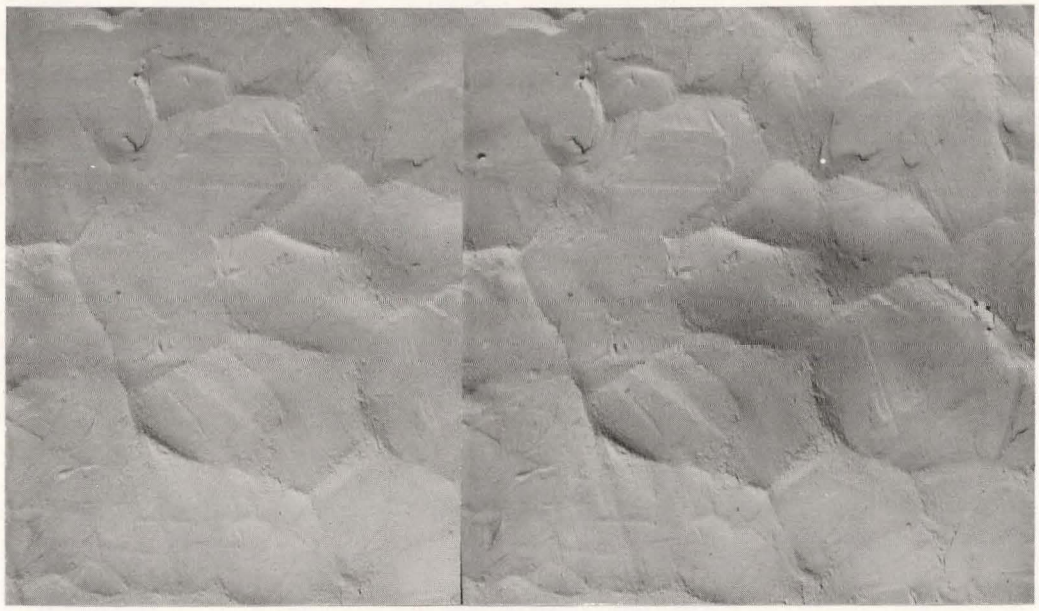

2-24-69 UNCL 7702-45137

B. HEATED ZONE AFTER 589 HOURS OPERATION

Figure 12. Stereo Photograph Pairs of Replicas of FBR Fuel Cladding Surface Used by the FBR Fuel Cladding and Structural Material Programs (2500X)

2-24-69 UNCL 7702-45138

Figure 13. Stereo Photograph Pair of Replica of the Heater K "As-Received" Surface (2500X)

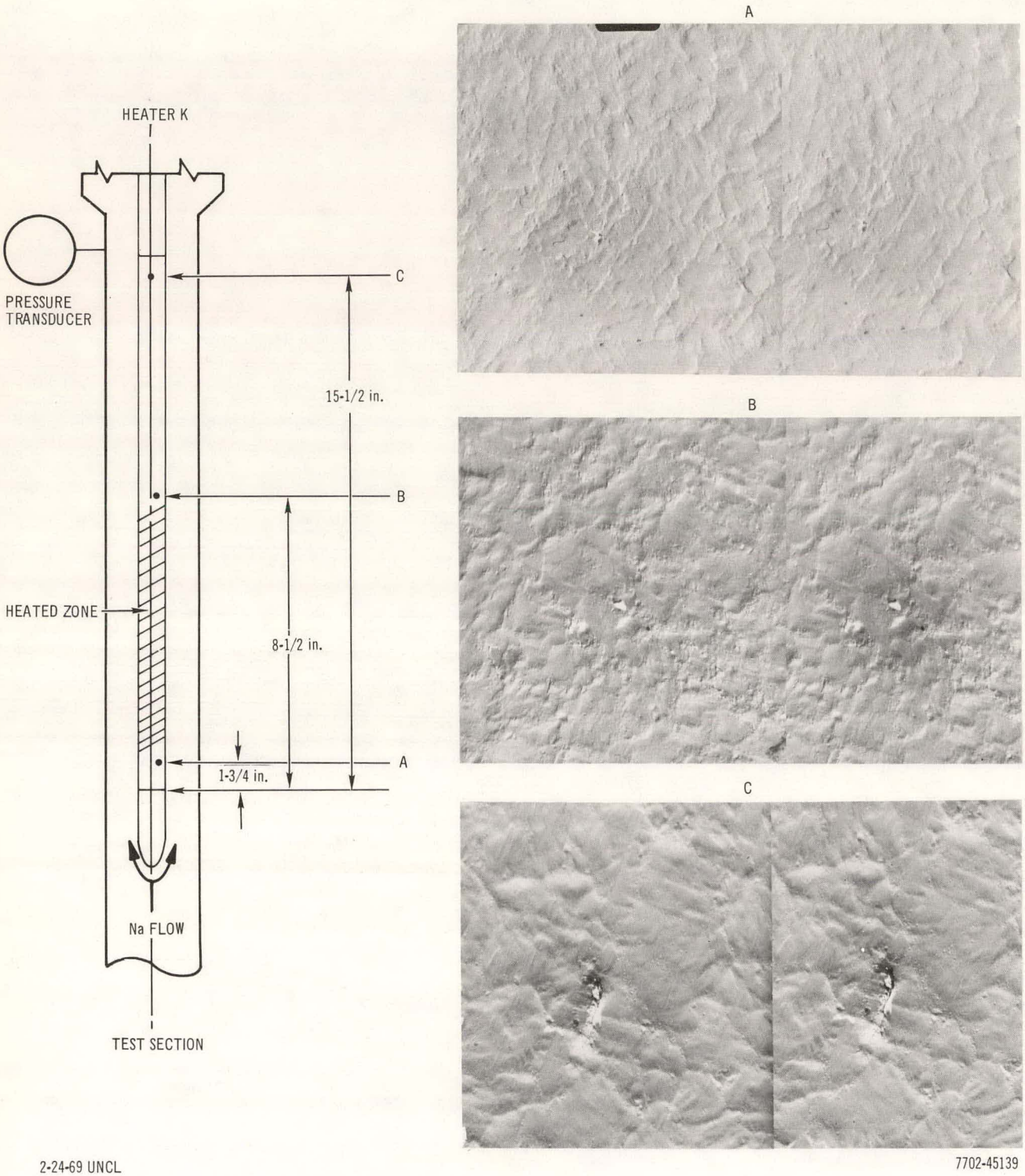

Figure 14. Stereo Photograph Pair of Replica of the Heater K Surface After 85 Minutes Running Time Starting With Figure 13 Surface (2500X)

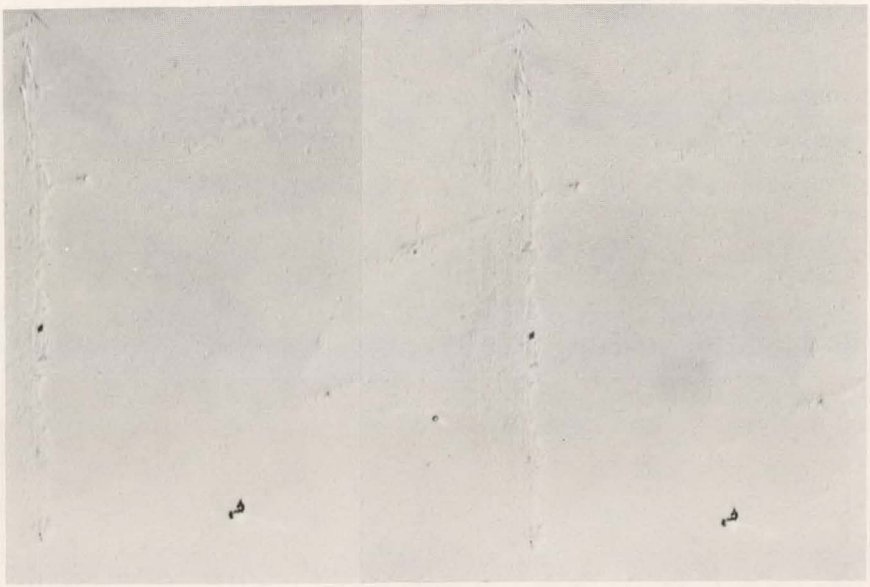

2-24-69 UNCL 7702-45140

Figure 15. Stereo Photograph Pair of Surface Replica of a Heater Surface Refinished With 23 Micron Abrasive (2500X)

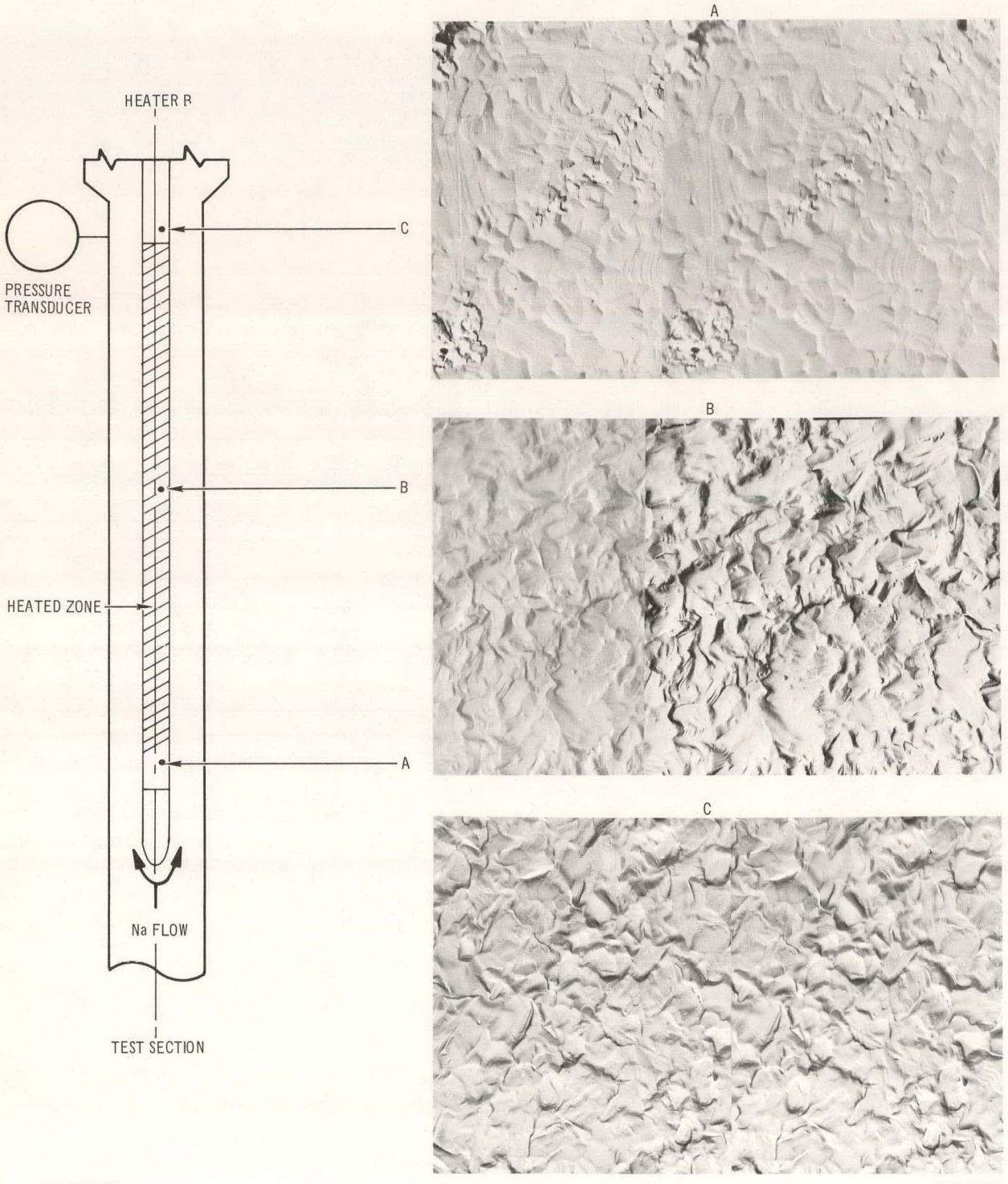

Figure 16. Stereo Photograph Pair of Replica of the Heater B Surface After 170 Liquid Sodium Superheat Tests (2500X)

Original Calibration	0.843	gpm/mv with 600°F sodium
New Calibration		
1st Magnet	0.839	gpm/mv with 600°F sodium
2nd Magnet	0.848	

B. RESULTS OF EXPERIMENT

1. Data Analysis Method

The experimental superheat data were plotted by two methods in order to facilitate comparison with other data and to clarify important trends.

The first method, used for data groups B through L, plots boiling initiation superheat as a function of saturation pressure. This type of plot affords convenient comparison with previous data[1] and, in the case of pool boiling inception at fixed heat flux,[14] adequately depicts the experimental data. However, for forced convection boiling initiation, such a presentation is quite inadequate as it cannot distinguish, even for the case of fixed heat flux, the contributions of inlet subcooling and fluid velocity. As a consequence, graphs of wall superheat vs saturation pressure for forced convection boiling initiation exhibit appreciable vertical distributions, often classified as scatter, which are, in reality, due to deficiencies in the method of data plotting. See Figures 17, 18, and 19.

In the second method, the data are plotted as superheat vs heat flux, for fixed velocity and pressure. In this case, curves of constant inlet subcooling result with a minimum of data scatter. See Figures 20 and 21. Since this method more clearly reveals the important trends, it has been used for plotting the most recent data.

For all liquid conditions* the following relations apply at boiling initiation:

$$(T_w - T_i) = (T_w - T_b) + (T_b - T_i) = (T_w - T_s) + (T_s - T_i) \qquad \ldots(1)$$

$$(T_w - T_s) = (T_w - T_b) + (T_b - T_s) \qquad \ldots(2)$$

*The all-liquid heat transfer approach to boiling inception in liquid metals was suggested by J. G. Collier in a private communication reported by Kosky.[15]

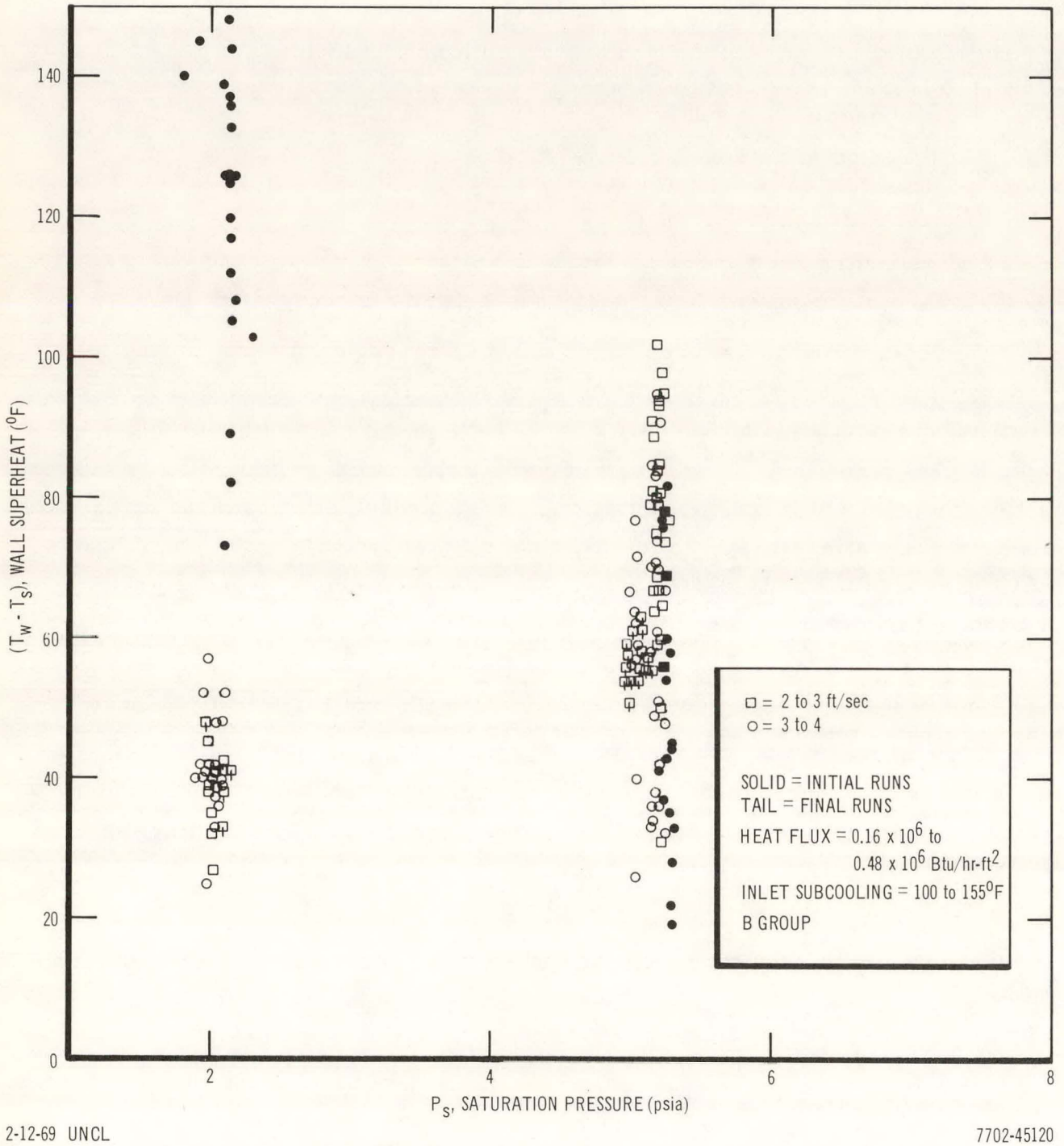

Figure 17. Wall Superheat vs Saturation Pressure (B Group)

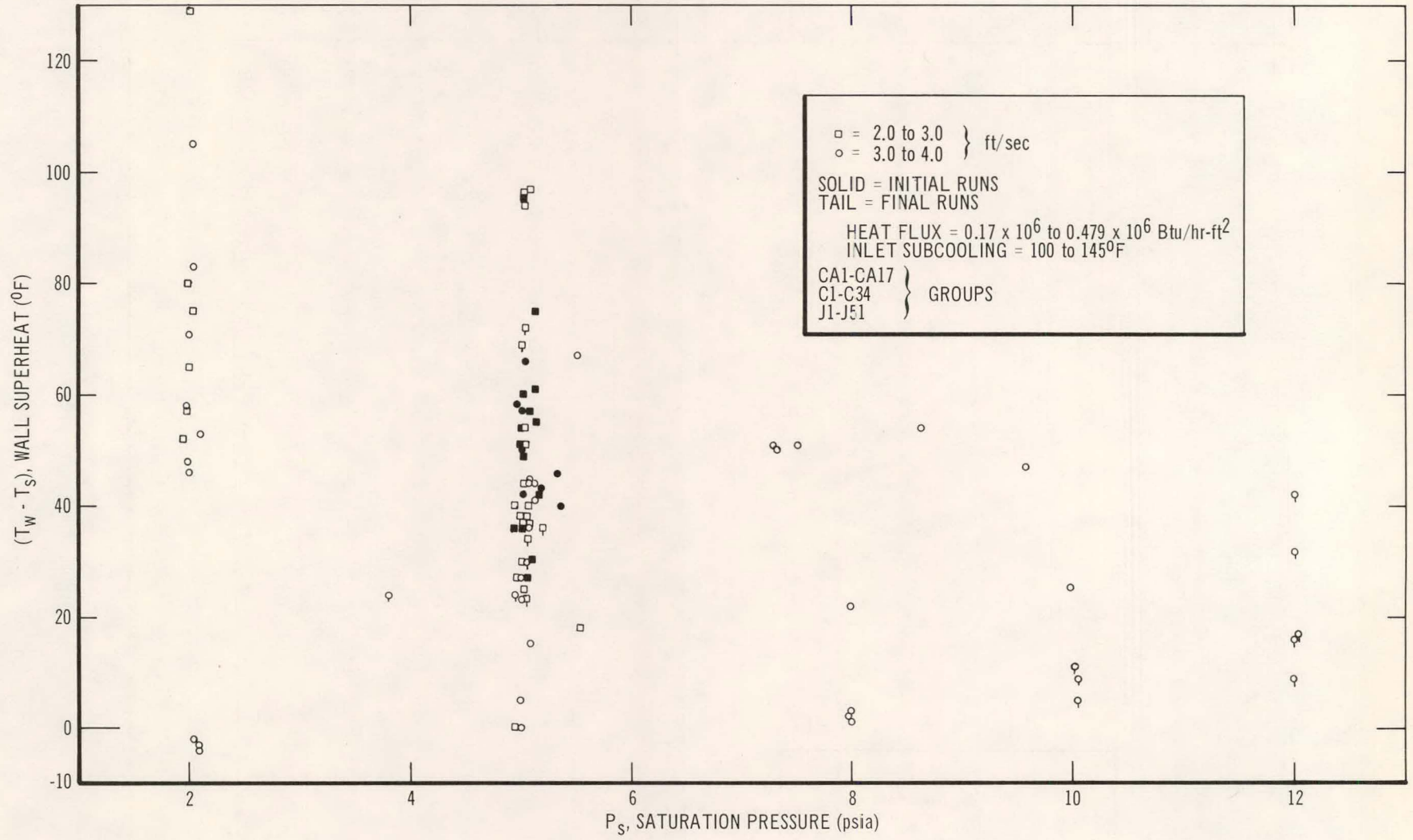

2-12-69 UNCL

7702-45121

Figure 18. Wall Superheat vs Saturation Pressure (C, J Groups)

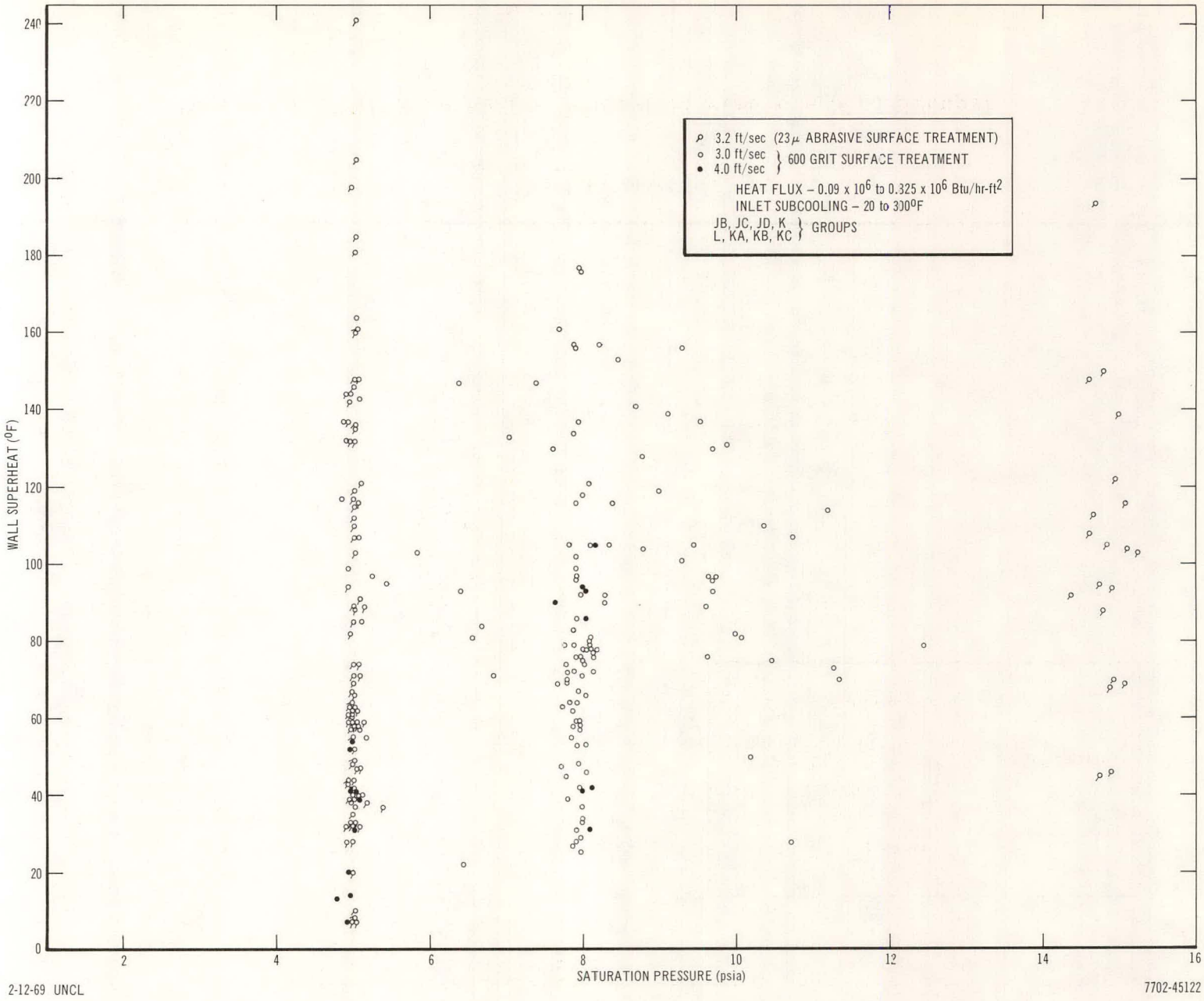

Figure 19. Wall Superheat vs Saturation Pressure (JB, JC, JD, K, L, KA, KB, KC Groups)

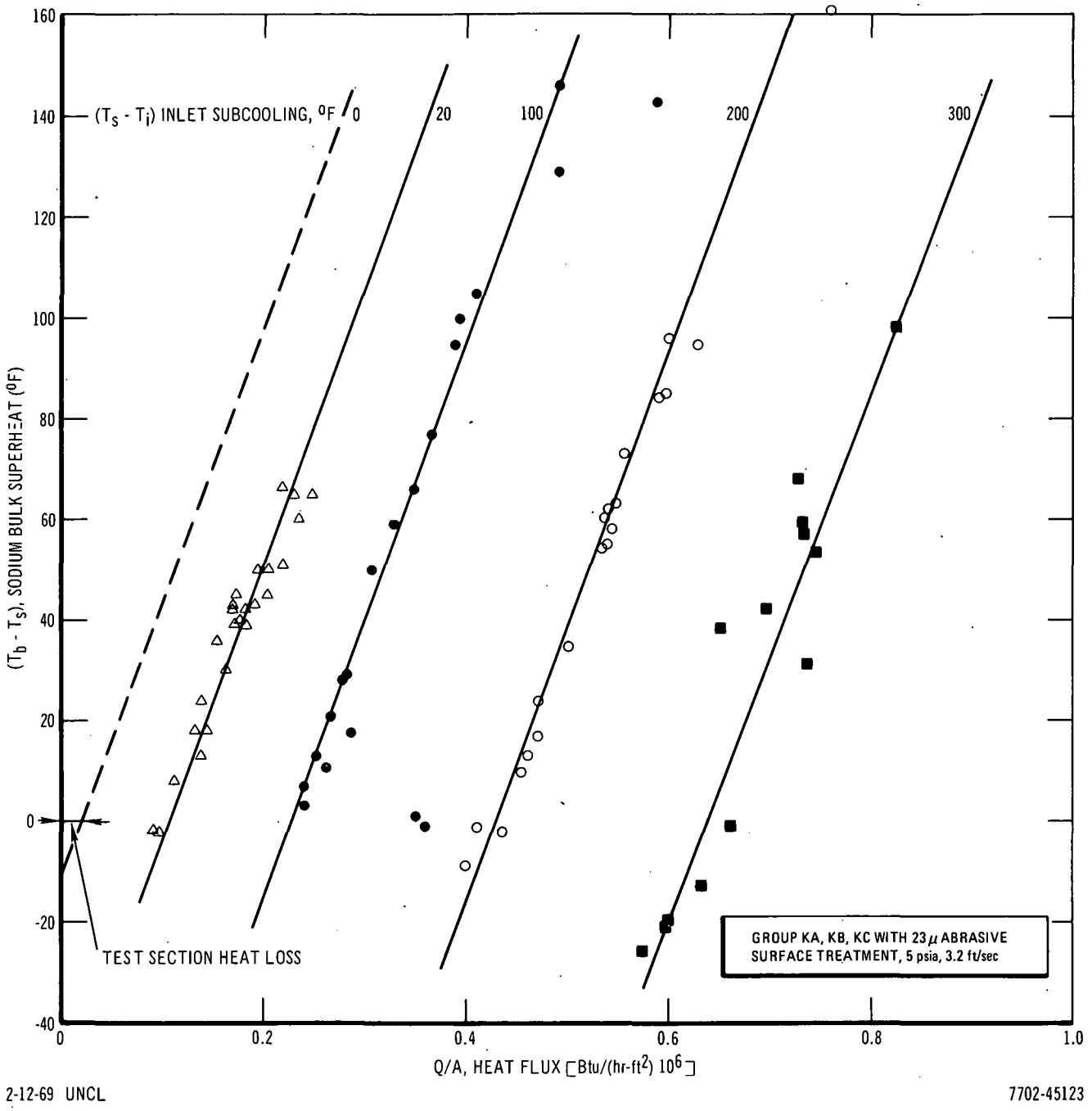

Figure 20. Bulk Superheat vs Heat Flux (KA, KB, KC Groups)

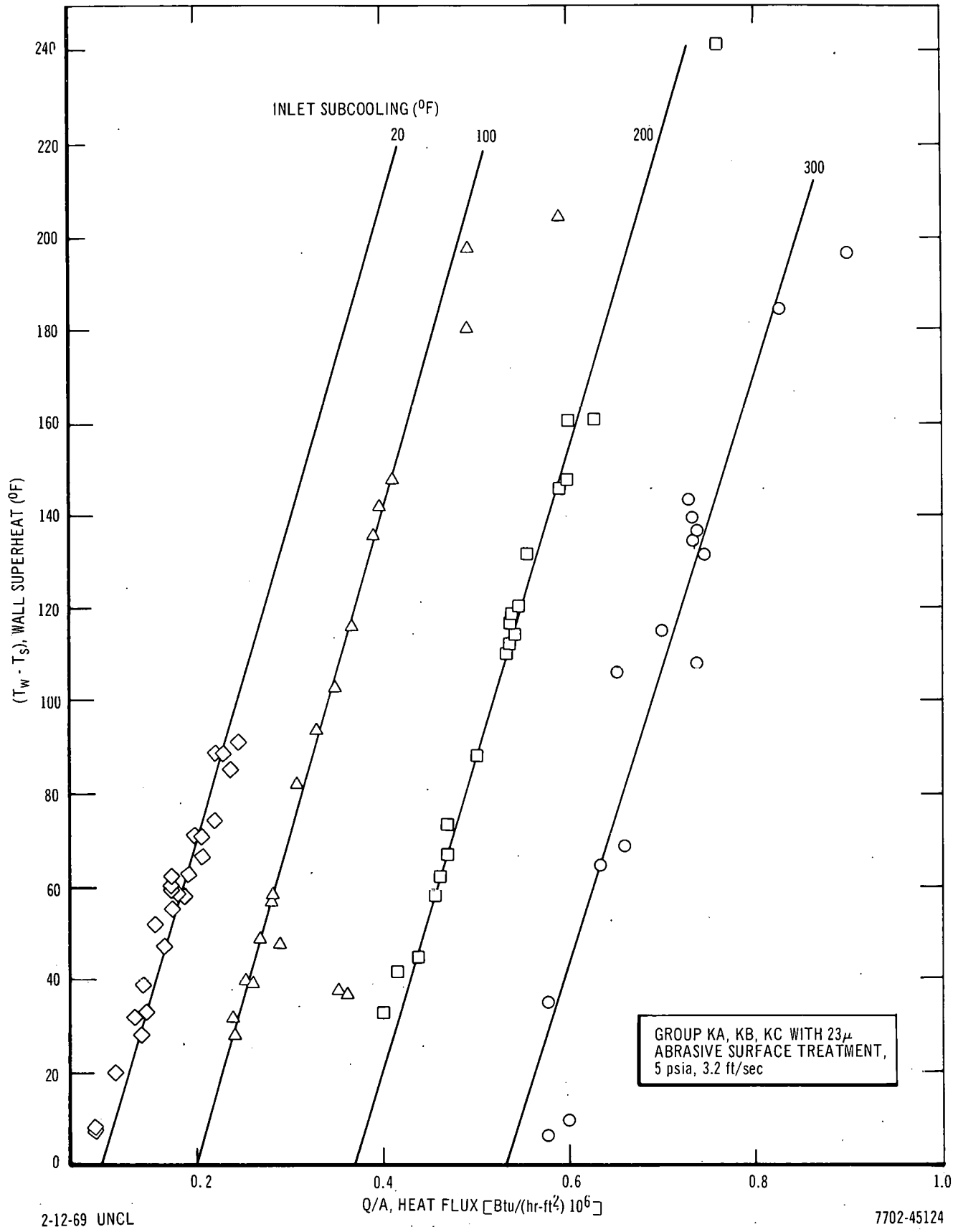

Figure 21. Wall Superheat vs Heat Flux (KA, KB, KC Groups)

where

T_b = liquid bulk temperature (measured* directly)

T_w = wall temperature at the end of the heated section (calculated† from T_b via Equation 3)

T_s = saturation temperature (measured as pressure and calculated from sodium saturation properties[16])

T_i = inlet liquid temperature (measured directly)

$(T_w - T_s)$ = wall superheat

$(T_b - T_s)$ = bulk superheat

$(T_s - T_i)$ = inlet subcooling

$(T_b - T_i)$ = temperature rise of the flowing sodium in the test section.

The wall to bulk temperature difference is:

$$(T_w - T_b) = \frac{(Q/A)}{h} \qquad \ldots (3)$$

where (Q/A) is the heat flux at the heating surface and h is the all-liquid heat transfer coefficient.§

The temperature rise of the flowing sodium is,

$$(T_b - T_i) = A\left[\frac{(Q/A) - (Q/A)_L}{Wc}\right] = (T_b - T_s) + (T_s - T_i) \qquad \ldots (4)$$

*During experimental runs, the heater was usually slightly off center and, as a result, the thermocouples in the four quadrants of the liquid annulus generally had different readings. The maximum liquid bulk temperature reading was used each time to compute the bulk temperature.

†To avoid mechanically perturbing the heater surface T_w was not measured directly.

§No detectable difference in film temperature drop would result from the use of either the Dwyer[17,18] or Kays and Leung[19] method of determining the sodium heat transfer coefficient. (See Appendix 2.)

where $(Q/A)_L$ is the heat flux, based on the heated surface area, corresponding to the test section heat loss, W is the liquid sodium flow rate, A is the heated surface area, and c is the liquid specific heat.

Combining Equations 1, 2, and 3 gives:

$$(T_w - T_b) + (T_b - T_i) = \frac{Q}{A}\left\{\frac{1}{h} + \frac{A}{Wc}\left[1 - \frac{(Q/A)_L}{(Q/A)}\right]\right\} = T_w - T_i$$

$$= (T_w - T_s) + (T_s - T_i) \quad . \qquad \ldots(5)$$

Except for the inclusion of the effect of test section heat loss, which is present in any real system, the above expression is identical to that used by Kosky.[15]

2. A Condenser*

a. B Group

Figure 17 shows wall superheat vs saturation pressure for the B group of runs. The wall superheat ranges from 13° to 148°F. For improved interpretation, the symbols identify velocity and relative operational time on the heater (solid points, initial runs; points with a tail, final runs). At 2 psia, the initial tests produced the highest superheats, while the final tests generally produced the lowest superheats. The lowest superheats are generally obtained at the highest velocity. The 5-psia data shown in Figure 17 show that the initial B Group runs, which were taken after the similarly identified runs at 2 psia, span almost the entire range of superheat. The final runs, however, group in superheat range which is very narrow and of intermediate magnitude.† The maximum superheat decreases with increasing pressure whereas the minimum superheat

*Because of strong indications of gas entrainment, the data for velocities greater than 4 ft/sec are excluded from the B through L runs. In addition, the initial shakedown runs (A Group) are not included.

†Corroboration of this observation has been presented by Heineman[20] and Pinchera, et al.,[21] who showed that both the magnitude and scatter, for sodium superheat data, decreased with increased heater operational time. Pinchera, et al.[21] have related this aging effect to surface changes due to corrosion in flowing high temperature sodium.[8]

remains essentially constant. It is emphasized that, for the B Group shown in Figure 17, a total of 170 sequential runs were made on the heater and resulted in extensive pitting of the surface.*

b. C Through L Groups

Verification of the constancy of surface condition is shown in Figure 18 (C and J Groups) where, at 5 psia, superheats obtained in the early, intermediate, and latter part of the heater operational time exhibit no apparent difference. Paralleling the trend observed in Figure 17, superheat decreases with increasing pressure, within the limitations posed by the small amount of data available for pressures other than 5 psia.

Figure 19 shows wall superheat as a function of saturation pressure for the K,† KA, KB, KC, JB, JC, JD, and L Groups. The very smooth heated surfaces (23μ grit surface treatment) constitute all of the runs made at 15 psia and virtually all of the runs taken at 5 psia; surfaces treated with 600 grit abrasive constitute the remaining runs. Wall superheats range from 7 to 241°F at 5 psia, 25 to 177°F at 8 psia, and 45 to 194°F at 15 psia. If similar surface finishes are compared, i.e., 5 and 15 psia, wall superheat decreases as saturation pressure increases.§

It is of interest to note that the superheat data presented in Figures 17 through 19 show an appreciable distribution. Such distributions have previously been obtained by Holtz and Singer[14] for stagnant sodium and by Grass, et al.,[22] for both sodium and potassium. In contrast, the forced convection, incipient boiling superheat data of Chen,[6] for potassium, show very little scatter and are well represented by a single curve. The apparent absence of scatter in this

*The extensive heater surface corrosion that occurred with the B heater, resulting in many discrete pits, undoubtedly produced the narrow range of superheat. (See Figure 16 for surface condition.) For all succeeding groups, the maximum number of runs, before surface refinishing, was limited to 38 for the C Group and 51 for the J Group, and to about 35 for all other groups. By following the procedure of periodic resurfacing of the heater, the number of boiling sites on the surface of the heater was maintained in a narrow range; this effectively reduced surface condition as a variable in the superheat data so obtained.

†See Appendix 3 for the description of an unusual superheat pattern which occurred during K runs.

§This observation coincides with that of Holtz and Singer[14] and Pinchera, et al.,[21] for stagnant sodium and with that of Heineman[20] for flowing sodium.

latter case[6] may be due to the limited range of test conditions (heat flux, velocity, inlet subcooling) covered at a given saturation pressure.

To clarify the conditions contributing to the observed superheat distribution, bulk sodium superheat vs heat flux was graphed at various inlet subcoolings, as shown in Figure 20.* The runs shown are from Groups KA, KB, and KC, in which a periodic surface retreatment with 23μ abrasive was performed. Furthermore, the runs are for a fixed pressure of 5 psia and a test section liquid velocity of 3.2 ft/sec. Thus, the principal variables are bulk superheat and heat flux at the inception of boiling. The relationship between these two quantities is discussed below.

Figure 20 shows that for a given bulk superheat heat flux increases with increasing inlet subcooling; for a given inlet subcooling, the bulk superheat increases as the heat flux increases. This pattern is to be expected from Equation 4, the all-liquid heat balance, which shows that at constant flow rate the sum of the inlet subcooling and bulk superheat will be directly proportional to the net heat input to the test section. As verification, note that at a given gross heat flux,† e.g., 0.50×10^6 Btu/hr-ft^2, the sum of inlet subcooling and bulk superheating is 239°F for 200°F subcooling, and 250°F for 100°F subcooling. This may be considered a typical case as a similar condition exists for the other curves of constant inlet subcooling. Also, extrapolation of the curves of constant inlet subcooling to zero (see Figure 20) results in the dashed line at the left of the figure. The heat flux indicated by the dashed line at zero bulk superheating (0.02×10^6 Btu/hr-ft^2) represents the test section heat loss.§ If, for zero bulk superheat, the test section heat loss $(Q/A)_L$, is subtracted (See Appendix 4) from the heat flux indicated for each value of inlet subcooling, then inlet subcooling is seen to vary approximately directly with net heat flux. Figure 20 demonstrates the consistency of the heat input and temperature measurements and shows that all-liquid conditions (i.e., single phase thermal balance as given by Equation 4) prevail for these data.

---

*The figure is valid only for a given heater length, in this case, 15 in.
†Actually the same net heat flux is being compared if the heat loss-heat flux is subtracted from the gross heat flux.
§The test section heat loss has not been subtracted from any of the heat flux values shown in this report.

From the above discussion, it is seen that, for incipient boiling, sodium bulk superheat increases in direct proportion to net heat flux for otherwise fixed conditions. If the all-liquid film coefficient (Figure 22) temperature drop is used to calculate wall temperature, a similar relationship, Equation 5, will hold for wall superheat vs heat flux, as depicted in Figure 21. In this case, the slope of the lines is somewhat greater than that appearing in Figure 20, but the trends are identical.*

Examination of the trends indicated by the data of Figure 20 may give the impression that the data distribution is entirely due to preselection of the experimental conditions and that a true statistical data distribution does not therefore prevail. However, this assumption is not correct since, it is recalled, the flow rate, pressure, and inlet subcooling are set for a given run and the bulk superheat and heat flux, at boiling inception, are those which concur with either the acoustic, or flow rate, boiling detector signal. Therefore, while bulk superheat consistently increases with increasing heat flux, thus showing heat flux to be a major contributor to the observed data distribution, the conditions existing at boiling inception, as signalled by the boiling detector, are solely determined by the inception phenomenon.

In the present experiment, the rate of power increase to the sodium is maintained essentially constant for a given group of runs, and it typically results in a boiling signal about 40 sec after power application. The possible effect on the incipient boiling data of a power increase rate other than the one used is not known but may bear investigation in future tests.

3. B Condenser

a. KD Through NA Group

With the B condenser design, in which the two-phase mixture, or hot liquid, did not come into contact with the argon cover gas prior to mixing with the subcooled liquid sodium, no acoustic noise was detected, without boiling,

*This pattern is confirmed by the data for stagnant sodium of Pinchera, et al.,[21] Holtz and Singer,[14] and Marto and Rohsenow;[23] all of these data show wall superheat to increase in approximately direct proportion to the heat flux. Thus, the trend of wall superheat vs heat flux, at boiling initiation, is identical both for stagnant sodium and for forced flow sodium.

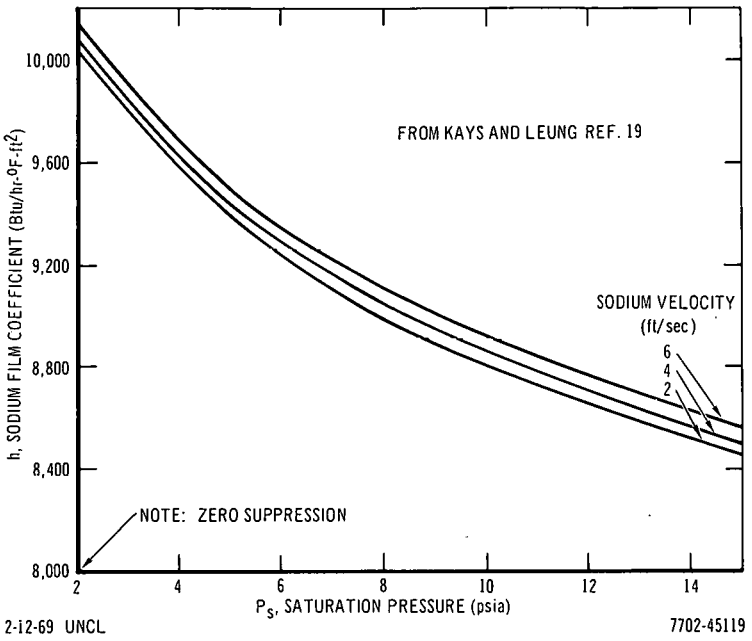

Figure 22. Sodium Film Coefficient vs Saturation Pressure

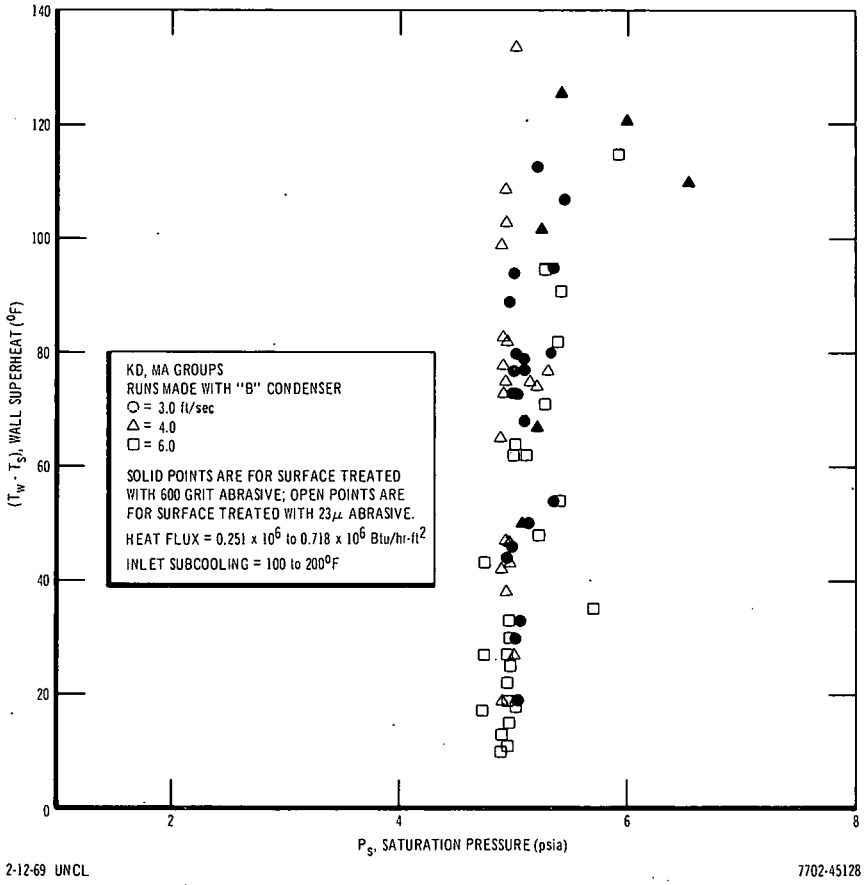

Figure 23. Wall Superheat vs Saturation Pressure (KD, MA Groups)

at velocities up to 9 ft/sec. As a consequence, runs KD, MA, and NA are believed to be almost free of the influence of gas entrainment; however, the amount of gas in the circulating sodium has not been measured directly. Figure 23 shows wall superheat as a function of pressure level for the KD and MA groups of data. The former group is for 23μ abrasive surface treatment. The heat flux varied from 0.25×10^6 to 0.72×10^6 Btu/hr-ft^2 and the inlet subcooling from 100 to 205°F. There is a trend for superheat to decrease with increasing velocity, as shown by the fact that the 6 ft/sec runs were usually the lowest and the 3 to 4 ft/sec runs usually the highest.

4. Discussion of Experimental Results

a. Comparison with All-Liquid Heat Balance

(1) Velocity and Heat Flux Effects

The present data, and those of Pinchera, et al.,[24]* show boiling initiation superheat (bulk or wall) to decrease rapidly with increasing fluid velocity. The main features of this superheat velocity behavior are consistent with all-liquid heat transfer relationships, Equations 1 through 5; more subtle secondary effects on boiling inception, such as velocity induced eddies and turbulence at cavity sites, are not accounted for by all-liquid heat transfer considerations alone.

Figure 24 shows sodium bulk superheat as a function of heat flux for surfaces treated by 23μ abrasive, at 5 psia and 100°F inlet subcooling, and velocities of 3.2 and 6 ft/sec. The lower velocity data are taken from Figure 20, while the higher velocity points constitute the most recent data (Group KD). It is believed that the "A" condenser design did not affect the low velocity results of Figure 24. Otherwise the comparison in Figure 24 is for identical conditions. For the same heat flux, bulk superheat is considerably less at 6 ft/sec than at 3.2 ft/sec. For both velocities, substitution of the appropriate values into Equation 4 will produce two lines which closely correspond to the data points.

*Comparison of the data of Pinchera[24] by the present method of predicting boiling initiation trends was not possible because his experimental conditions were not sufficiently described.

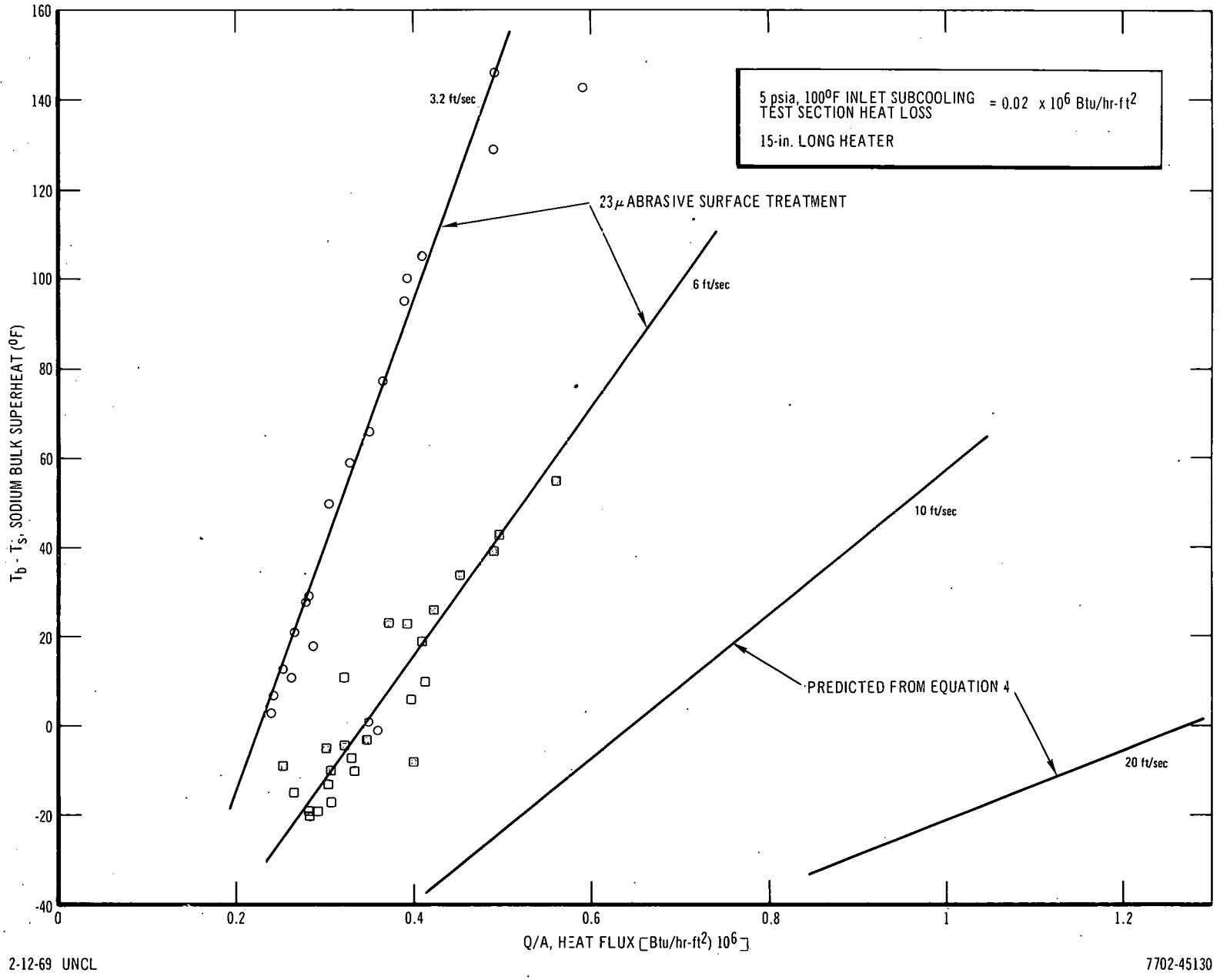

Figure 24. Bulk Superheat vs Heat Flux at Various Sodium Velocities

The all-liquid heat balance equation, Equation 4 therefore, not only correctly accounts for the trends shown by the KD, MA, and NA data but also produces favorable comparison with virtually all of the data previously obtained. The predicted lines for 10 and 20 ft/sec are also shown in Figure 24 and indicate progressively lower superheat with increasing velocity. (Verification of these latter predictions will require additional data.)

In summary, Equation 4 shows that bulk superheat increases with net heat flux and, for a given net heat flux, that it decreases with increased velocity and with increased inlet subcooling.*

(2) Surface Finish Effects

An attempt to ascertain the effect of initial surface finish on bulk superheat is shown by Figure 25. Except for initial surface finish, all conditions, flow rate, inlet subcooling, and pressure were identical for these tests. The figure illustrates that the surface treated with 23μ abrasive consistently produces somewhat greater sodium bulk superheat† (about 35°F) than the surface treated with 600 grit abrasive. Although this trend generally coincides with the observations of Marto and Rohsenow,[23] for boiling initiation in stagnant sodium, the role played by surface condition is not entirely clear. For given conditions, the all-liquid film temperature drop for a smooth surface would be expected to be larger than that for a rough surface. When coupled with the observed greater bulk superheat, the wall superheat for a smooth surface would be expected to be considerably greater than that for a rough surface. The all-liquid prediction (Equation 4) does not account for these effects, yet produces reasonably good correspondence with both sets of data, with the comparison being better for the rougher surface. The bulk superheat vs heat flux data for both surfaces essentially group in a single band and no appreciable distribution difference appears to exist.§

*Completely analogous behavior has been observed[25] for low pressure, forced convection local boiling of water.

†A similar relationship would prevail if the bulk superheat data were converted to wall superheat.

§This result differs from the Marto and Rohsenow[23] findings for a mirror finish and etched surface.

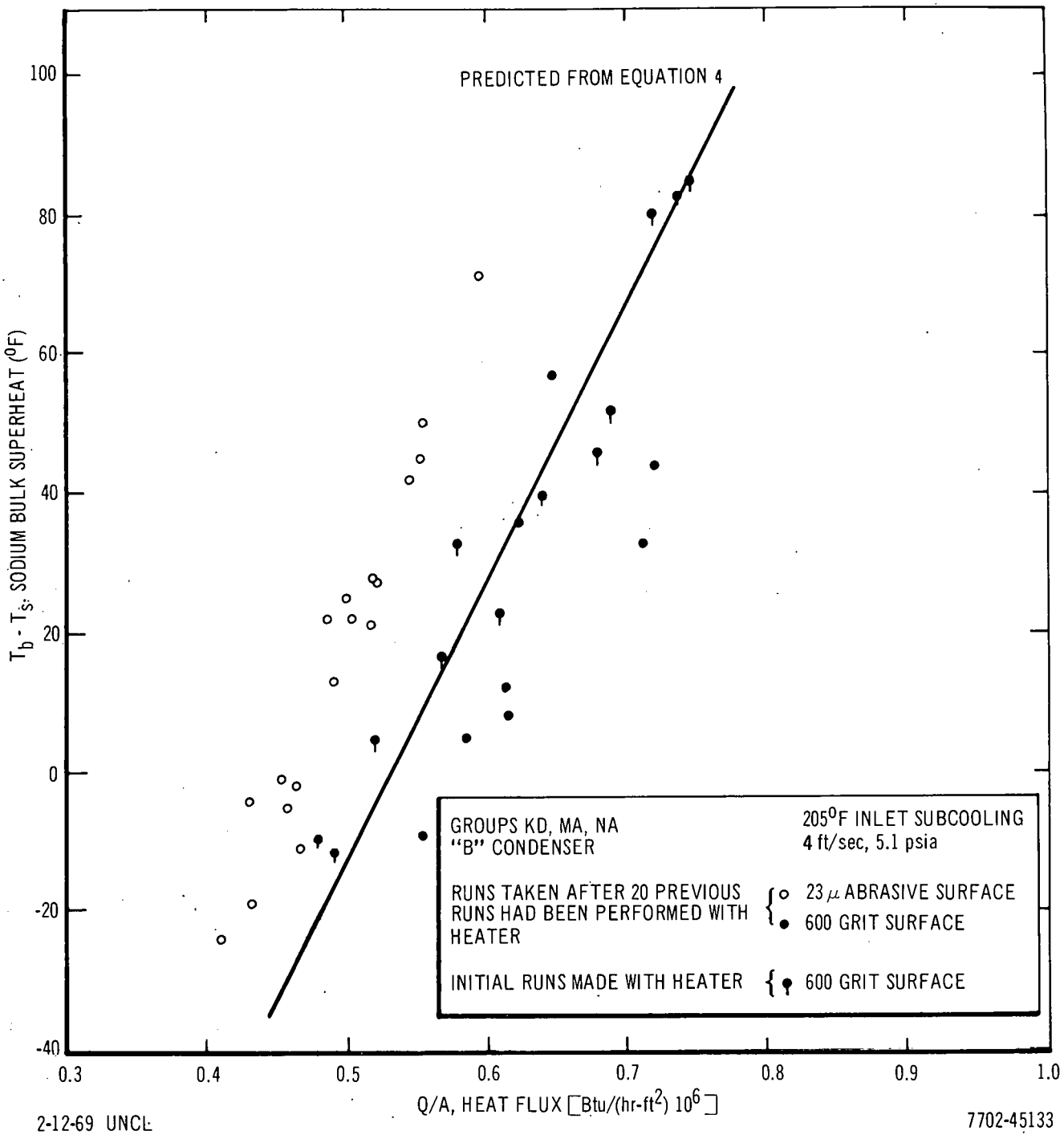

Figure 25. Bulk Superheat vs Heat Flux for Various Heater Surface Finishes

The influence of surface effects on superheat was minimized by use of a periodic surface refinishing treatment after each group of approximately 40 tests. Figure 25 shows that, under these conditions superheat is not affected by operational time on the heater. Comparison of the solid points (runs taken after 20 previous tests) with the solid points with a tail (initial runs made with a new heater), shows that no substantial difference exists between the two sets of data. As evidenced by the B Group runs, more than 100 runs are required before a noticeable change in surface condition and in superheat can be detected. (See Figure 17.)

(3) Pressure Effects

The all-liquid heat balance equation implies that pressure level will not be a significant influence, except on test section heat loss, $(Q/A)_L$. Figure 26 shows two sets of bulk superheat vs heat flux data, each set taken under identical conditions except for pressure. The data points represented by squares (open points are for 5 psia, solid points are for 2 psia) are for 3 ft/sec and 145 to 150°F inlet subcooling, for an as-received surface. The points represented by circles (open points are for 15 psia, solid points are for 5 psia) are for 3.2 ft/sec and 200°F inlet subcooling for surfaces with a 23μ abrasive surface treatment. For each set of data, the points group in a single line and are well represented by the all-liquid prediction method (Equation 4). For each set of data, however, the lower pressure level points are not only slightly displaced to the right, but the maximum superheats and the heat flux are greater for the lower pressures. Also, as discussed in more detail in the following subsection, the superheat distribution is such that a greater proportion of the total runs falls into a higher superheat region as pressure decreases, other conditions being identical.

The pressure effect on bulk superheat illustrates an important limitation on using the all-liquid heat balance equation. While Equation 4 can be expected to show the major trends existing for incipient boiling superheat and can predict the curve along which superheat data fall (for given conditions), it cannot predict boiling inception, the limits of superheat, or the data distribution. Presently, only experimental data can provide the latter information.

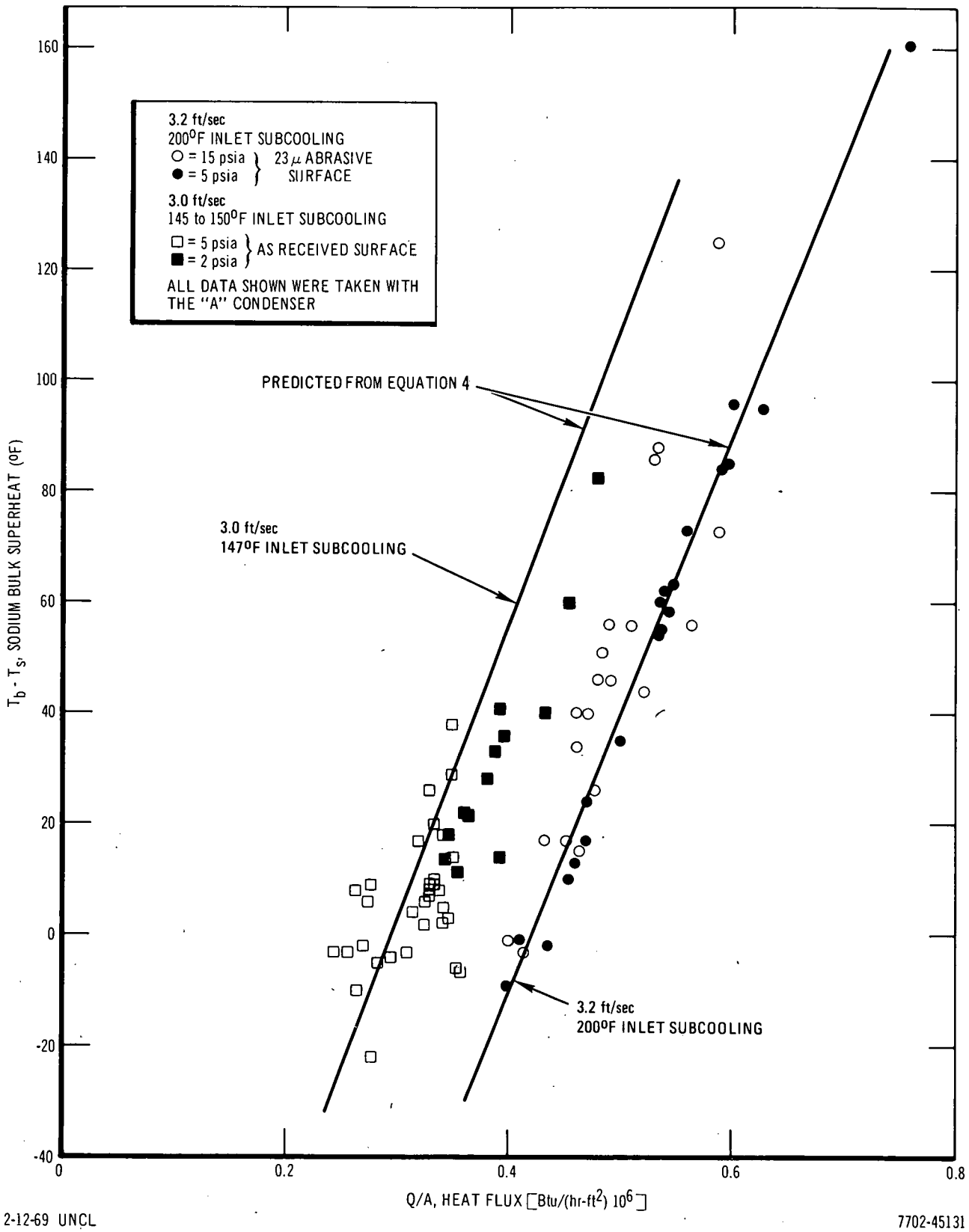

Figure 26. Bulk Superheat vs Heat Flux at Various Saturation Pressures

b. Superheat Data Histograms

Figure 27 displays the number of runs vs wall superheat for the 5-psia, 3 ft/sec tests (Figure 19) in which heat flux varied from 0.09×10^6 to 0.825×10^6 Btu/hr-ft^2 and inlet subcooling varied from 20 to 300°F.

Two histograms are shown, one for the surface treated with 600 grit abrasive and the other for the surfaces treated with 23μ abrasive. For both surfaces, the bulk of the data fall into the 20 to 80°F range, and the distributions appear to be similar within this range. However, the smoother surface contains a much larger portion of the 100 to 180°F range and contains all of the data for superheats greater than 180°F. As previously discussed, it is emphasized that the wall superheat, which is the sum of the film temperature drop and the bulk superheat, increases approximately directly with heat flux. That is, the film temperature drop increases directly with heat flux whereas the sodium bulk superheat increases directly as net heat flux (with test section heat loss accounted for). Thus, the wall superheat distributions shown in Figure 27 are due primarily to heat flux variations and secondly to different inlet subcoolings where superheat increases with increasing heat flux and decreases with increasing subcooling.

Only in the case of a small number of runs (see Figure 20 for inlet subcoolings of 20 and 300°F) for which all conditions, including heat flux, are identical is a real statistical distribution in evidence.

Figure 28 is a histogram of the 8-psia, 3.2 ft/sec runs in which heat flux ranged from 0.235×10^6 to 0.790×10^6 Btu/hr-ft^2 and inlet subcooling from 105 to 290°F. The general shape of the wall superheat distribution is similar to that of the 5-psia data with the bulk of the superheats occurring between 30 and 110°F.

A histogram of the data of Figure 23 is shown in Figure 29 and, as expected from the previously observed trend, wall superheat decreases with increasing velocity. The data representations shown in Figures 28 and 29 are the combined result of three strong influences: heat flux, inlet subcooling, and velocity.

Histograms of the data of Figure 26 are shown in Figure 30. For each set of data (2 and 5 psia; 5 and 15 psia), superheat is greater, and the proportion of higher superheat is larger, at the lower pressure. The trend of higher

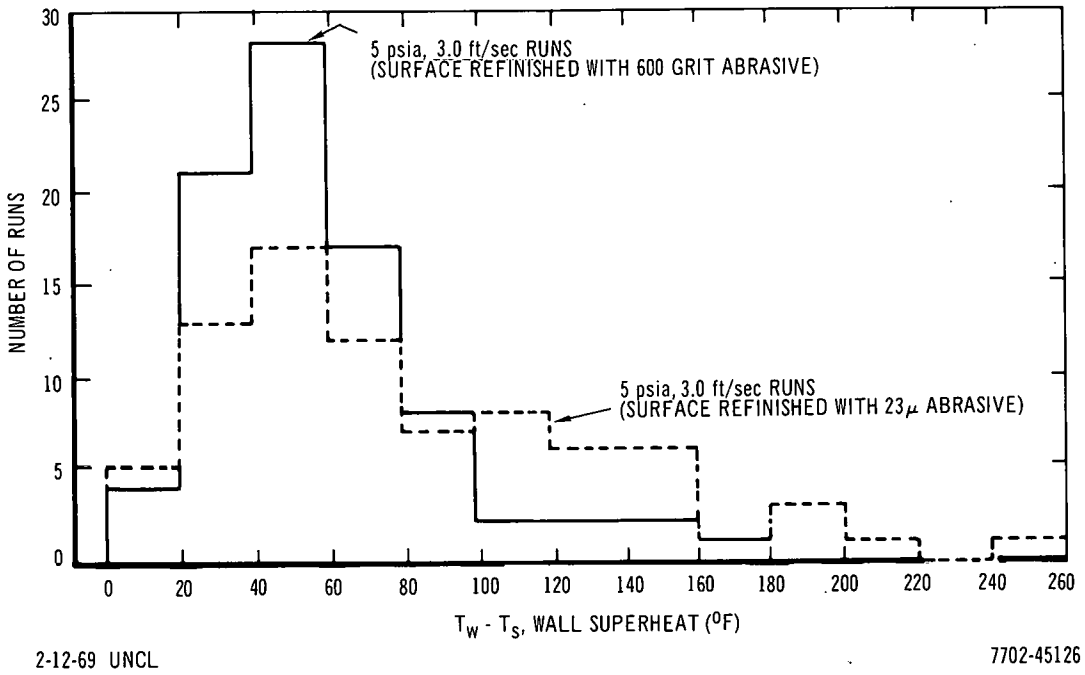

Figure 27. Histogram for 5 psia, 3.0 ft/sec Runs

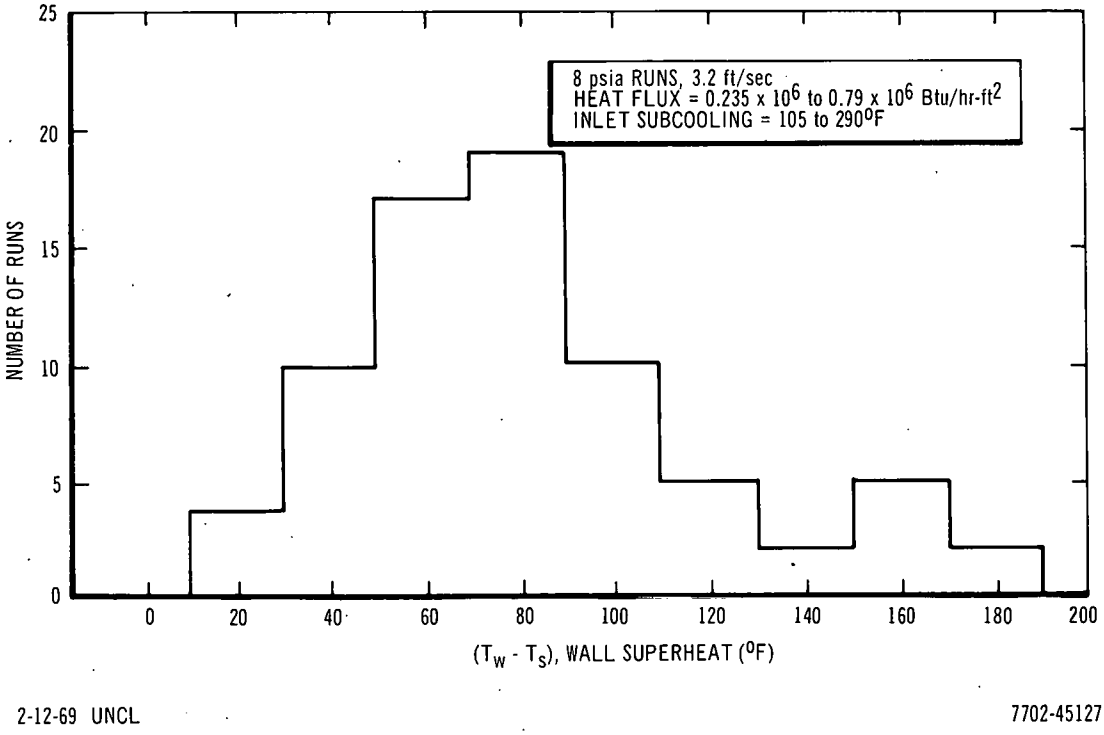

Figure 28. Histogram for 8 psia, 3.2 ft/sec Runs

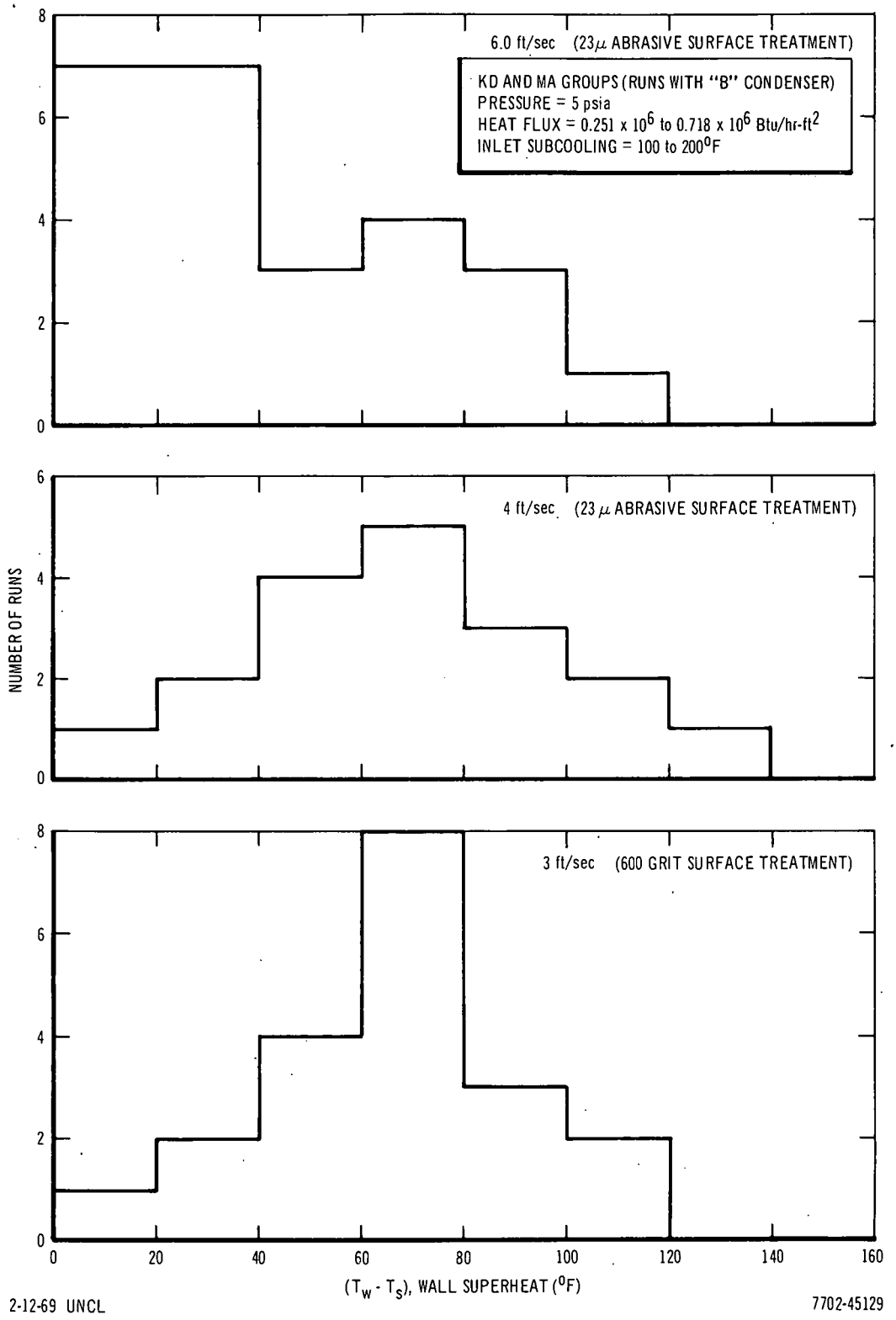

Figure 29. Histograms for Various Liquid Velocities (KD, MA Groups)

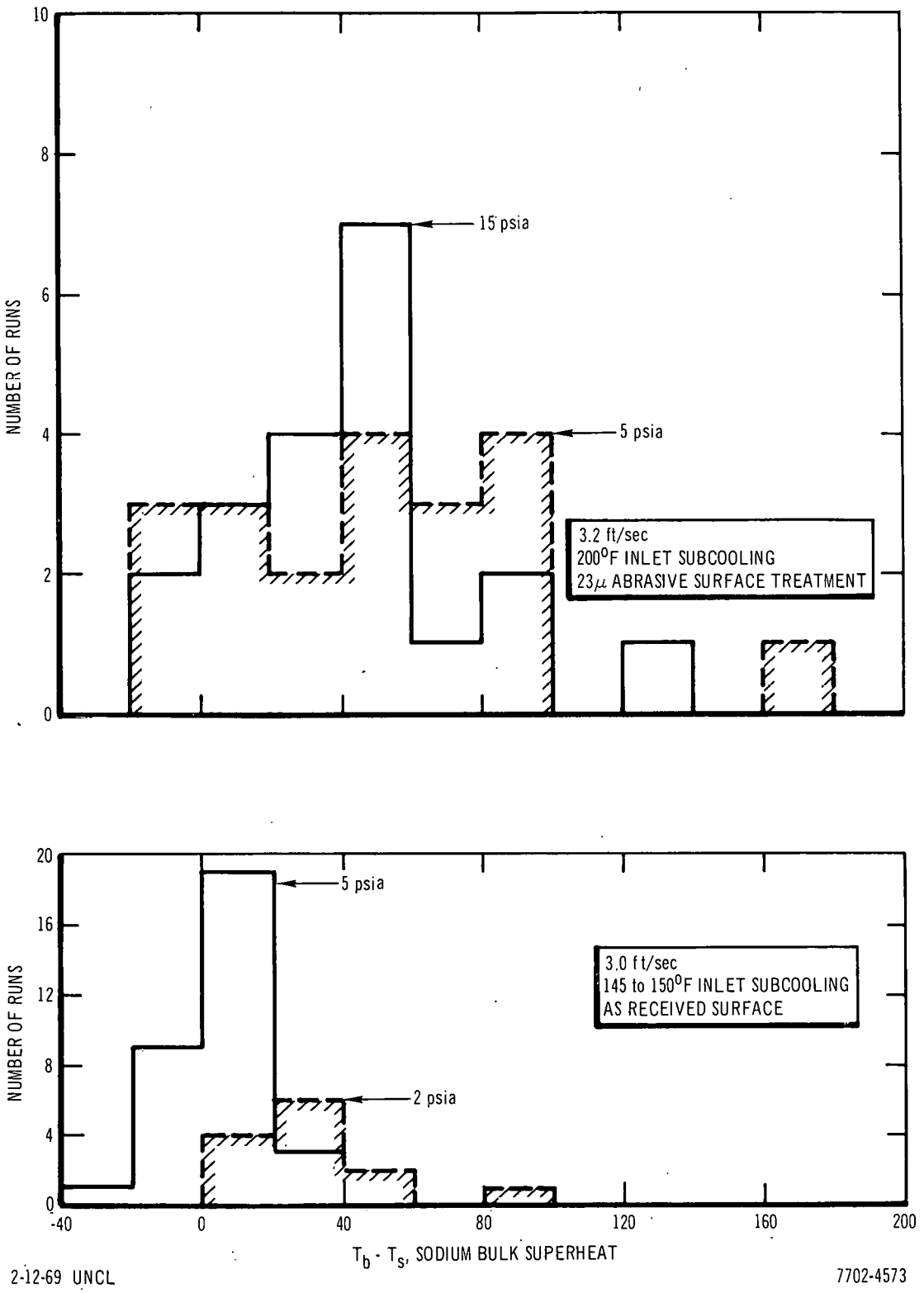

Figure 30. Histogram for Pressure and Surface Effects

superheat at lower pressure is in accordance with more detailed predictions based on the use of the Laplace formula and the liquid-vapor pressure temperature curve for sodium.[19] (See Section IV.)

Figure 31 is a superheat map utilizing Figures 24 and 30 and presents the major influential variables. The figure shows bulk superheat as a function of heat flux, with fluid velocity as a parameter, for fixed inlet subcooling. The effect of pressure level is shown by the shaded areas (representing data distribution for the lowest velocity) and it is seen that superheat decreases with increasing pressure.

5. Summary of Experimental Results

1) By means of reliable 15-in. long stainless steel clad, high flux heaters and an effective boiling detection system, extensive boiling inception superheat data were obtained for sodium flowing in an annulus, at pressures up to 15.3 psia and heat fluxes up to 0.825×10^6 Btu/hr-ft^2.

2) Major trends, but not incipient boiling superheat, for sodium can be predicted from all-liquid heat transfer considerations. Sodium bulk superheat increases with increasing net heat flux and, for a given heat flux, bulk superheat decreases both with increasing inlet subcooling and increasing velocity.

3) Wall (or bulk) superheat increases as pressure decreases. The pressure effect appears as a difference in data distributions, superimposed on an all-liquid heat transfer representation involving heat flux, velocity, and inlet subcooling. (See Figure 31.)

4) For otherwise similar conditions, the smoothest initial heater surface (23μ abrasive) produced somewhat greater bulk superheat than the next smoothest surface (600 grit abrasive). This difference held throughout the testing period (up to 40 runs before resurfacing) and no essential difference in incipient boiling superheat was detected between initial and final runs made on a given heater. For a severely corroded heater surface (after 170 consecutive runs) wall superheat was noticeably less than for the same heater in the initially smooth condition.

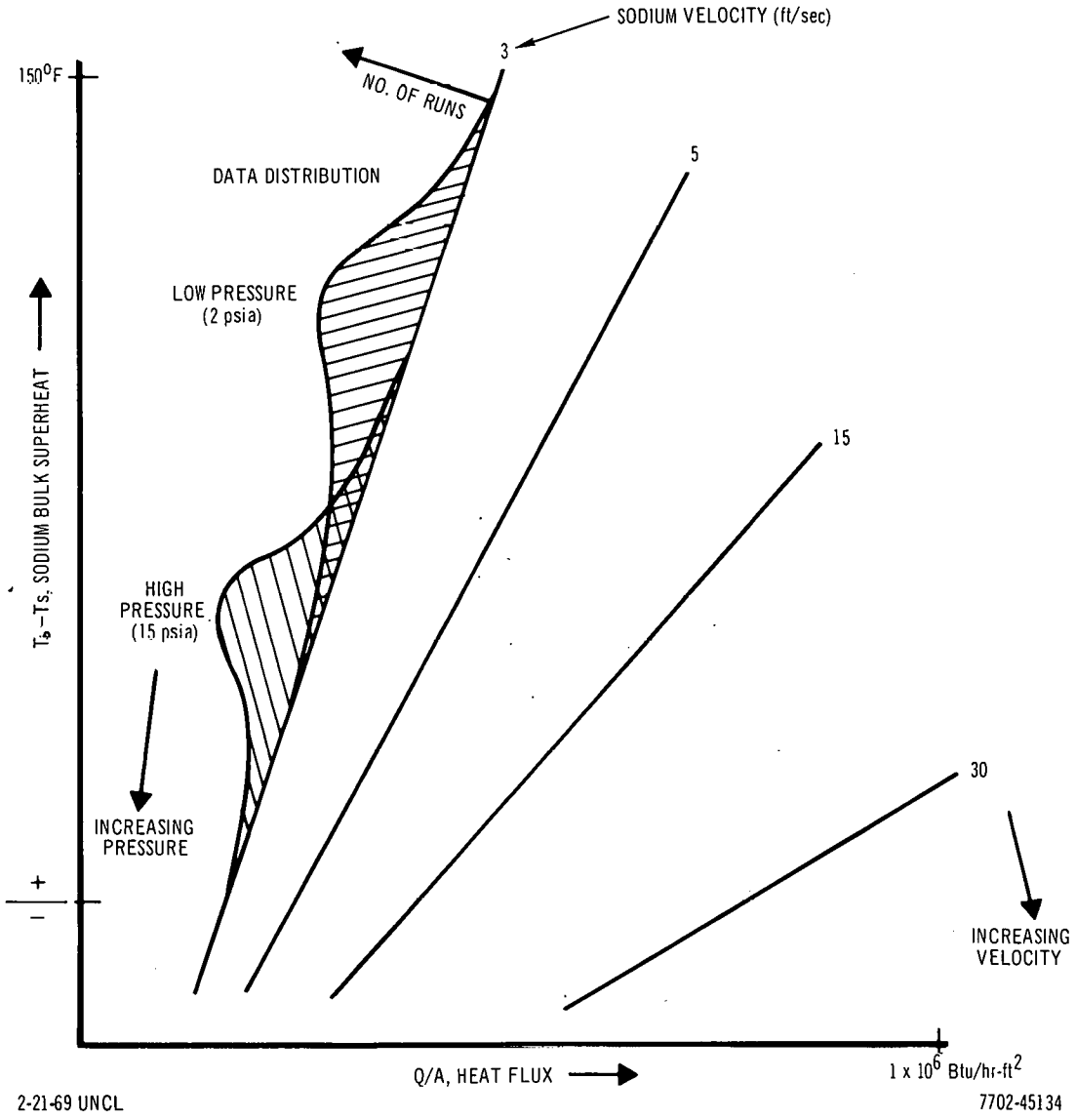

Figure 31. Superheat Map

C. APPLICATION OF TEST RESULTS TO LMFBR FLOW COAST DOWN ACCIDENT

The trends expected for a simplified LMFBR flow coast down accident in which power remains at 100% while flow decreases from 100 to 25% in 15 sec[26] can be deduced from Figure 31. If a heat flux corresponding to 100% power is chosen* and fluid velocity is followed as it decreases from 30 to 7.5 ft/sec, the bulk superheat increases from a negative to a positive value. Even for boiling initiation at 7.5 ft/sec, the low superheat indicates that the desirable bubbly flow pattern, rather than slug flow, would likely prevail. Similarly, for an overpower situation at full flow, the initiation superheat will increase but, because of the low positive bulk superheat, the onset of boiling will be accompanied by bubbly flow.

Based on Figure 31, the only LMFBR situation in which the rapid formation of a vapor slug appears to be possible would be a flow condition of less than 4 ft/sec, which is below the minimum flow usually required prior to initial rod withdrawal.

*In this example both the pressure and inlet subcooling are assumed to be constant. In an actual case, the inlet subcooling would probably decrease as the system pressure drops. To deal with such a case, knowledge of the pressure influence on superheat data distribution at high velocities is required but is not known at this time.

IV. THEORY OF BOILING INITIATION

A. SURVEY OF EXISTING MODELS

Consideration of the initiation of boiling in the turbulent flow of liquid metals requires a survey of the different boiling initiation models and assessment of such models for suitability of application to LMFBR conditions. Most of the available information concerning the initiation of boiling in liquid metals is either for stagnant conditions or laminar flow and can be shown not to apply to the forced flow conditions prevailing in the LMFBR.

To denote the outstanding differences among the existing theories, two extreme models for boiling incipience are first considered: The "Trapped Gas in Cavity Model" and the "Extended Rayleigh Model." Two other schemes, that of Hsu,[4] and an all-liquid heat transfer method are then considered.

In the Trapped Gas in Cavity Model, suggested by Holtz[5,27] Chen[6] and Dwyer,[7] it is assumed that the initiation of boiling takes place within an active cavity which contains some gas and that the only external parameter to be considered in the model is the system pressure. It is assumed that the penetration of liquid metal into the cavity is caused by the removal of scale inside the cavity by the liquid metal. The depth of the penetration depends on the maximum pressure[5] that the system has previously experienced. This model takes into account neither the hydrodynamic nor the thermal conditions existing in the channel. It is further assumed that the finish of the boiling surface is as-manufactured, with oxides present in the cavities, which have a wide spectrum of sizes ($\sim 10^{-2}$ to 10^{-6} in.).[6]

In contrast, recent experimental evidence[8] on the corrosive action of flowing liquid sodium on stainless steel surfaces under LMFBR conditions (immersed in flowing 1200°F sodium at heat fluxes of 10^6 Btu/hr-ft^2), shows that over a period of time the chromium and nickel are preferentially leached out of the surface and that etch pits of 40 to 80 μin. diameter appear in the grain boundaries.* Other studies[29] have also shown that the hot sodium easily penetrates 10^{-3} in. into surface microcracks. Thus, under LMFBR conditions the range

*A similar narrow range of pit sizes has been found by Davis and Anderson[28] on copper surfaces exposed to boiling water.

of sizes for boiling sites is very narrow and the cavities are thoroughly wet by the sodium.*

In the Extended Rayleigh Model the boiling process is assumed to occur in the bulk of a stagnant liquid medium, i.e., the growth of a vapor bubble takes place in an unbounded medium. This problem, in its hydrodynamic aspect, was first considered by Rayleigh in 1917. The combined thermal and hydrodynamic effects have been considered by Theofanous, et al.,[32] assuming variable condensation rates. The Rayleigh model holds for vapor generated in a liquid medium at rest and far from the influence of surrounding walls. (This process is similar to that which occurs in bubble chambers, where boiling in a superheated liquid medium is triggered by ionizing radiation.) In the LMFBR, the generation of vapor bubbles in the bulk of sodium coolant, if possible, is confined to only one trigger mechanism, that of elastic head-on collision of fast neutrons with sodium atoms.[33] Uncertainties concerning the percent of fast neutron flux, the elastic scattering cross-section for sodium in the range from 1 to 10 Mev, and the path-length of the recoil in sodium do not permit a clear-cut conclusion.[34]

The work of Hsu[4] initiated a more realistic approach to the description and interpretation of the onset of boiling. The simplified version of this concept is usually referred to as "Hsu's Criterion."[28,35] In Hsu's description, the incipient bubble is not confined within the cavity site as in the Trapped Gas in Cavity Model, but emerges from the cavity though remaining attached to it. This process is confined to the region of the thermal boundary layer adjacent to the heat transfer surface, in which a constant temperature gradient develops. Such a situation evidently prevails only in a liquid medium in which the turbulence does not affect the establishment of a substantial temperature gradient close to the heat transfer wall.

Hsu's criterion relates the equilibrium bubble diameter to the distance from the heat transfer wall by a condition of tangency on the superheat curve,

*Under these circumstances it is clear that the pressure-temperature history of the surface should have little effect on the incipient boiling superheat for forced convection systems. Dr. Louis Bernath[30] has suggested that the source of gas in the cavities may be in the metal itself, i.e., air-melted type 304 stainless steel contains ~0.1 wt % nitrogen, thereby providing an ample gas supply. This gas may diffuse through the thin stainless steel cladding and gather at grain boundaries in the surface, at 1500 to 1850°F during boiling transients.[31]

i.e., the temperature characteristic curve of the incipient bubble is tangent to the thermal gradient profile in the liquid at the moment of equilibrium (Figure 32). The temperature characteristic curve for the spherical bubble is obtained by the Laplace formula and either the Clapeyron formula or the pressure-temperature values for thermal equilibrium.

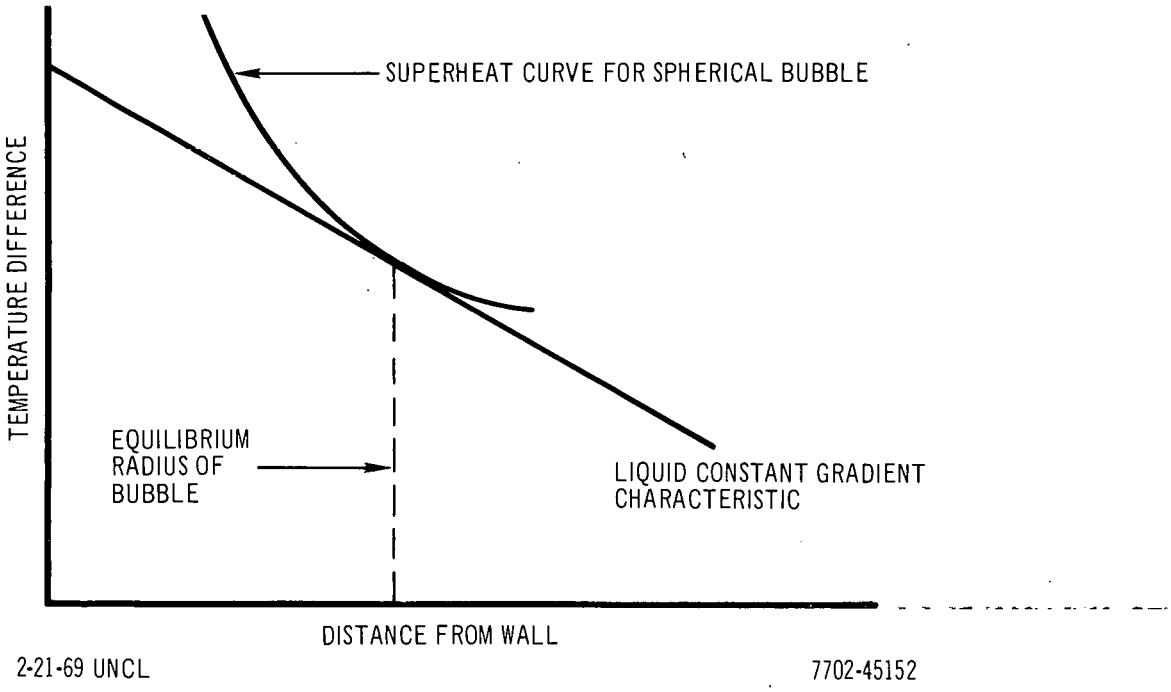

Figure 32. Graphical Interpretations of Hsu's Criterion

In Hsu's model, a hemispherical bubble is usually considered,[36] but this is not a requirement and non-hemispherical bubbles are sometimes considered.[28]

This criterion does not account for the existence of cavity sites or for the presence of vapor or gases in the cavities; but these inadequacies cannot be a serious objection to Hsu's criterion, since it has been successfully used in predicting wall superheating in ordinary liquids.[28]

The serious difficulties with Hsu's criterion arise when it is applied to liquid metals, particularly when turbulent flow prevails, since the Prandtl

number,* Pr, indicates that liquid metals behave differently from ordinary liquids when thermal and viscous processes occur (Figure 35 and Table 5). In addition to this material property, not only the wall surface, but also the bulk of the liquid can be brought to temperatures above the saturation temperature in liquid metal cooled heat transfer systems. If the thermal gradient for the liquid adjacent to the heat transfer surface is used in Hsu's criterion, the tangency condition leads to very low incipient boiling wall superheats and very large radius for incipient bubbles in liquid metals.

Marto and Rohsenow[36] tried to adapt Hsu's criterion to incipient pool boiling of sodium by abandoning the tangency condition and predicting the onset of boiling from only the size of the cavities and the bubble characteristic curve (Figure 33). In their scheme, the wall superheating behavior at different heat transfer rates is predicted by pivoting the thermal gradient of the liquid adjacent to the wall around the point in the superheat curve determined by the existing cavity sizes. This attempt by Marto and Rohsenow for pool boiling (i.e., with negligible viscous forces) is apparently the only one to date to adapt Hsu's ideas for liquid metals.

A different scheme for predicting boiling inception in forced flow sodium, the all-liquid heat transfer approach, was suggested by Collier.[15] This scheme was used by Kosky,[15] in conjunction with Davis and Anderson's analysis,[28] to determine surface cavity size from the steady state, forced convection boiling sodium data of Noyes and Lurie.[38] Subsequently, Kosky[15] used this information to predict critical heat flux, corresponding to boiling inception, for sodium and he claimed favorable comparison with experiment.[38] Since established boiling and incipient boiling are quite different phenomena, this interchange of results is questionable. The data[23] in Figure 34, clearly show the wall superheat for boiling inception at a given heat flux to be much greater than that for established pool boiling. Since the wall superheat is a major influence on calculated incipient bubble size, there is an evident contradiction in predicting

*By definition: $Pr \equiv \nu/\alpha$ where ν is the kinematic viscosity and α is the thermal diffusivity. In flowing media, where not only thermal, but also viscous processes take place, the Prandtl number is crucial because it relates both processes. Consequently, the onset of boiling in liquid metals is expected to behave differently than in common liquids.

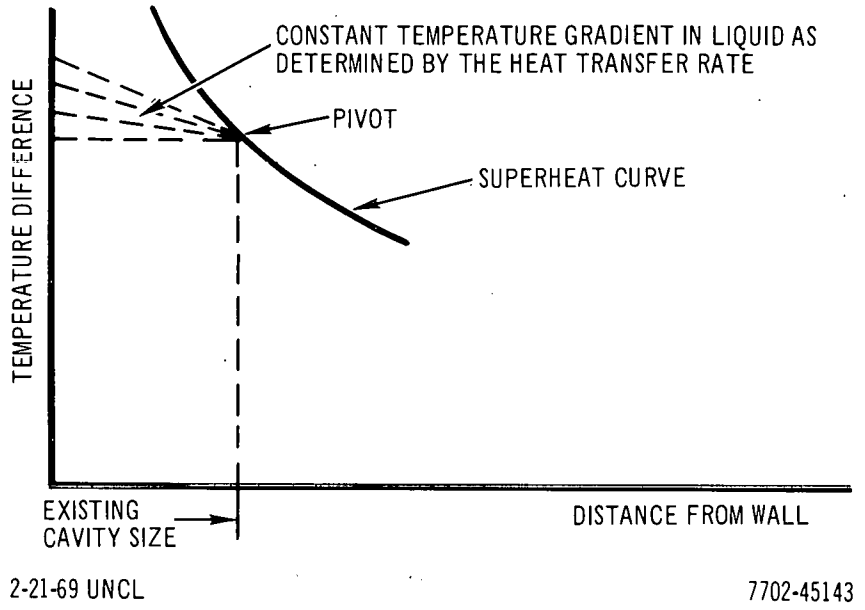

Figure 33. Modification of Hsu's Criterion for Incipient Pool Boiling of Sodium (After Marto and Rohsenow)

TABLE 5

PRANDTL NUMBER FOR COMMON LIQUIDS AND AIR

Fluid	Temperature Range (°F)	Prandtl Number Range	Reference
Glycerin	32 to 104	84.7×10^3 to 2.45×10^3	37
Engine Oil	32 to 320	47.1×10^3 to 84	37
Water	32 to 500	13.6 to 0.874	37
Air (14.22 psia)	32 to 212	0.712 to 0.690	37
Mercury	32 to 482	0.0288 to 0.0103	37
Sodium	800 to 1400 1400 to 2500	0.00487 to 0.00414 0.00414 to 0.00743	16

incipient boiling by the use of the cavity size obtained from established boiling. Furthermore, use of the all-liquid heat transfer coefficient and film temperature drop is not valid for established boiling conditions, since the boiling heat transfer coefficient is considerably greater for steady boiling than that for all-liquid conditions, as evidenced by the large reduction in film temperature drop.

B. DOMINANT PHYSICAL PROCESSES OCCURRING IN THE TURBULENT FLOW OF LIQUID METALS

Since turbulent flow prevails under LMFBR conditions, the main parameters are the channel Reynolds number, Re_c,* and the Prandtl number, Pr (the ratio of the kinematic viscosity and the thermal diffusivity). Martinelli[39] has shown the role of the Prandtl number during turbulent heat transfer in liquid metals. In the absence of a pressure gradient, a Prandtl number of Pr = 1 indicates that the thermal and the dynamic boundary layers possess the same thickness, i.e., the temperature and the velocity profiles are essentially the same at Pr = 1, as shown in Figure 35. With $Pr \ll 1$ (liquid metals) the ratio of the temperature drop in the laminar sublayer to the temperature drop in the turbulent zone is much smaller than the ratio of the corresponding velocity differences, because the phenomenon of molecular transfer of heat prevails over that of the molecular transfer of momentum. This argument reverses when Pr > 1. In the graphical representation[39] (Figure 35), the temperature profiles for Pr > 1 are on the upper side of the velocity profile while the temperature profiles for Pr < 1 are on the opposite side.

Attention should be focused on the laminar sublayer ($0 < y^+ < 5$), where the incipient bubbles are located; but, from Martinelli's results it is clear that the thermal gradient effects, which are the essential ingredient in Hsu's criterion, are insignificant in liquid metals. The low Prandtl number in liquid metals makes it possible to disregard the thermal effects, with respect to the viscous effects, in the laminar sublayer adjacent to the heat transfer surface.

---

*By definition $Re_c \equiv l^* u/\nu$, where ν is the kinematic viscosity, l^* is the characteristic length of the flowing channel, and u is the characteristic velocity. The onset of boiling at $Re_c \rightarrow 0$ (pool boiling conditions reported by Marto and Rohsenow) is a limit far removed from the situation prevailing in the LMFBR, so the conclusions at $Re_c \rightarrow 0$ are not applicable to LMFBR conditions a priori. Discontinuous behavior in the onset of boiling is expected to occur with the transition from laminar to turbulent flow regimes.

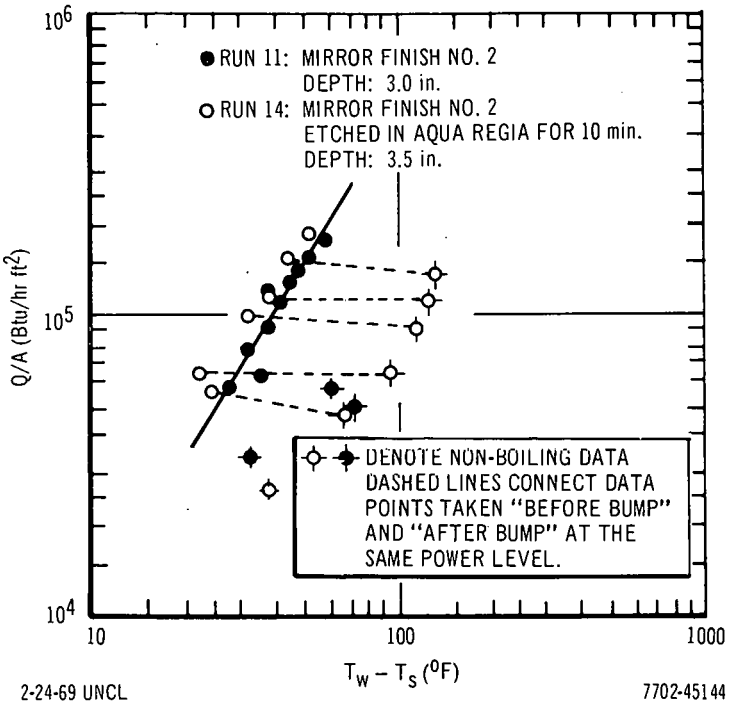

Figure 34. Sodium Boiling Inception Data of Marto and Rohsenow

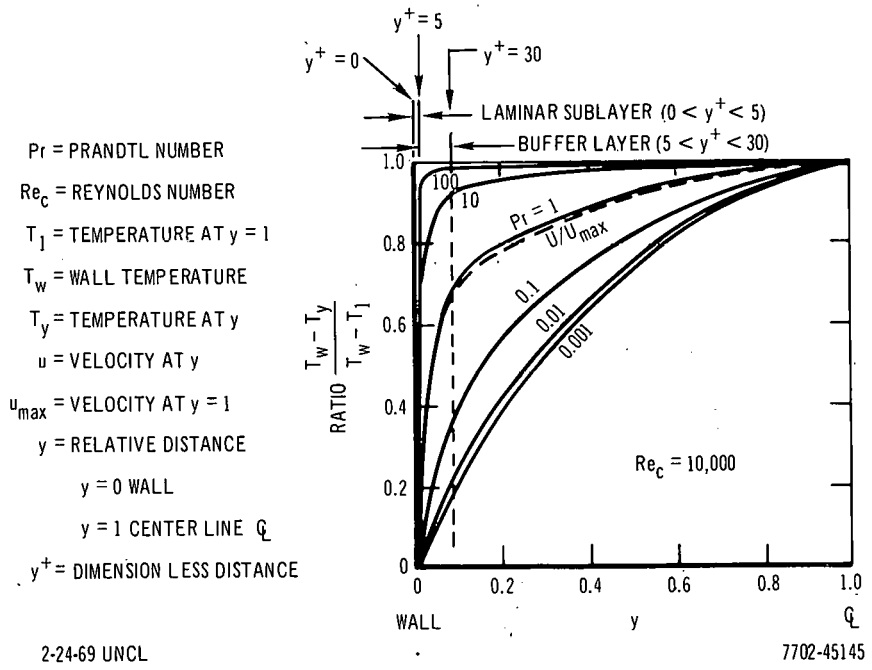

Figure 35. Martinelli's Results for Relative Temperature Profiles

Results from the present experiment (Appendix I), obtained during turbulent flow, allow us to compare the dominant forces influencing the initiation of boiling and to corroborate the above conclusions.

The results for an annular channel configuration, with heat being supplied from the internal wall, are summarized below:

1) In the laminar sublayer adjacent to the heat transfer surface (inner surface of the annular channel) there exists practically no thermal gradient. The thickness of the laminar sublayer is associated[40] with a dimensionless distance $y^+ = 5$, and the thermal gradient is computed either by the heat transfer coefficient, using the correlation for the liquid phase in annular channels[19] and the given temperature difference $T_w - T_b$, or by the heat flux Q/A together with the thermal conductivity of sodium. As a result, a temperature difference in the laminar sublayer of the order of 1°F is obtained.

2) The radius of the spherical bubbles at the onset of boiling are smaller than the thickness of the laminar sublayer; consequently, thermal effects do not have to be considered. This limits the number of participant forces to:

   a) Buoyant forces, because of the difference in densities between the liquid and vapor phases. (It is shown in Section IV-C that the buoyant forces are unimportant in forced convection boiling of sodium.)

   b) Drag forces, exerted by an essentially viscous flow (laminar sublayer) on the emerging vapor bubbles.

   c) Surface tension forces at the vapor-liquid interface are responsible not only for the higher pressure in the bubbles but also for holding the vapor bubbles to the heat transfer surface at the cavity sites.

3) The ratio of volumes between the incipient bubbles and the original cavity sites is of interest because of the possible influence of gases and vapors other than sodium on the onset of boiling. The radius of the incipient bubbles is obtained by using the Laplace formula for spherical bubbles, while the cavity size is obtained experimentally

with the aid of electron microscopy using replicas of the boiling surface (see Section III). The experimental evidence derived from measured superheat distributions shows that, as the volume of the incipient bubbles is much greater than the volume of the cavity sites, the amount of original gas or vapor is negligible with respect to the amount of vapor contained in the released bubbles at the onset of boiling. In consequence, any dependence of the onset of boiling on the previous history of the system is minimized for the LMFBR situation.*

C. ANALYSIS

The maximum superheat data for incipient boiling in flowing sodium, in the Forced Convection Loop, at a system pressure of about 5 psia, were selected for comparison with analysis, because they cover a wider range of flow velocities, and consequently heat fluxes, than any other set of data at different pressures in the system.

The established parameters at the moment of incipient boiling during forced convection flow are:

1) System pressure, denoted by p_s in psia.

2) Flow velocity, u_b, in ft/sec.

3) Temperature of the flowing sodium, T_b, in °F.

4) Heat flux delivered to the sodium flow from the inner wall of the annular channel, Q/A, in Btu/ft^2-hr.

5) The conical boiling sites on Type 304 stainless steel exposed to the flowing sodium at 1200°F, and heat flux rates of 10^6 Btu/ft^2-hr for periods of about 600 hr, have been examined by stereo electron microscopy and shown to be in the range of 40 to 80 μin. in diameter and depth[8] (see Section III). Similar sites have been found on Type 304 stainless steel surfaces exposed to boiling transients in the Forced Convection Loop.

The physical properties of sodium are taken from Reference 16.†

*This result is in agreement with the picture developed from recent corrosion studies.[8,29]

†The use of the Clapeyron formula is avoided and with it the criticism pointed out by Dalle Donne.[41]

1. Conditions Prevailing Before Boiling Incipience

The liquid sodium flows upward along the annular channel (Figure 36) in a turbulent regime and removes the heat generated in the centrally located heater. The idealized situation assumes (1) a constant heat flux is delivered to the fluid across the inner wall; (2) the outer wall is a thermal insulator; and (3) that certain hydraulic and thermal conditions are met. The conditions are elaborated below.

a. Shear Stress

The total shear stress transferred to the walls is formally expressed by

$$\tau = f \frac{\rho_b u_b^2}{2g} \qquad \ldots(6)$$

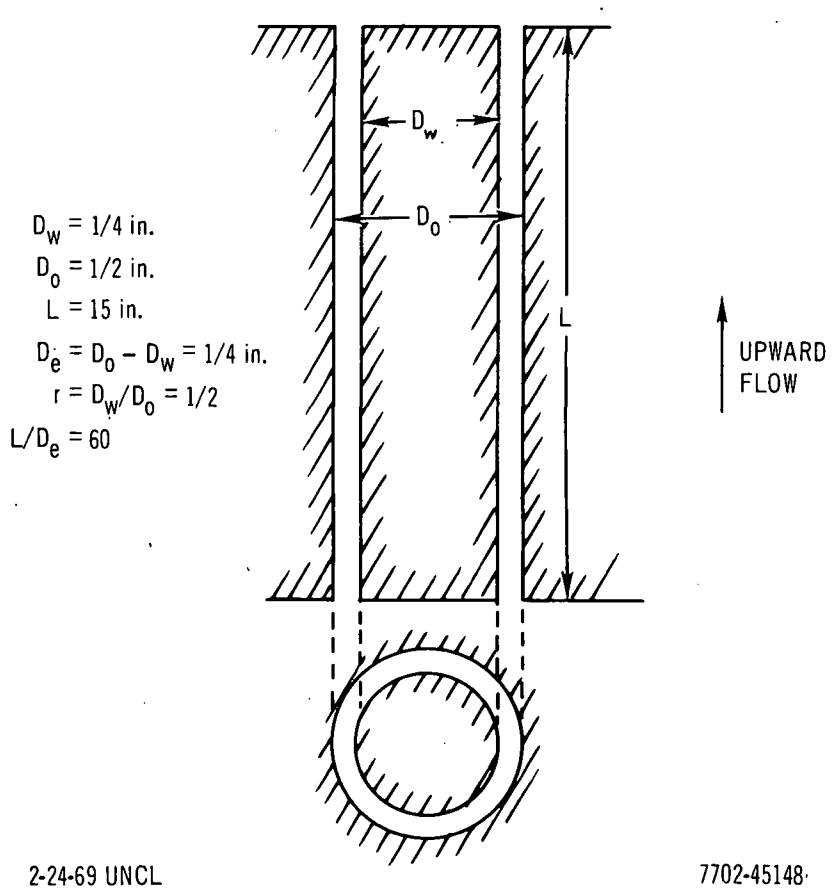

Figure 36. Experimental Channel Geometry

where the friction factor f, for smooth pipes and turbulent regime, is given by the empirical equation of Koo[40]

$$f = \frac{0.046}{Re_c^{1/5}} \quad . \qquad \ldots(7)$$

In the Reynolds number range

$$5 \times 10^3 < Re_c < 2 \times 10^5 \quad .$$

The total shear stress is neither at the inner nor the outer wall. In fact, per unit length of channel,

$$\tau(D_o + D_w) = \tau_w D_w + \tau_o D_o \quad ,$$

which in dimensionless form reads,

$$r + \tau^* = (1 + r)\frac{\tau}{\tau_w} \quad .$$

If the shear stress ratio τ^* is known, then

$$\tau_w = \frac{1 + r}{\tau^* + r}\tau \quad , \qquad \ldots(8)$$

and

$$\tau_o = \tau^* \tau_w \quad . \qquad \ldots(9)$$

The cylindrical surface, coaxial with the annular channel and in correspondence with the maximum velocity, is associated with the zero shear stress. In consequence, if D_z denotes the diameter of such cylinder, the shear stress ratio τ^* is shown to be,

$$\tau^* = \frac{\tau_o}{\tau_w} = \frac{D_o^2 - D_z^2}{D_z^2 - D_w^2} = \frac{1 - \bar{s}^2}{\bar{s}^2 - r^2} \quad ; \quad D_w < D_z < D_o$$

where $\bar{s}$ denotes the diameter ratio

$$\bar{s} \equiv \frac{D_z}{D_o}$$

It was proposed by Kays and Leung,[19] that

$$s^* = r^{0.343} \qquad \ldots(10)$$

where the ratio s^* is taken, by definition, as

$$s^* \equiv \frac{\bar{s} - r}{1 - \bar{s}}$$

Thus

$$\bar{s} = \frac{s^* + r}{1 + s^*}$$

and

$$\tau^* = \frac{1 + \bar{s}}{\bar{s} + r} \cdot \frac{1}{s^*}$$

becomes

$$\tau^* = \frac{r + 1 + 2s^*}{(r + 1)s^* + 2r} \cdot \frac{1}{s^*} \qquad \ldots(11)$$

For the present channel geometry,

$r = 1/2$

$s^* = 0.788$

$\bar{s} = 0.721$

$$\tau^* = 1.79$$

$$\tau_w = 0.656\tau$$

$$\tau_o = 1.17\tau$$

For the conditions prevailing in the channel, the total shear stress τ is predicted by Equations 6 and 7.

b. Laminar Sublayer

The thickness of the laminar sublayer adjacent to the inner wall is of interest for the onset of boiling. If the fluid is considered as incompressible, and the curvature of the wall is neglected, the demarcation between the laminar sublayer and the buffer layer[40] takes place when both the dimensionless distance from the wall y^+ and the dimensionless velocity u^+ are equal to five, i.e.,

$$y^+ = u^+ = 5 \quad . \qquad \ldots(12)$$

The friction velocity u^*, a function of the shear stress at the inner wall, is

$$u^* = u_b \sqrt{\frac{f}{2}\frac{\tau_w}{\tau}} = \sqrt{g\frac{\tau_w}{\rho_b}} \quad .$$

Hence

$$y^+ = y\frac{\rho_b u^*}{\mu_w} = y\frac{\sqrt{g\tau_w\rho_b}}{\mu_w} \quad ,$$

and

$$u^+ = \frac{u}{u^*} = \sqrt{\frac{\rho_b}{g\tau_w}}\,u \quad .$$

The thickness of the laminar sublayer is

$$y = \frac{5\mu_w}{\sqrt{g\tau_w\rho_b}} \quad . \qquad \ldots(13)$$

The velocity profile and the thickness of the laminar sublayer are shown in Figure 37.

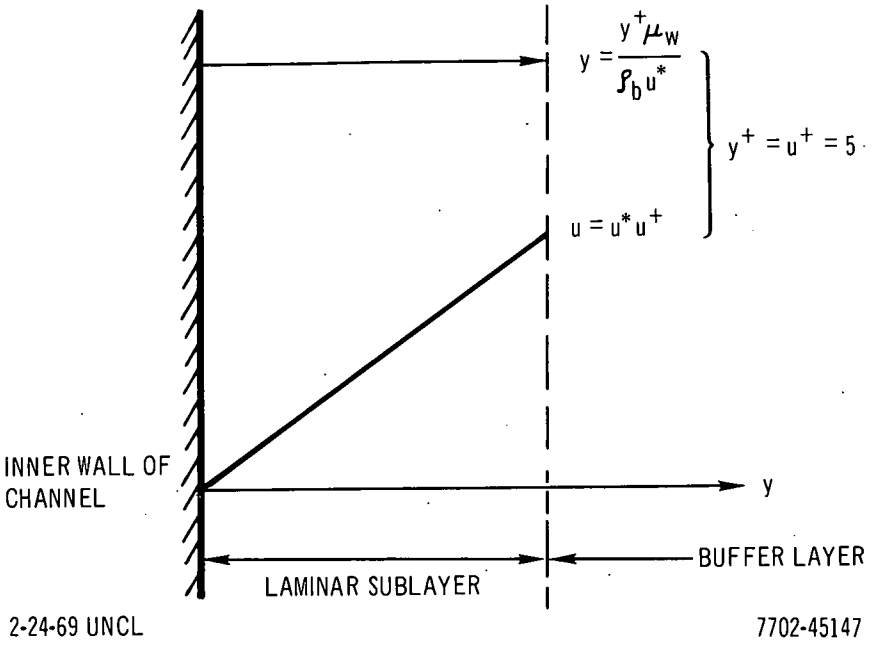

Figure 37. Isothermal Laminar Sublayer

c. Heat Transfer Characteristics

For given geometry and thermal boundary conditions (e.g., constant heat flux or constant wall temperature, adiabatic outside wall) prevailing in the channel, there exists a limiting Nusselt number Nu_l, which is considered the minimum Nusselt number for forced convection. Therefore, the forced convection range for the Nusselt number* spans the range

$$Nu_l \leq Nu < \infty$$

where the case $Nu \rightarrow \infty$ (or $h \rightarrow \infty$) corresponds to the thermal equilibrium conditions (isothermal system).

The usual graphical representation (Equation 3, Section III-B-2) for heat vs wall temperature minus bulk temperature, which gives a slope equal to the heat transfer coefficient h, can be modified to dimensionless variables as tabulated below.

*By definition $Nu \equiv h \cdot D_e/k$ where h is the all-liquid heat transfer coefficient, D_e is the equivalent diameter, and k is the thermal conductivity.

Item	Usual Variable	Dimensionless Variable
Abscissa	$T_w - T_b$	Pr^2Gr
Ordinate	Q/A	Pr^2GrNu
Slope	h	Nu

Pr and Gr denote the Prandtl and Grashof numbers, respectively. When these dimensionless variables are chosen, the natural convection characteristics for the vertical annular channel are represented by two straight lines on a log-log scale: One line for laminar natural convection, and the other for turbulent natural convection. The situation for the experimental channel is shown in Figure 38; the natural convection characteristics* of this figure are valid as long as boiling does not occur. The natural convection characteristics are obtained from the recommended correlations by Kutateladze et al.[42] and are used in the limit $Pr \rightarrow 0$.

The Nusselt number is a function of the Reynolds and Prandtl numbers during forced flow, so when these two dimensionless numbers Re_c and Pr are specified, they determine a definite line in the forced convection region of Figure 38. The limiting Nusselt number ($Nu_\ell = 6.181$) is theoretically calculated for the experimental channel using the results from Reference 43, and it corresponds to the laminar flow regime.

The main purpose of Figure 38 is to show the different ranges of heat transfer coefficients prevailing for natural and forced convection before the onset of boiling. As all liquid correlations have been shown to be valid up to the moment of boiling inception (see Section III), it is clear that at the same differential temperatures (wall minus bulk) larger heat removals are associated with forced flows, independent of the prevailing flow regime. The Nusselt number for the turbulent flow regime can be obtained by using the interpolation tables.[19] When results at about the same system pressure are considered, the Prandtl number remains almost constant, and the Nusselt number is then practically determined by the Reynolds number alone. The fluid flow and thermal characteristics of the experimental channel, for the selected runs, are shown in Tables 6 and 7.

*The ratio L/D_e must be observed since Nusselt numbers based on the equivalent diameter D_e, instead of the length L, are considered in Figure 38, to compare the Nusselt numbers for natural and forced convection.

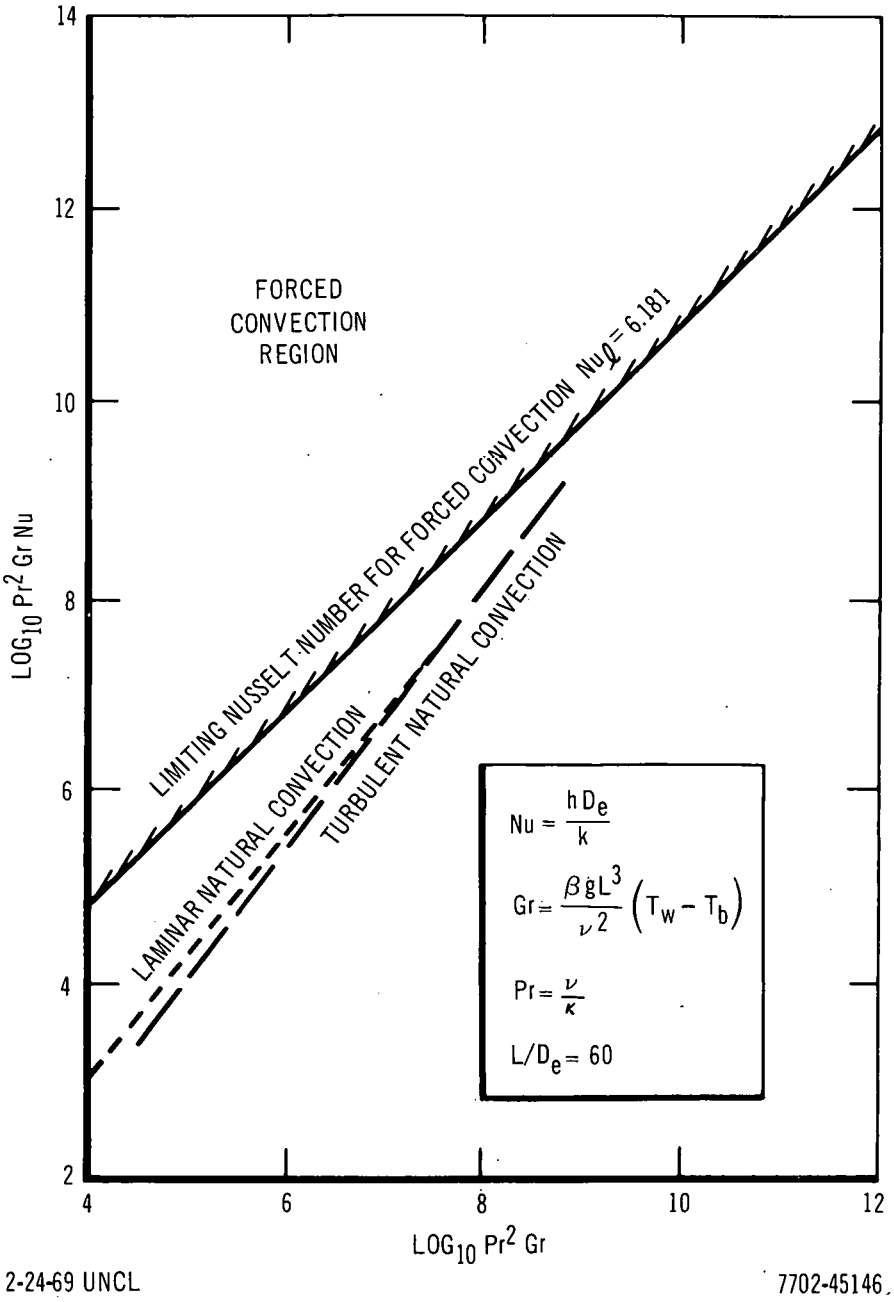

Figure 38. Experimental Channel Heat Transfer Characteristics

TABLE 6

FLUID FLOW CHARACTERISTICS OF THE ANNULAR CHANNEL
(r = 1/2)

Run	p_s		T_s	$T_b - T_s$	T_b	ρ_b	μ_b	u_b	Re_c	f	τ	τ_w	τ_o
	(psia)	(atm)	(°F)	(°F)	(°F)	(lb/ft^3)	$\left(\frac{lb}{ft\text{-}hr}\right)$	(ft/sec)	(10^4)	(10^{-3})	(lb/ft^2)	(lb/ft^2)	(lb/ft^2)
B-77	5.23	0.356	1434	65	1499	47.2	0.411	2.17	1.87	6.43	0.0222	0.0145	0.0260
JD-6	5.05	0.344	1429	78	1507	47.1	0.409	3.17	2.74	5.96	0.0438	0.0287	0.0512
KB-26	4.98	0.338	1426	146	1572	46.6	0.397	3.22	2.83	5.93	0.0445	0.0292	0.0520
KB-14	5.04	0.343	1428	161	1589	46.4	0.394	3.26	2.88	5.91	0.0453	0.0297	0.0530
KD-34	5.01	0.341	1427	71	1498	47.2	0.411	4.03	3.47	5.69	0.0677	0.0444	0.0791
KD-17	5.92	0.403	1454	55	1509	47.1	0.409	5.99	5.16	5.26	0.138	0.0905	0.161

TABLE 7

HEAT TRANSFER CHARACTERISTICS OF THE
ANNULAR CHANNEL
(r = 1/2; Pr = 0.0042)

Run	Re_c	Nu_w	k_b	h	Q/A	$T_w - T_b$	T_w	p_w		$\Delta p = p_w - p_s$
	(10^4)		$\left(\frac{Btu}{ft\text{-}hr\text{-}°F}\right)$	$\left(\frac{10^3 Btu}{ft^2\text{-}hr\text{-}°F}\right)$	$\left(\frac{10^6\ Btu}{ft\text{-}hr}\right)$	(°F)	(°F)	(psia)	(atm)	(atm)
B-77	1.87	6.31	29.9	9.05	0.310	34	1533	9.35	0.636	0.280
JD-6	2.74	6.33	29.7	9.01	0.807	90	1597	13.2	0.898	0.554
KB-26	2.83	6.33	28.7	8.71	0.490	56	1628	15.4	1.048	0.710
KB-14	2.88	6.33	28.4	8.62	0.759	88	1677	19.5	1.329	0.986
KD-34	3.49	6.34	29.9	9.07	0.595	66	1564	11.1	0.754	0.413
KD-17	5.16	6.40	29.7	9.10	0.559	62	1571	11.5	0.782	0.379

2. Incipient Boiling

The size and magnitude of the forces acting upon the departing bubbles for incipient boiling can be determined from the experimental data.

a. Size of Departing Bubbles

The departing bubbles are assumed to be brought into existence from the active nucleation sites on the heat transfer surface. For a given gaseous vapor volume, the spherical surface enclosing it is known to possess the minimum area (i.e., the minimum interface energy due to surface tension). Therefore only spherical bubbles are considered in this analysis. The Laplace formula relates the differential pressure, or wall superheat pressure, $\Delta p = p_w - p_s$, to the radius of the bubble, a,

$$\Delta p = 2\sigma/a \qquad \ldots(14)$$

where σ stands for the surface tension.

The system pressure p_s is a measurable parameter — that is the pressure of the bulk flow — while p_w is the pressure of the saturated vapor contained in the departing bubble, which is essentially at the temperature of the heated surface. In the present case the heated surface is the inner wall of the annular channel.

b. Comparison of Forces Acting Upon Incipient Bubbles

The departure of bubbles during stable boiling has been observed in forced flow of water[44] and was attributed to overcoming of the surface tension forces by the buoyant forces. During the present experiments on incipient boiling in sodium, the buoyant forces can be shown to be ineffective when compared to the surface tension and drag forces. Table 8 shows a comparative estimate for the buoyant, surface tension, and drag forces for run KB-26. The bubble, which has emerged into the laminar sublayer, is assumed to be hemispherical. As a simplifying calculation for the drag forces, the case of an undeformable sphere in a uniform flow is considered as usual[44] except that the tangential velocity does not vanish at the surface of the sphere, i.e., slip flow prevails.[45] The assumption of an undeformable spherical bubble is correct since the surface tension force is greater than the drag force except in the region where the bubble is in contact with the wall surface. The small Reynolds numbers for the sphere justifies the use of the drag coefficient for Stokes flow ($Re_{sp} < 1$).

TABLE 8

ESTIMATED FORCES ACTING ON A HEMISPHERICAL BUBBLE
(Run KB-26)

Bubble Radius, a, (in.)	0.126×10^{-3}
Hemispherical Bubble Volume (ft^3)	2.43×10^{-15}
Liquid Sodium Density, ρ_b, (lb/ft^3)	46.6
Buoyant Force (lb)	0.113×10^{-12}
Equatorial Perimeter (ft)	66.0×10^{-6}
Surface Tension (lb/ft)	7.86×10^{-3}
Surface Tension Force (lb)	0.519×10^{-6}
Exposed Area Normal to Flow, A_e, (ft^2)	0.173×10^{-9}
Velocity Gradient, $u/y = g\tau_w/\mu_w$, (sec^{-1})	8.74×10^{3}
Velocity at Half Radius (ft/sec)	0.0459
Dynamic Viscosity (lb/ft-hr)	0.387
Kinematic Viscosity, ν, (ft^2/sec)	2.31×10^{-6}
Reynolds Number for the Sphere, Re_{sp}	0.417
Drag Coefficient, $C_d = 48/Re_{sp}$	115
Specific Kinetic Energy of Flow, q, (lb/ft^2)	1.52×10^{-3}
Drag Force, $C_d A_e q$, (lb)	0.030×10^{-9}

All of the forces are quite different in magnitude for the assumed hemispherical bubble; but if an intermediate situation between the hemisphere and the complete sphere is considered, it is possible to balance the surface tension and drag forces. In the present experiments, the departure of the bubbles is attributed to the overcoming of the surface tension forces by the drag forces, producing the detachment of the incipient bubbles.

c. Dimensionless Representation

The example outlined in Table 8 indicates that it is possible to explain the detachment of the incipient bubbles by considering only the drag and surface tension forces. There are two steps in such an analysis; the first step is to find the equilibrium conditions, which is the subject of this Subsection (IV-C-2). The second step is the search for the stability of these equilibrium conditions. This step is partially surveyed in Subsection IV-C-3. The drag forces acting on the bubbles have not been determined analytically. Some preliminary models for hemispherical bubbles (which do not apply in the case for sodium) have been reported.[46]

The following argument corresponds to the range of the experimental velocities from 2 to 3.3 ft/sec. If a balance exists between the surface tension and drag forces for the departure of bubbles at the moment of boiling inception, it is possible to establish a dimensionless relationship among the variables participating in the process. The surface tension force F_t is dimensionally proportional to the product (σa),

$$F_t \propto \sigma a \quad . \qquad \ldots(15)$$

The influence of the dimensionless contact angle cannot be taken into account in dimensional analysis. If the drag force F_d is assumed to depend upon: (1) the liquid viscosity, μ_w; (2) the velocity gradient in the laminar sublayer, $\left(\frac{u}{y}\right)_w$; and (3) the bubble radius, a (i.e., a characteristic dimension of the departing bubble) then,

$$F_d \propto \mu_w \frac{a^2}{g}\left(\frac{u}{y}\right)_w = \tau_w a^2 \quad . \qquad \ldots(16)$$

The ratio* between the surface tension and the drag forces is

$$\frac{F_t}{F_d} \propto \frac{\sigma}{\tau_w{}^a} \quad . \qquad \ldots(17)$$

The ratio of forces can be also expressed as

$$\frac{F_t}{F_d} \propto \frac{g\Delta p}{\rho_b u_b{}^2} \cdot \frac{1}{f} = \frac{Eu}{f} \qquad \ldots(18)$$

where Eu is the Euler number.†

If the ratio of forces remains constant, then in the laminar flow regime

$$EuRe_c = \text{const.}\,;(f \propto Re_c{}^{-1}) \quad ; \qquad \ldots(18')$$

and in the turbulent flow regime,

$$EuRe_c{}^{1/5} = \text{const.}\,;(f \propto Re_c{}^{-1/5}) \qquad \ldots(18'')$$

because of the friction factor dependence upon the channel Reynolds number.

In pool boiling, and perhaps in forced convection laminar flow, according to Marto and Rohsenow,[36] the sodium superheat for incipient boiling seems to be determined by the size of the largest unfilled cavities. In contrast, as shown in Table 9, the thickness of the laminar sublayer of the present forced convection experiments (all of them in well developed turbulent flow) is of the order of one mil. This thickness is sufficient to completely contain the departing bubbles

*This is not the ratio between the Reynolds and the Weber numbers, because the bubble does not face any characteristic velocity but most likely a velocity gradient.

†The Euler number is generally considered as $g\,\Delta p/\rho u^2$.[40] When in Δp the subtrahend is the gas pressure, the Euler number becomes the cavitation number,[47] except for a constant. In contrast, when superheating is considered, the gas pressure is the minuend in Δp. In this way, the Euler number is always positive.

TABLE 9

COMPARISON OF BUBBLE SIZE WITH LAMINAR SUBLAYER THICKNESS

Run*	σ (10^{-3} lb/ft)	a (10^{-3} in.)	τ_w (lb/ft^2)	μ_w (lb/ft-hr)	y (10^{-3} in.)	a/y	Eu Re_c^2 (10^{10})	Re_c (10^4)
B-77	8.22	0.333	0.0145	0.404	1.44	0.231	3.00	1.87
JD-6	7.97	0.163	0.0287	0.393	0.994	0.164	5.97	2.74
KB-26	7.86	0.126	0.0292	0.387	0.976	0.129	8.04	2.83
KB-14	7.67	0.0882	0.0297	0.379	0.951	0.093	11.3	2.88
KD-34	8.10	0.223	0.0444	0.398	0.809	0.276	4.42	3.47
KD-17	8.08	0.242	0.0905	0.397	0.566	0.428	4.09	5.16

*The runs shown represent the maximum superheats obtained in the respective groups and are for essentially constant pressure but for different heat fluxes, inlet subcoolings, and velocities.

when boiling is initiated. Under these conditions the laminar sublayer is too thin to support any significant change in temperature across it, due to the high thermal conductivity of the liquid sodium (about 28 Btu/ft-hr-°F at the wall temperature of the selected runs). It follows that the saturated vapor contained in the departing bubbles is essentially at the wall temperature, as already anticipated. To explicitly show the wall superheat pressure - velocity dependence of the process during turbulent flow, Equation 18'' for the Euler number Eu is multiplied by $Re_c^{9/5}$ to yield the product $EuRe_c^2$, which is a velocity-independent parameter,*

$$EuRe_c^2 = \text{const. } Re_c^{9/5} \qquad \ldots(19)$$

where $Re_c > 2100$.

Actually the critical Reynolds number (2100) is a lower limit for the use of Equation 19, as can be seen from the perturbation introduced by the bubbles in the laminar sublayer, which is proportional to the ratio a/y in Table 9.

In fact

$$\frac{y}{a} = \frac{y^+}{\sqrt{a\sigma g\rho_b}} \sqrt{\frac{\sigma}{a\tau_w}}$$

which on the previous assumption of $\sigma/a\tau_w$ = const., and disregarding the changes in the properties of sodium, becomes

$$y/a \propto a^{-1/2} \quad . \qquad \ldots(20)$$

As a decreases with u_b, the ratio y/a increases, i.e., the perturbation introduced by the bubbles in the laminar sublayer should decrease with increasing velocities. This indicates that Equation 19 should be more accurate at higher Re_c.

*The channel Reynolds number Re_c is used to remove the velocity from the Euler number, so $EuRe_c^2$ stands for a dimensionless pressure differential. Re_c is used not only because of its connection to the flow regime, but mainly because of the friction factor dependence upon it.

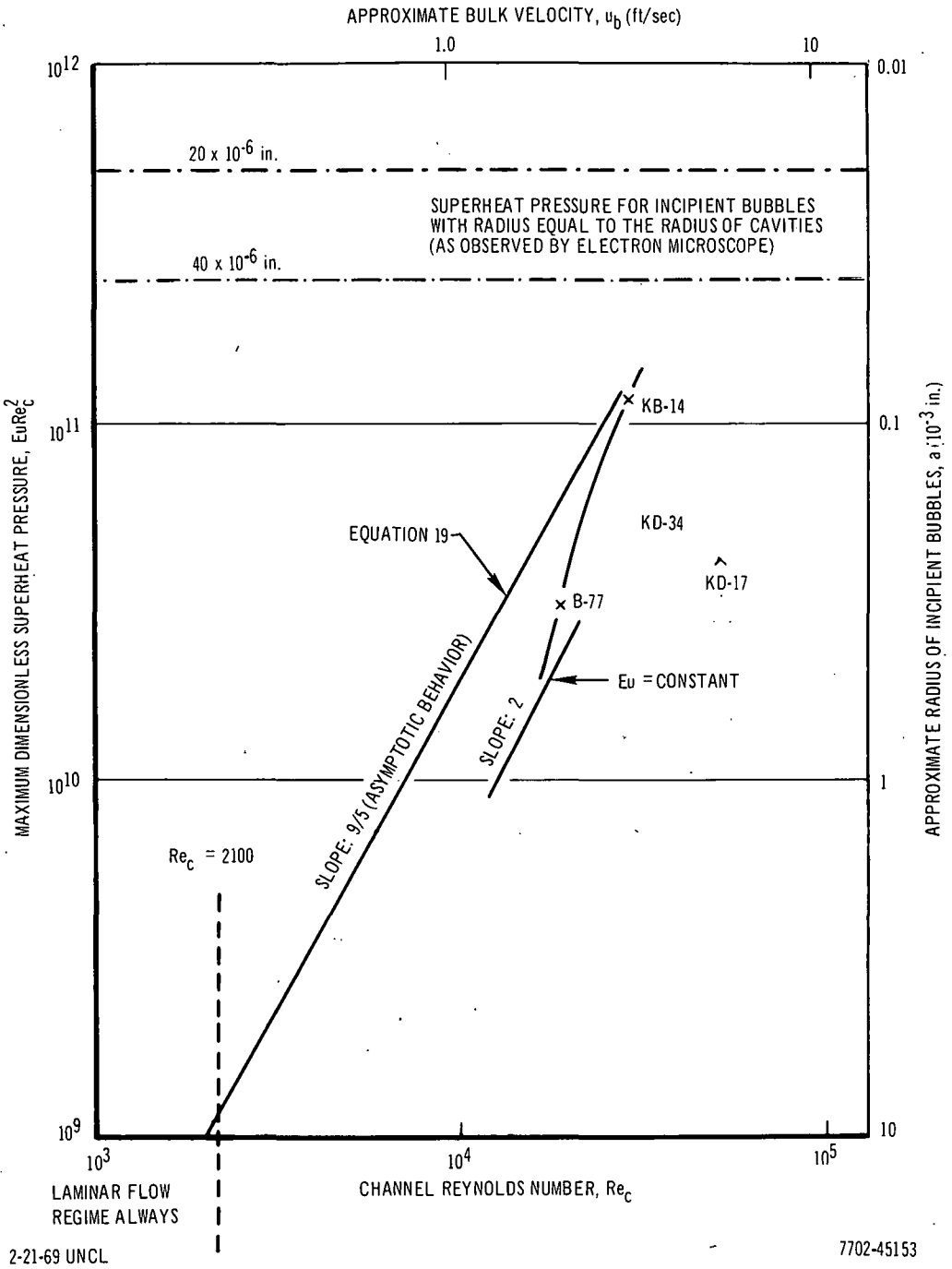

Figure 39. Dimensionless Representation of Superheat

The results from the experimental runs under consideration are shown in Figure 39 where $EuRe_c^2$ is the dimensionless-wall superheat pressure at the onset of boiling, while Re_c, as usual, is the dimensionless bulk velocity. The dependence indicated by Equation 19 is shown in Figure 39 which is based upon the runs with the largest Re_c in the velocity range of 2 to 3.3 ft/sec. This dependence is asymptotic because, as seen in Table 9 (first four runs) and from Equation 20, the perturbation introduced by a single bubble in the laminar sublayer vanishes as $Re_c \to \infty$. The approximate radius of the incipient bubbles and the bulk velocity of the liquid sodium are shown in the right and upper scales of Figure 39, respectively, for the present experimental channel and for the constant values

$$\rho_b = 47 \text{ lb/ft}^3,$$

$$\mu_b = 0.4 \frac{\text{lb}}{\text{ft-hr}}, \text{ and}$$

$$\sigma = 0.008 \frac{\text{lb}}{\text{ft}}.$$

3. Discussion of Analysis

In the above analysis, the number of participating parameters was minimized,* producing a hypothetical asymptotic dependence for wall superheat pressure vs velocity. Only the asymptotic dependence of the slope can be predicted for the logarithmic representation (Figure 39).

As already shown in Figure 39 the experimental data seem to approach this predicted dependence for large channel Reynolds number, Re_c, but the experimental velocities vary only from 2 to 3.3 ft/sec. The curve, using only two runs (B-77 and KB-14), is the maximum superheat pressure for incipient boiling, i.e., all the other data exhibit lower superheat pressures. The spread in the superheat pressures at constant Re_c indicates a situation of weak stability which is worthy of further study, even in this stage of the investigation. In fact, Section IV-B-2 and specifically Figure 39, clarifies that at the onset of boiling,

*Shown by the absence of the characteristic parameters for the cavity sites and the roughness of the heat transfer surface. The viscosity of the vapor contained in the bubble is tacitly ignored on the assumption of slip flow. In addition, it is implicit that an unknown function of the contact angle, β, affects the previous derivation, and it obviously cannot be handled by dimensional analysis.

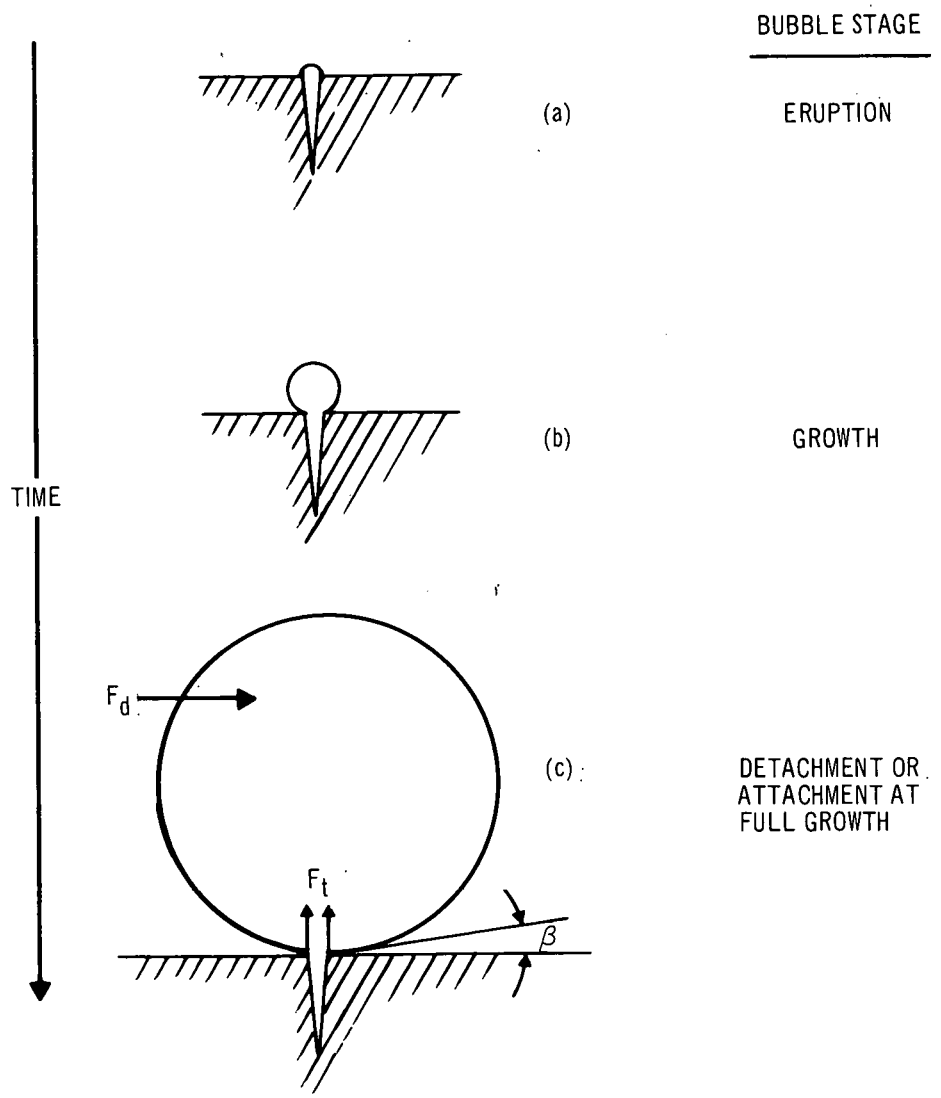

SITUATION	TIME	RADIUS	GROWTH RATE	DRAG FORCE
(a)	t_a	a_a (MINIMUM)	$\dot{a}_a^3 > 0$	$F_{da} > 0$
(b)	$t_b > t_a$	$a_c > a_b > a_a$	$\dot{a}_a^3 > \dot{a}_b^3 > \dot{a}_c^3$	$F_{dc} > F_{db} > F_{da}$
(c)	$t_c > t_b$	a_c (MAXIMUM)	$\begin{cases} 0 \text{ IF ATTACHED} \\ \dot{a}_c^3 > 0 \text{ IF DETACHED} \end{cases}$	F_{dc} (MAXIMUM)

2-24-69 UNCL

7702-45149

Figure 40. Evolution of the Incipient Bubble

the radius of the bubble is about one order of magnitude greater than the size of the cavity site. A small contact angle, β, as shown in Figure 40, is implied.

The incipient bubbles must grow from an initial size [the approximate size of the cavity site shown in Figure 40(a)] to a size whose radius at the onset of boiling [Figure 40(c)] could be about one order of magnitude greater than the initial size. A typical bubble occurring during this process is shown in Figure 40 in three different situations in its evolution [from (a) to (c)].

As the bubble radius in situation (a) is about 1/10 of the radius in situation (c) for the onset of boiling, it is clear that a quasi-static evolution of the bubble is not possible. Dynamic effects must be considered in order to account for the pressures required to keep the bubble growing; for instance, a sudden vaporization of the liquid sodium contained in a cavity could explain these dynamic effects. Furthermore, the ratio of densities (liquid to vapor) is of the same order as the ratio of the volume of detaching bubbles to the volume of the cavity sites, which is of the order of $(a_a/a_c)^3$, in a first approximation.* The designation of eruption then seems suitable for situation (a) in which liquid, in the cavity volume, is suddenly vaporized. From here on, the growth rate slows down, and the growth of the bubble is shown in situation (b). At the final condition, situation (c), the bubble is still in contact with the heat transfer wall, the dynamic effects due to the growth of the bubble are attenuated, and the bubble attachment to, or detachment from, the surface can be determined by means of the formulas derived for equilibrium conditions (see previous section).

Formulas (15) and (16) are indicated in Figure 41 as a function of the radius at situation (c), assuming that the flow of sodium remains invariable, i.e., constant shear stress. If $a_c < a^o$ the bubble would stay attached to the wall because the surface tension force, $F_t > F_d$, the drag force; but, if $a_c > a^o$ the bubble would detach from the wall because $F_t < F_d$.

In the present experiments the occurrence of the highest wall superheats at low system pressures can be explained with the aid of the liquid-vapor pressure-temperature curve[16] of the sodium. Since the present experiments are operated at a temperature far removed from the critical temperature, the Clapeyron formula can be used for illustrative purposes in this particular case, i.e.,

*An effective depth of the order of a_c is assumed for the vaporized volume in the cavity site.

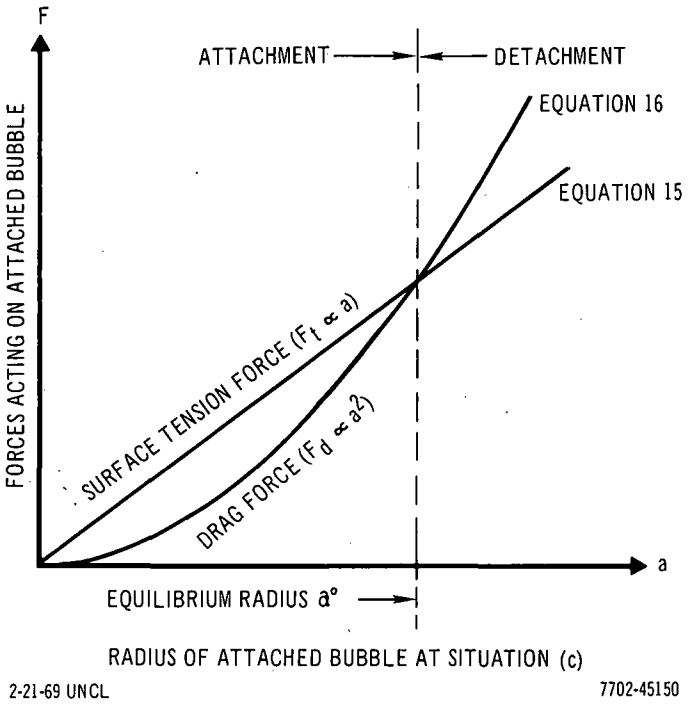

Figure 41. Surface Tension and Drag Forces Acting on a Constant Radius Bubble Attached to the Heated Surface

$$\Delta \log p \propto -\Delta \frac{1}{T} \quad ,$$

or

$$p = p^* e^{-B/T} \quad ,$$

where p^* and B are constants in the limited range of temperatures and pressures in the system.

At a given Re_c, the maximum wall superheat pressure Δp, is obtained from Figure 42. But, at different system pressures, the same Δp corresponds to different superheats. This situation is graphically illustrated in Figure 42 by relating the Clapeyron formula to Figures 39 and 43.

In contrast to Hsu's criterion, a thermal interpretation of the incipient boiling, the present interpretation is a dynamic one. However, it should be borne in mind that incipient boiling in the present interpretation is not entirely divorced from the heat transfer aspects. For instance, during the present superheat

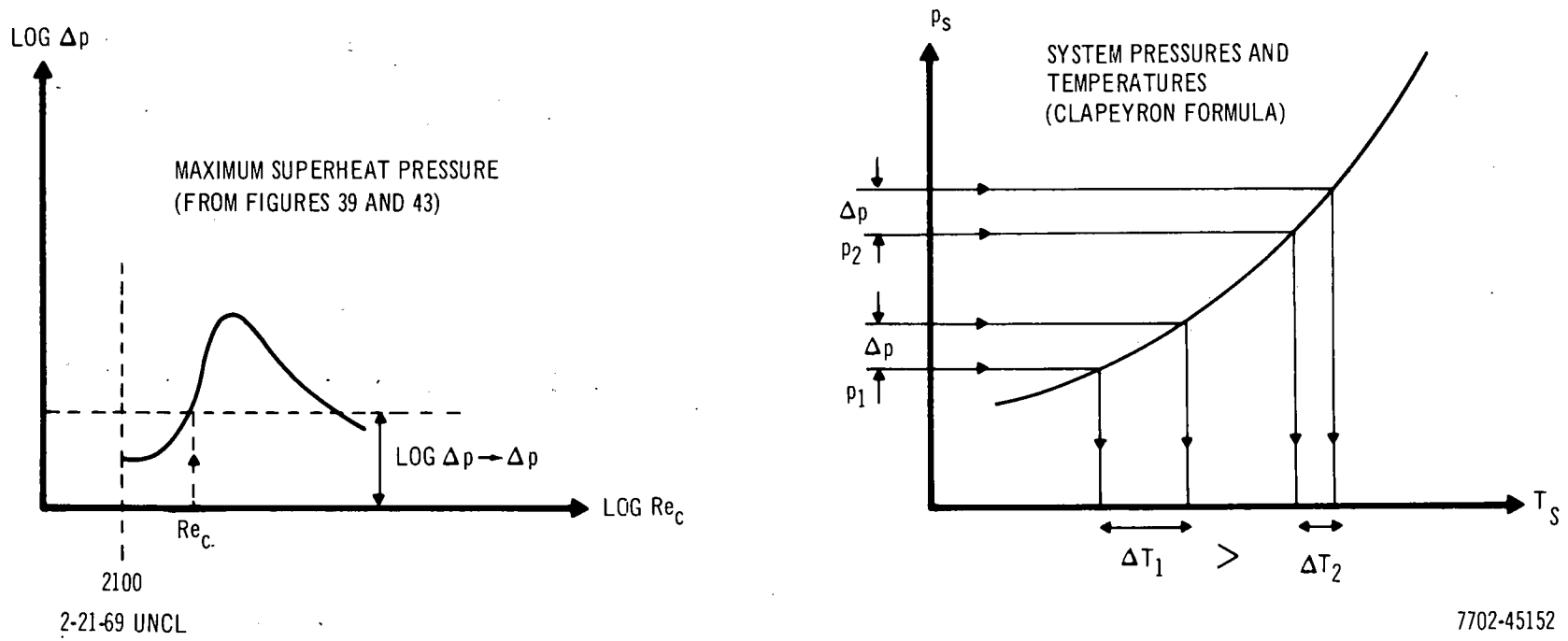

Figure 42. Maximum Wall Superheat for Incipient Boiling at Different System Pressures

tests, the experimental runs conducted by maintaining all the parameters constant but increasing the heat flux, lead to increased differential temperatures $\Delta T = T_w - T_s$ and consequently increased differential pressure $\Delta p = p_w - p_s$. At constant Re_c or constant u_b (i.e., constant dynamic effects) the maximum superheat corresponds to the maximum heat flux.

There are limitations on the asymptotic behavior predicted by Figure 39. These limitations are described below.

a. Spectrum of Cavities and Contact Angle

The relatively limited range for the spectrum of cavities is shown in Figure 39. The slope of the curve connecting the runs B-77 and KB-14 seems to approach the predicted asymptotic slope, but the curve cannot be indefinitely extended because when the bubble radius, a, approaches zero there are no cavities on the stainless steel surface small enough to support bubble growth.

The influence of the contact angle, which may vary both with temperature and with surface condition (aging effects) is believed to be reduced by considering only runs at constant pressure (about 5 psia). For a limited range of cavity sites, and if the contact angle remains constant, the validity of the expressions derived in Section IV-C-2 is also limited, and the claimed asymptotic behavior at high Reynolds number would never be reached.

b. Perturbation of Attached Bubbles

The bubbles which emerge into the laminar sublayer introduce a perturbation to the flow. This perturbation grows with increasing ratios of a/y. At low Reynolds number, the shear stresses are also low and the bubbles are bigger at the equilibrium situation. But — as Table 9 shows for Run B-77 — a/y = 0.231, indicating a significant perturbation to the laminar sublayer flow. If the attached bubbles behave as artificial roughness introduced to the wall, then at low Re_c, but still in turbulent flow, the law would tend to

$$EuRe_c^2 \propto Re_c^2$$

or

$$Eu = \text{const} \quad .$$

This result is reasonable since it is well known[45] that when the roughness of the walls is well in excess of the thickness of the laminar sublayer, the friction factor becomes independent of Re_c. Furthermore, for Eu = const, the slope is 2, as shown by Figure 39 at lower Re_c. But at still lower Reynolds numbers in turbulent flow, the wall superheat characteristic would tend to flatten. This effect can be expected from the fluctuations of the longitudinal and transverse components of the velocity to the mean flow in the laminar sublayer. Figure 39 shows an expected discontinuity at the transition of flow regimes, but in the present experiments the onset of boiling has not been investigated in the vicinities of $Re_c = 2100$.

c. Effect of Roughness* of Heat Transfer Surface

The roughness of the surface can be modified by corrosive action of the liquid sodium, but individual experimental runs at relatively high wall temperature (about 1800°F) are performed for short periods, and the effects of the initial roughness do not seem to be removed after several runs (see Section III).

In the LMFBR, a continuous and long exposure of the fuel element cladding to the liquid sodium flow produces a relatively smooth heat transfer surface.[8] By Equation 20, the perturbation a/y that the attached bubbles introduce into the laminar sublayer varies as the square root of a, which decreases with Re_c; consequently, the effect of roughness due to the attached bubbles also decreases with increasing Re_c. But if the roughness of the surface is still predominant, its perturbation would increase with increasing Re_c because y decreases with increasing Re_c.

The type of flow prevailing in the idealized laminar sublayer is the plane Couette flow shown in Figure 37. But this idealization refers to the time average values of the velocity in the range $0 < y^+ < 5$; and of course, it does not describe the instantaneous situations which are affected by the fluctuations in the velocity. With increasing values of Re_c, the shear stress also increases and wakes develop downstream of the obstacles to the flow, caused not only by

*In the present study, roughness is measured relative to the thickness of the laminar sublayer instead of to the diameter of the pipe as is usual in engineering correlations for the friction factor.

the attached bubbles, but also by the irregularities of the heated surface.* This effect apparently tends to decrease the drag force on the attached bubbles, and the present experiments, in fact, show a decreasing trend for the wall superheat pressure with increasing Re_c, as denoted in Figure 39, runs KD-34 and KD-17. An attached bubble is more voluminous than any single prominence in the heated surface; however, the population of the attached bubbles is less than the population of those prominences. Consequently the irregularities on the heated surface produce a more noticeable influence on the detachment of the bubbles, not only with decreasing bubble size but also with increasing bulk velocity (Reynolds number) in the channel.

The transition from an essentially unperturbed laminar sublayer to a sublayer exhibiting effects of wakes is denoted in Figure 27; this figure shows that the more polished surface (23μ abrasive) exhibits a broader distribution for the number of runs than the less polished surface (600 grit abrasive). The polishing effect thus is seen to create a number of small cavity sizes at the expense of the large cavities, while reducing the roughness of the surface.

Disregarding the boundaries imposed on the incipient spherical bubbles attached to one side of the heated surface by the heated surface itself and the growing turbulence on the other side, the situation is idealized as spheres in a uniform velocity gradient flow (i.e., plane Couette flow). The same argument applies to surface prominences. As in plane Couette flow, $(u/y)_w$ is the characteristic parameter in place of u, and the dimensionless group representing the Reynolds number for the sphere Re_{sp}

$$Re_{sp} = \frac{au}{\nu} \quad , \qquad \ldots(21)$$

*If we adhere to this idealization for the flow in the laminar sublayer, we may recognize that surface prominences and attached bubbles produce two different patterns downstream flow. This is because slip flow (no boundary layer effect) exists in the case of attached bubbles, in contrast to sharp velocity gradients (boundary layer effect) in the flow adjacent to the surface prominences. Flow separation, which often occurs after rigid obstacles facing uniform velocity flow, either does not occur or is postponed until higher velocities are reached, when slip flow takes place. An example of formation of eddies, instead of flow separation, is shown by Kenning and Cooper.(46)

in plane Couette flow becomes,

$$Re_{sp} \rightarrow \frac{a^2(u/y)w}{\nu} \quad . \qquad \ldots(21')$$

Similarly, if ℓ stands for the characteristic length of the prominences on the heated surface, Equation 21 becomes,

$$Re_{sp} \rightarrow \frac{\ell^2(u/y)w}{\nu} \quad . \qquad \ldots(21'')$$

When the bulk velocity u_b increases, (u/y)w also increases. As the bubble radius a increases with increasing u_b (at higher Reynolds number such as runs KD-34 and KD-17), it is clear, from Figure 39, that both Equations 21' and 21'' increase with u_b, the increase in Equation 21' being more pronounced than in Equation 21''.

Though the presently available runs at higher Re_c are sufficient to indicate the decreasing trend in the superheat pressure with increasing Re_c, they are insufficient to extrapolate the curve determined by the runs B-77 and KB-14 of Figure 39 into the range of higher Re_c ($Re_c > 3 \times 10^4$).

Studies of the maximum incipient boiling superheat for sodium with Re_c are summarized in Table 10, and shown schematically in Figure 43.

The maximum wall superheat pressure, whose behavior is indicated in dimensionless form in Figure 39, is understood to be independent of the pressure prevailing in the system. Actually, higher system pressures are related to higher temperatures, and some variation in the maximum wall superheat pressure Δp can consequently be expected with temperature (or pressure). However, this effect is not seen in Figures 39 and 43 where Δp is plotted in its dimensionless form, $EuRe_c^2$. The limits in the range of the Reynolds numbers, for Section 2 of Figure 43, depend on the geometry and the heat transfer surfaces participating in the process.

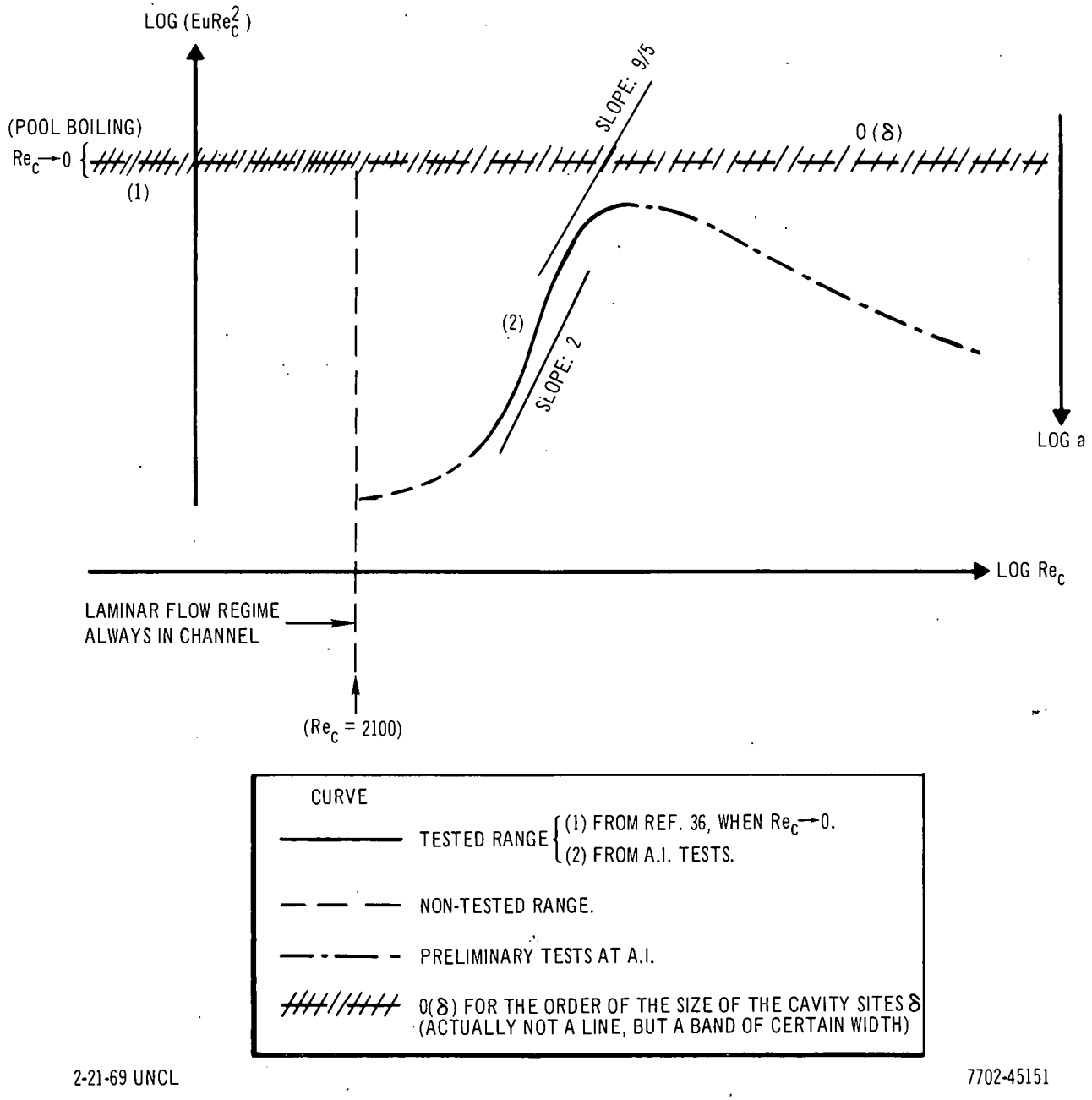

Figure 43. Maximum Incipient Boiling Superheat in Dimensionless Representation

TABLE 10

STUDIES OF MAXIMUM INCIPIENT BOILING SUPERHEAT FOR SODIUM

Reynolds Number, Re_c	Summary
$Re_c < 2100$	Experiments by Marto and Rohsenow[36] show that the size of the incipient bubbles is of the order of the size of the cavities for $Re_c \to 0$ (pool boiling).
$2100 < Re_c < 1.8 \times 10^4$	No test performed, but there is some evidence about the behavior.
$1.8 \times 10^4 < Re_c < 3 \times 10^4$	Tests asymptotically approach theoretical prediction ($Eu\ Re_c^2 \propto Re_c^{9/5}$) based on balance of drag and surface tension forces.
$3 \times 10^4 < Re_c < 5.6 \times 10^4$	Present tests show a decreasing superheat trend with increasing Re_c.
$Re_c < 5.6 \times 10^4$	No tests performed.

An explicit dimensionless form for the asymptotic behavior (i.e., in correspondence with the slope of 9/5 in Figure 43) is

$$\Delta p = p_w - p_s \propto (u_b)^{9/5} (D_e)^{-1/5} \qquad \ldots(22)$$

for constant material properties.

Similarly, for a slope of 2 in Figure 43, the maximum wall superheat pressure is

$$\Delta p \propto u_b^2 \ . \qquad \ldots(22')$$

When laminar flow is considered, the validity of Equation 18, which becomes Equation 18', was questioned in the preceding section when compared to the experimental results of Marto and Rohsenow[36] in the limit $Re_c \to 0$ (pool boiling). When $Re_c \to 0$, Equation 18' is not valid because it implies $\Delta p \to 0$, i.e., that the drag forces are nil.

It is more meaningful to examine the validity of Equation 18' at the transition of flow regimes. This situation is possible because the approximate position of the line for the asymptotic behavior is shown in Figure 39, and therefore the uncertainty posed by the constant factor in Equation 19 is removed. If Equation 18' were valid at $Re_c = 2100$, it would predict superheat values close to the values expected by extending the asymptotic behavior slope in Figure 39 into the $Re_c = 2100$ range. This argument is valid not only because the known correlations for the friction factor give values close to that predicted by extrapolation, but also because Equations 18' and 18'' are for spherical bubbles facing a plane Couette flow (even though the expressions are for two different flow regimes). Figure 39 indicates the values for the asymptotic behavior slope (i.e., Equation 19) at $Re_c = 2100$ indicate very low superheat pressure.

$$EuRe_c^2 \simeq 1.2 \times 10^9$$

$$a \simeq 0.0085 \text{ in.}$$

$$\Delta p = \frac{2\sigma}{a} \simeq 0.15 \text{ psi} \quad .$$

This situation shows that, in the range $0 < Re_c < 2100$, the drag forces either do not play a significant role in incipient boiling or should be considered together with other forces in order to account for higher superheat values. But knowledge of the superheat pressure values in the laminar region is presently not of interest for the LMFBR.

Obviously, the degrees of freedom of a system can be reduced by imposing constraints on the system. For instance the existence of walls confining the liquid flow decreases the maximum incipient boiling superheat from the values expected for liquids in an unbounded medium. In addition to this natural constraint imposed by the container, which not only confines the medium but also transfers heat to it, there may be other constraints imposed by the experimental procedure used to determine the incipient boiling superheat. A common way to detect incipient boiling is to perform experiments at constant heat flux but variable fluid velocity. Such a procedure introduces an additional constraint to the

system, reducing its incipient boiling superheat. These values are expected to follow the trend indicated by the energy balance equation from all-liquid considerations (i.e., inversely proportional to the weight flow rate) rather than the behavior shown in Figures 39 and 43. Figures 39 and 43 clearly indicate that heat flux and velocity are not independent variables because they are linked through the incipient boiling superheat and the all-liquid considerations prevailing in the system before boiling incipience (Section III).

With respect to the maximum incipient boiling superheat curve (Figures 39 and 43), a final comment is that, on the basis of the preceding derivations, it represents cut-off values, i.e., wall superheat values which cannot be surpassed. This is in contrast to the superheat values which fall below the curve. These lower values are real and have a probabilistic character.

APPENDIX 1
EXPERIMENTAL DATA

EXPERIMENTAL DATA LEGEND*

(1) Symbols

A, B, C, J, K, L – heaters with "as-received" tubing surface finish.

DA, JA, JB, JC, JD, HA – heater surfaces prepared by sanding with 600 grit abrasive.

KA, KB, KC, KD – heater surfaces prepared by sanding first with 600 grit abrasive then with 23μ abrasive.

P (after number) runs in which boiling was initiated by reducing pressure; for all other runs boiling was initiated by increasing heat flux.

(2) Approximate only (±0.3 psi).

(3) T after pressure indicates that test section pressure was established by throttling between test section and condenser.

(4) Maximum test section pressure prior to boiling initiation tests.

(5) Sum of bulk superheat and a calculated all-liquid film temperature drop.

(6) Boiling detection device which first cut off heater power, F = Flow-meter, S = Acoustical, P = Pressure.

*For Runs B through L, data for velocities >4 ft/sec are not included in the data analyses because of strong indication of gas entrainment.

TABLE A-1
EXPERIMENTAL SODIUM BOILING INITIATION DATA

(Sheet 1 of 22)

Run (1)	Argon Cover Gas Pressure in Condenser (psia) (2)	Test Section Pressure (psia) (3)	Maximum Test Section Pressure (psia) and time (4)	Test Section Inlet Temperature (°F)	Heat Flux (Btu/hr-ft^2 10^6)	Velocity (ft/sec)	Bulk Superheat (°F)	Wall Superheat (°F) (5)	Type of Trip (6)	Heater Operating Time (min)
A38	2.0	1.96		1198	0.230	2.20	55	78		
A39	2.0	1.97		1197	0.300	2.20	33	63		
A40	2.0	1.96		1194	0.230	2.20	29	52		
A41	2.0	1.96		1193	0.304	2.20	50	80		
A42	2.0	1.96		1191	0.388	2.23	55	93		
A43	2.0	1.96		1190	0.408	2.17	63	103		
A44	2.0	1.96		1190	0.413	2.19	47	88		
A45	2.0	1.95		1162	0.413	2.96	37	78		
A46	2.0	1.96		1166	0.442	2.97	31	75		
A47	2.0	1.96		1168	0.350	3.02	40	75		
A48	2.0	1.96		1171	0.313	3.04	0	31		
A49	5.0	5.04	~14 (~24 hr.)	1351	0.238	3.04	32	57		
A50	5.0	5.05		1346	0.320	3.04	31	65		
A51	5.0	5.04		1344	0.392	3.04	17	58		
A52	5.0	5.00		1338	0.388	3.04	4	45		
A53	5.0	5.00		1342	0.392	3.02	24	65		
A54	5.0	5.01		1338	0.250	3.02	20	46		
A55	5.0	5.00		1337	0.292	3.04	60	91		
A56	5.0	5.02		1337	0.250	3.02	11	37		
A57	5.0	5.02		1336	0.270	3.02	42	70		
A58	5.0	5.02		1335	0.400	3.02	18	60		
A59	5.0	5.02		1334	0.400	3.02	7	49		
A60	5.0	5.02		1334	0.270	3.02	30	58		
A61	5.0	5.02		1336	0.321	2.94	56	90		
A62	5.0	5.02	~14 (~24 hr.)	1348	0.354	2.94	27	64		
A63	5.0	5.02		1343	0.342	2.94	27	63		
A64	5.0	5.02		1341	0.408	2.94	56	99		
A65	5.0	5.02		1336	0.396	2.96	30	72		
A66	5.0	5.02		1347	0.292	2.96	47	78		
A67	5.0	5.02		1346	0.288	2.96	20	50		

TABLE A-1
EXPERIMENTAL SODIUM BOILING INITIATION DATA

Run (1)	Argon Cover Gas Pressure in Condenser (psia) (2)	Test Section Pressure (psia) (3)	Maximum Test Section Pressure (psia) and time (4)	Test Section Inlet Temperature (°F)	Heat Flux (Btu/hr-ft^2 10^6)	Velocity (ft/sec)	Bulk Superheat (°F)	Wall Superheat (°F) (5)	Type of Trip (6)	Heater Operating Time (min)
A68	5.0	5.02		1342	0.233	2.96	23	47		
A69	5.0	5.02		1330	0.300	2.96	57	89		
A70	5.0	5.02	~ 14 (~ 24 hr.)	1339	0.288	3.25	21	51		
A71	5.0	5.01		1346	0.346	3.25	45	81		
A72	5.0	5.02		1334	0.325	3.23	33	67		
A73	5.0	5.02		1331	0.450	3.25	44	91		
A74	5.0	5.02		1330	0.450	2.62	45	92		
B1	2.0	2.11	~ 14 (~ 24 hr.)	1220	0.390	3.55	87	126		
B2	2.0	2.17		1233	0.330	3.45	75	108		
B3	2.0	2.16		1235	0.320	3.45	73	105		
B4	2.0	1.81		1238	0.350	3.45	105	140		
B5	2.0	2.14		1185	0.370	3.39	45	82		
B6	2.0	2.14		1191	0.350	3.25	44	89		
B7	2.0	2.11		1199	0.300	3.17	43	73		
B8	2.0	2.11		1198	0.300	3.07	43	73		
B9	2.0	2.08	~ 14 (~ 24hr.)	1245	0.370	3.29	103	139		
B10	2.0	2.14		1245	0.380	3.45	98	136		
B11	2.0	1.91		1245	0.370	3.35	109	145		
B12	2.0	2.14		1213	0.450	3.45	100	144		
B13	2.0	2.14		1218	0.280	3.49	-	-		
B14	2.0	2.14		1217	0.450	3.49	104	148		
B15	2.0	2.14		1217	0.400	3.51	80	120		
B16	2.0	2.14		1220	0.420	3.45	96	137		
B17	2.0	2.14		1220	0.390	3.43	86	125		
B18	2.0	2.14		1197	0.430	3.51	75	117		
B19	2.0	2.14		1195	0.420	3.41	71	112		
B20	2.0	2.14		1191	0.460	3.55	80	125		
B21	2.0	2.14		1188	0.480	3.57	86	133		
B22	5.0	5.29	~ 14 (~ 24 hr.)	1364	0.188	3.59	15	35		
B23	5.0	5.25		1364	0.192	3.64	17	37		

TABLE A-1
EXPERIMENTAL SODIUM BOILING INITIATION DATA

Run (1)	Argon Cover Gas Pressure in Condenser (psia) (2)	Test Section Pressure (psia) (3)	Maximum Test Section Pressure (psia) and time (4)	Test Section Inlet Temperature (°F)	Heat Flux (Btu/hr-ft^2 10^6)	Velocity (ft/sec)	Bulk Superheat (°F)	Wall Superheat (°F) (5)	Type of Trip (6)	Heater Operating Time (min)
B24	5.0	5.31		1360	0.167	3.55	1	19		
B25	5.0	5.31		1356	0.196	3.55	12	33		
B26	5.0	5.29		1356	0.196	3.76	7	28		
B27	5.0	5.27		1325	0.310	3.68	27	60		
B28	5.0	5.29		1322	0.290	3.70	13	44		
B29	5.0	5.21		1322	0.280	3.74	12	41		
B30	5.0	5.27		1320	0.290	3.74	12	43		
B31	5.0	5.29		1322	0.300	3.82	13	45		
B32	5.0	5.29		-	0.330	4.06	-13	22		
B33	5.0	5.25		-	0.370	3.37	15	54		
B34	5.0	5.23		-	0.390	3.45	36	77		
B35	5.0	5.23		1285	0.380	3.49	36	76		
B36	5.0	5.27		1285	0.370	3.51	19	58		
B37	5.0	5.25		1296	0.400	3.51	40	82		
B38	5.0	5.25		1295	0.330	2.88	43	78		
B39	5.0	5.25		1294	0.325	2.88	44	78		
B40	5.0	5.23		1294	0.300	2.90	24	56		
B41	5.0	5.25		1293	0.320	2.92	35	69		
B42	5.0	5.25	~14 (~ 24 hr.)	1288	0.430	4.53	6	51		
B43	5.0	5.29		1288	0.420	4.53	5	46		
B44	5.0	5.18		1284	0.430	4.53	8	53		
B45	5.0	5.20		1296	0.330	2.85	50	85		
B46	5.0	5.20		1274	0.470	4.47	8	58		
B47	5.0	5.25		1286	0.410	4.26	6	49		
B48	5.0	5.20		1289	0.400	4.22	5	47		
B49	5.0	5.19		1288	0.400	4.09	6	48		
B50	5.0	5.20		1286	0.390	4.08	3	44		
B51	5.0	5.20		1289	0.370	3.90	8	47		
B52	5.0	5.18		1289	0.480	3.86	45	95		
B53	5.0	5.20		1288	0.460	3.82	43	91		

TABLE A-1
EXPERIMENTAL SODIUM BOILING INITIATION DATA

Run (1)	Argon Cover Gas Pressure in Condenser (psia) (2)	Test Section Pressure (psia) (3)	Maximum Test Section Pressure (psia) and time (4)	Test Section Inlet Temperature (°F)	Heat Flux (Btu/hr-ft^2 10^6)	Velocity (ft/sec)	Bulk Superheat (°F)	Wall Superheat (°F) (5)	Type of Trip (6)	Heater Operating Time (min)
B54	5.0	5.19		1288	0.340	3.80	2	38		
B55	5.0	5.18		1285	0.380	3.66	18	58		
B56	5.0	5.20		1283	0.420	3.61	29	74		
B57	5.0	5.19		1285	0.380	3.64	11	51		
B58	5.0	5.19		1290	0.410	3.43	42	85		
B59	5.0	5.25		1289	0.380	3.43	27	67		
B60	5.0	5.23		1287	0.400	3.43	38	80		
B61	5.0	5.19		1287	0.370	3.21	31	70		
B62	5.0	5.18		1289	0.380	3.19	43	83		
B63	5.0	5.18		1286	0.370	3.19	32	71		
B64	5.0	3.16		1284	0.380	2.90	49	89		
B65	5.0	5.18		1283	0.370	2.92	45	84		
B66	5.0	5.16		1283	0.360	2.90	43	81		
B67	5.0	5.19		1283	0.320	2.90	17	51		
B68	5.0	5.18		1281	0.400	2.86	60	102		
B69	5.0	5.18		1286	0.360	2.70	56	94		
B70	5.0	5.19		1285	0.340	2.70	43	79		
B71	5.0	5.19		1284	0.360	2.68	55	93		
B72	5.0	5.19		1284	0.310	2.50	41	74		
B73	5.0	5.19		1284	0.340	2.50	59	95		
B74	5.0	5.19		1282	0.330	2.50	46	81		
B75	5.0	5.18		1281	0.340	2.66	55	91		
B76	5.0	5.18		1284	0.290	2.21	48	79		
B77	5.0	5.23		1287	0.310	2.17	65	98		
B78	5.0	5.25		1233	0.240	2.25	52	77		
B79	5.0	5.23		1329	0.230	2.30	41	65		
B80	5.0	5.23		1328	0.200	2.56	10	31		
B81	5.0	5.18		1329	0.260	2.52	48	75		
B82	5.0	5.18		1336	0.230	2.50	40	64		
B83	5.0	5.23		1340	0.240	2.66	42	67		

TABLE A-1
EXPERIMENTAL SODIUM BOILING INITIATION DATA

Run (1)	Argon Cover Gas Pressure in Condenser (psia) (2)	Test Section Pressure (psia) (3)	Maximum Test Section Pressure (psia) and time (4)	Test Section Inlet Temperature (°F)	Heat Flux (Btu/hr-ft^2 10^6)	Velocity (ft/sec)	Bulk Superheat (°F)	Wall Superheat (°F) (5)	Type of Trip (6)	Heater Operating Time (min)
B84	5.0	5.20		1336	0.240	2.64	44	69		
B85	5.0	5.20		1338	0.250	2.86	41	67		
B86	5.0	5.25		1338	0.240	2.82	35	60		
B87	5.0	5.25		1341	0.210	3.05	10	32		
B88	5.0	5.19		1340	0.240	3.01	36	61		
B89	5.0	5.19		1340	0.240	2.97	34	59		
B90	5.0	5.16		1341	0.220	3.27	13	36		
B91	5.0	5.14		1338	0.220	3.25	10	33		
B92	5.0	5.16		1336	0.260	3.64	7	34		
B93	5.0	5.18		1330	0.270	3.59	20	49		
B94	5.0	5.20		1331	0.310	3.51	37	70		
B95	5.0	5.20		1332	0.280	3.98	6	36		
B96	5.0	5.20		1332	0.280	3.94	12	42		
B97	5.0	5.20		1332	0.300	4.29	6	38		
B98	5.0	5.18		1333	0.300	4.29	13	45		
B99	5.0	5.20		1337	0.290	4.31	8	39		
B100	5.0	5.20		1337	0.310	4.63	10	43		
B101	2.0	2.00		1204	0.360	4.41	23	61		
B102	2.0	2.00		1202	0.310	4.41	16	49		
B103	2.0	2.00		1203	0.380	4.41	15	52		
B104	2.0	2.03		1205	0.300	4.37	15	45		
B105	2.0	2.01		1197	0.300	4.14	16	46		
B106	2.0	1.99		1196	0.310	4.14	18	49		
B107	2.0	2.00		1195	0.300	4.10	13	43		
B108	2,0	2.03		1197	0.330	4.12	20	52		
B109	2.0	2.06		1206	0.270	3.90	9	36		
B110	2.0	2.04		1206	0.280	3.90	11	39		
B111	2.0	1.98		1208	0.260	3.90	15	41		
B112	2.0	2.04		1205	0.270	3.71	11	38		
B113	2.0	1.98		1196	0.240	3.69	1	25		

TABLE A-1
EXPERIMENTAL SODIUM BOILING INITIATION DATA

Run (1)	Argon Cover Gas Pressure in Condenser (psia) (2)	Test Section Pressure (psia) (3)	Maximum Test Section Pressure (psia) and time (4)	Test Section Inlet Temperature (°F)	Heat Flux (Btu/hr-ft^2 10^6)	Velocity (ft/sec)	Bulk Superheat (°F)	Wall Superheat (°F) (5)	Type of Trip (6)	Heater Operating Time (min)
B114	2.0	1.98		1194	0.300	3.69	22	52		
B115	2.0	1.98		1197	0.300	3.71	27	57		
B116	2.0	2.01		1201	0.280	3.52	24	52		
B117	2.0	2.05		1201	0.260	3.52	13	39		
B118	2.0	2.05		1202	0.270	3.53	14	41		
B119	2.0	1.99		1204	0.260	3.53	16	42		
B120	2.0	1.99		1197	0.250	3.36	17	42		
B121	2.0	2.04		1199	0.270	3.38	21	48		
B122	2.0	2.03		1195	0.240	3.38	9	33		
B123	2.0	2.04		1197	0.260	3.19	22	48		
B124	2.0	2.03		1194	0.240	3.17	13	37		
B125	2.0	2.01		1193	0.240	3.17	16	40		
B126	2.0	2.03		1197	0.240	2.95	21	45		
B127	2.0	2.04		1200	0.230	2.95	17	40		
B128	2.0	2.03		1199	0.230	2.95	16	39		
B129	2.0	2.01		1201	0.190	2.72	12	27		
B130	2.0	2.01		1201	0.210	2.72	20	41		
B131	2.0	2.00		1197	0.210	2.76	19	40		
B132	2.0	2.04		1194	0.230	2.76	18	41		
B133	2.0	2.01		1194	0.196	2.53	13	32		
B134	2.0	2.01		1193	0.210	2.53	20	41		
B135	2.0	2.03		1193	0.210	2.51	17	38		
B136	2.0	2.01		1197	0.190	2.32	16	35		
B137	2.0	2.04		1203	0.180	2.30	14	32		
B138	2.0	2.00		1202	0.180	2.30	30	48		
B139	2.0	2.01		1193	0.170	2.28	16	33		
B140	2.0	2.04		1197	0.188	2.00	23	42		
B141	2.0	2.03		1202	0.167	2.00	25	41		
B142	2.0	2.03		1202	0.167	1.98	22	38		
B143	2.0	2.00		1191	0.160	4.22	13	29		

TABLE A-1
EXPERIMENTAL SODIUM BOILING INITIATION DATA

Run (1)	Argon Cover Gas Pressure in Condenser (psia) (2)	Test Section Pressure (psia) (3)	Maximum Test Section Pressure (psia) and time (4)	Test Section Inlet Temperature (°F)	Heat Flux (Btu/hr-ft^2 10^6)	Velocity (ft/sec)	Bulk Superheat (°F)	Wall Superheat (°F) (5)	Type of Trip (6)	Heater Operating Time (min)
B144	2.0	2.01		1198	0.325	4.20	-2	30		
B145	2.0	2.04		1199	0.250	4.20	-12	13		
B146	5.0	5.00		1282	0.370	3.29	28	67		
B147	5.0	5.06		1290	0.350	3.29	35	72		
B148	5.0	5.02		1286	0.360	3.25	39	77		
B149	5.0	5.04		1286	0.330	3.27	22	57		
B150	5.0	5.00		1283	0.360	3.23	18	56		
B151	5.0	5.04		1290	0.320	3.29	6	40		
B152	5.0	5.05		1292	0.330	3.05	24	59		
B153	5.0	5.04		1291	0.340	3.05	28	64		
B154	5.0	5.05		1288	0.280	3.05	-4	26		
B155	5.0	5.05		1283	0.350	3.05	25	62		
B156	5.0	5.05		1282	0.330	2.74	28	63		
B157	5.0	5.00		1285	0.300	2.70	22	54		
B158	5.0	5.00		1283	0.310	2.66	24	57		
B159	5.0	5.03		1281	0.320	2.66	27	61		
B160	5.0	5.04		1282	0.300	2.46	30	62		
B161	5.0	5.06		1286	0.290	2.46	27	58		
B162	5.0	4.97		1288	0.280	2.44	24	54		
B163	5.0	4.96		1290	0.250	2.21	29	55		
B164	5.0	4.98		1296	0.240	2.17	29	54		
B165	5.0	4.99		1296	0.230	2.15	27	51		
B166	5.0	5.02		1292	0.250	2.09	32	58		
B167	5.0	5.00		1286	0.230	1.97	31	55		
B168	5.0	5.02		1286	0.240	1.93	34	59		
B169	5.0	5.03		1286	0.230	1.91	31	55		
B170	5.0	5.06		1286	0.230	1.89	32	56		
C1	5.0	5.01		1331	0.280	4.43	10	40		
C2	5.0	4.97		1334	0.270	3.45	30	58		
C3	5.0	5.02		1338	0.250	3.45	24	50		

TABLE A-1
EXPERIMENTAL SODIUM BOILING INITIATION DATA

Run (1)	Argon Cover Gas Pressure in Condenser (psia) (2)	Test Section Pressure (psia) (3)	Maximum Test Section Pressure (psia) and time (4)	Test Section Inlet Temperature (°F)	Heat Flux (Btu/hr-ft^2 10^6)	Velocity (ft/sec)	Bulk Superheat (°F)	Wall Superheat (°F) (5)	Type of Trip (6)	Heater Operating Time (min)
C4	5.0	5.01		1340	0.260	3.43	30	57		
C5P		5.37		1336	0.250	3.47	14	40		
C6P		5.33		1334	0.260	3.41	19	46		
C7	5.0	5.01		1338	0.230	3.45	18	42		
C8P		7.33		1333	0.340	3.45	13	50		
C9P		7.29		1334	0.360	3.45	12	51		
C10P		7.51		1335	0.330	3.49	15	51		
C11P		8.64		1336	0.400	3.45	10	54		
C12P		9.58		1339	0.430	3.49	-1	47		
C13P		10.00		1334	0.420	3.51	-22	25		
C14P		6.47		1336	0.330	4.63	-21	14		
C15	5.0	6.16		1326	0.330	4.33	-12	23		
C16	5.0	2.03		1197	0.190	3.45	-21	-2		
C17	5.0	2.09		1197	0.190	3.47	-23	-4		
C18	5.0	2.09		1198	0.190	3.45	-22	-3		
C19	5.0	5.00		1332	0.190	3.45	-15	5		
C20	5.0	5.01		1332	0.220	3.47	0	23		
C21	5.0	5.08		1336	0.210	3.47	-7	15		
C22	5.0	5.00		1337	0.180	3.49	-19	0		
C23	5.0	8.00		1418	0.210	3.49	-1	22		
C24	5.0	7.97		1418	0.170	3.51	-17	2		
C25	5.0	8.00		1419	0.170	3.51	-18	1		
C26	5.0	8.00		1413	0.170	3.51	-16	3		
C27	5.0	10.03		1453	0.200	3.45	6	16		
C28	5.0	10.03		1450	0.190	3.53	-16	5		
C29	5.0	10.03		1450	0.200	3.53	-13	9		
C30	5.0	12.00		1481	0.190	3.43	-13	9		
C31	5.0	12.00		1483	0.250	3.39	14	42		
C32	5.0	12.00		1483	0.230	3.39	6	32		
C33	5.0	12.00		1483	0.200	3.39	-7	16		

TABLE A-1
EXPERIMENTAL SODIUM BOILING INITIATION DATA

Run (1)	Argon Cover Gas Pressure in Condenser (psia) (2)	Test Section Pressure (psia) (3)	Maximum Test Section Pressure (psia) & time (min) (4)	Test Section Inlet Temperature (°F)	Heat Flux (Btu/hr-ft^2 10^6)	Velocity (ft/sec)	Bulk Superheat (°F)	Wall Superheat (°F) (5)	Type of Trip (6)	Heater Operating Time (min)
C34	5.0	12.00		1485	0.220	3.45	-8	17		
CA1	5.0	5.01		1287	0.242	2.94	11	36		
CA2	5.0	5.03		1287	0.271	2.98	20	49		
CA3	5.0	5.07		1284	0.279	2.96	28	57		
CA4	5.0	5.01	25 (1)	1285	0.242	2.94	10	36		
CA5	5.0	5.03	25.1 (15)	1283	0.271	2.88	31	60		
CA6	5.0	5.03		1283	0.333	2.88	60	95		
CA7	5.0	5.05		1281	0.346	2.94	58	94		
CA8	5.0	5.05		1283	0.271	2.92	25	54		
CA9	5.0	5.01		1284	0.365	2.98	57	96	S	
CA10	5.0	5.01		1285	0.263	3.03	-1	27	S	
CA11	5.0	5.05		1289	0.367	3.09	58	97	F	
CA12	5.0	5.01	25.1 (60)	1285	0.263	2.90	2	30	S	
CA13	5.0	4.98	25.1 (15)	1284	0.221	2.98	-23	0	F	
CA14	5.0	5.01	15 (15)	1283	0.333	2.98	34	69	S	
CA15	5.0	5.01		1281	0.275	3.03	1	30	S	
CA16	5.0	5.04		1284	0.333	2.98	37	72	FS	
CA17	5.0	5.06		1285	0.275	2.98	5	34	S	
J1	5.0	5.04		1272	0.296	2.94	-4	27	S	
J2	5.0	5.00		1281	0.320	2.94	17	51	F	
J3	5.0	5.03		1277	0 342	2.94	18	54	F	
J4	5.0	5.05		1285	0.349	3.00	29	66	F	
J5	5.0	5.15		1285	0.333	2.98	20	55	F	
J6	5.0	5.13	25.5 (1)	1292	0.350	2.98	38	75	F	
J7	5.0	5.14	25.5 (1)	1286	0.329	2.88	26	61	F	
J8	5.0	5.19	26.0 (5)	1282	0.329	3.00	8	43	F	
J9	5.0	5.17		1279	0.329	2.94	7	42	F	
J10	5.0	5.10		1281	0.308	2.92	-3	30	F	
J11	5.0	5.02		1279	0.283	2.90	-5	25	S	50.5
J12	5.0	5.03		1280	0.329	2.98	9	44	F	

TABLE A-1
EXPERIMENTAL SODIUM BOILING INITIATION DATA

Run (1)	Argon Cover Gas Pressure in Condenser (psia) (2)	Test Section Pressure (psia) (3)	Maximum Test Section Pressure (psia) & time (min) (4)	Test Section Inlet Temperature (°F)	Heat Flux (Btu/hr-ft^2 10^6)	Velocity (ft/sec)	Bulk Superheat (°F)	Wall Superheat (°F) (5)	Type of Trip (6)	Heater Operating Time (min)
J13	5.0	5.06		1282	0.342	2.94	2	38	F	
J14	5.0	5.01	25.5 (5)	1282	0.313	2.96	4	37	S	
J15	5.0	5.04	25.5 (5)	1278	0.325	3.00	2	36	F	
J16	5.0	5.07	25.5 (10)	1275	0.338	3.07	8	44	F	
J17	5.0	5.12	25.5 (10)	1279	0.342	3.17	5	41	F	
J18	5.0	5.03		1279	0.346	2.98	3	40	FP	
J19	5.0	5.00		1281	0.325	2.96	6	40	FP	
J20	5.0	5.03		1283	0.350	2.98	14	51	F	
J21	5.0	5.07		1283	0.333	3.00	10	45	F	
J22	5.0	5.10		1284	0.333	3.00	9	44	F	87.1
J23	1.9	1.98		1133	0.358	2.98	22	57	F	
J24	1.9	1.95		1136	0.346	2.98	18	52	F	
J25	2.0	2.00		1136	0.379	2.98	28	65	F	
J26	1.9	1.99	25.5 (5)	1136	0.392	2.98	41	80	F	
J27	2.0	2.01	25.5 (10)	1133	0.479	2.96	82	129	FP	
J28	1.9	1.98	25.5 (10)	1135	0.363	3.00	22	58	F	
J29	2.0	2.10	25.5 (10)	1134	0.392	3.00	14	53	F	
J30	1.9	1.99	25.5 (10)	1137	0.342	3.00	14	48	F	
J31	2.0	2.00		1134	0.383	3.00	33	71	F	
J32	2.0	2.04		1137	0.454	3.02	60	105	FP	
J33	2.0	2.04		1131	0.433	3.22	40	83	FP	
J34	2.0	2.00		1142	0.354	3.00	11	46	FP	
J35	2.0	2.04		1135	0.396	2.94	36	75	F	138
J36	2.0	5.54T		1294	0.264	2.92	-10	18	F	
J37	2.0	5.09T		1290	0.274	2.94	7	36	F	
J38	2.0	4.97T		1295	0.271	2.90	-2	27	F	
J39	2.0	5.00T		1292	0.276	2.98	9	38	F	
J40	2.0		25.1 (5)							
J41	2.0		25.0 (1/2)							
J42	2.0	5.51T	17.3 (5)	1292	0.229	3.02	43	67	F	

TABLE A-1
EXPERIMENTAL SODIUM BOILING INITIATION DATA

Run (1)	Argon Cover Gas Pressure in Condenser (psia) (2)	Test Section Pressure (psia) (3)	Maximum Test Section Pressure (psia) & time (min) (4)	Test Section Inlet Temperature (°F)	Heat Flux (Btu/hr-ft^2 10^6)	Velocity (ft/sec)	Bulk Superheat (°F)	Wall Superheat (°F) (5)	Type of Trip (6)	Heater Operating Time (min)
J43	2.0	5.20T		1294	0.263	2.98	8	36	F	
J44	2.0									
J45	2.0	5.03T	(1/12)	1293	0.244	2.98	-3	23	F	
J46	2.0	3.80		1290	0.191	3.00	4	24	F	
J47	2.0	4.95T		1287	0.256	3.00	-3	24	F	192
J48	2.0	5.09T		1290	0.356	4.15	-7	31	S	
J49	2.0	5.03T		1291	0.353	4.15	-6	31	S	
J50	2.0		30.0 (1/12)							
J51	2.0	5.03T	25.5 (5)	1284	0.276	4.24	-22	7	S	
JA1	2.0	4.97T		1287	0.321	4.15	-20	14	S	
JA2	2.0	4.93T		1287	0.306	4.11	-25	7	S	
JA3	2.0	5.02T		1287	0.376	4.30	-9	31	FS	
JA4	2.0	4.80T		1287	0.321	4.28	-21	13	FS	
JA5	2.0	5.00T		1289	0.338	4.37	-16	20	S	
JA6	2.0	5.08T	15.0 (5)	1288	0.396	4.32	-3	39	F	
JA7	2.0	5.00T	15.0 (5)	1286	0.425	4.32	7	52	F	
JA8	2.0	5.00T	15.0 (5)	1277	0.463	4.28	9	54	F	
JA9	2.0	5.05T		1282	0.440	4.30	-6	40	F	
JA10	2.0	4.97T		1281	0.440	4.30	-5	41	FS	30
JA11	2.0	7.65T		1336	0.504	4.20	35	90	F	
JA12	2.0	8.10T		1329	0.558	4.24	44	105	F	
JA13	2.0	8.05T		1328	0.525	4.24	28	86	F	
JA14	2.0	8.05T		1334	0.521	4.26	36	93	F	
JA15	2.0	8.01T		1344	0.517	4.26	37	94	F	
JA16	2.0	8.00T		1341	0.423	4.28	-5	41	S	
JA17	2.0	8.10T		1335	0.517	4.28	26	31	F	
JA18	2.0	8.12T		1334	0.442	4.28	-7	42	S	46
JB1	5.0	7.91T		1399		3.26			F	
JB2	5.0	7.95T		1404	0.266	3.30	19	48	F	
JB3	5.0	7.93T		1405	0.236	3.28	5	31	F	

TABLE A-1
EXPERIMENTAL SODIUM BOILING INITIATION DATA

Run (1)	Argon Cover Gas Pressure in Condenser (psia) (2)	Test Section Pressure (psia) (3)	Maximum Test Section Pressure (psia) & time (min) (4)	Test Section Inlet Temperature (°F)	Heat Flux (Btu/hr-ft^2 10^6)	Velocity (ft/sec)	Bulk Superheat (°F)	Wall Superheat (°F) (5)	Type of Trip (6)	Heater Operating Time (min)
JB4	5.0	7.88T		1404	0.288	3.30	26	58	F	
JB5	5.0	7.97T		1400	0.291	3.30	25	57	F	
JB6	5.0	7.98T		1399	0.256	3.32	-3	25	F	
JB7	5.0	8.00T		1399	0.255	3.30	6	34	F	10.1
JB8	5.0	7.99T		1408	0.317	3.20	41	76	FS	
JB9	5.0	7.92T		1404	0.297	3.22	26	59	F	
JB10	5.0	8.10T		1400	0.346	3.20	41	79	F	
JB11	5.0	7.95T		1398	0.327	3.22	31	67	FS	
JB12	5.0	7.80T	15.0 (5.0)	1403	0.354	3.17	35	74	F	
JB13	5.0	8.04T		1397	0.304	3.15	20	53	F	
JB14	5.0	7.90T		1397	0.319	3.20	24	59	F	
JB15	5.0	7.93T	15.0 (5.0)	1408	0.310	3.13	42	76	FS	
JB16	5.0	8.01T		1404	0.340	3.20	41	78	FS	
JB17	5.0	7.88T		1402	0.303	3.13	29	62	F	
JB18	5.0	7.92T	15.0 (5.0)	1412	0.235	3.20	3	28	F	
JB19	5.0	7.96T		1409	0.264	3.11	14	42	F	
JB20	5.0	8.14T		1406	0.333	3.11	41	77	FS	
JB21	5.0	7.82T		1404	0.324	3.24	37	72	FP	
JB22	5.0	8.11T		1404	0.344	3.20	44	81	FS	
JB23	5.0	8.15T		1404	0.339	3.13	36	72	FS	
JB24	5.0	8.15T		1404	0.341	3.13	40	76	FS	
JB25	5.0	7.89T		1403	0.325	3.24	37	72	FS	
JB26	5.0	8.19T		1398	0.360	3.26	39	78	FS	
JB27	5.0	8.04T		1399	0.326	3.15	31	66	FS	
JB28	5.0	7.88T	15.0 (5.0)	1410	0.328	3.26	44	79	FS	
JB29	5.0	8.11T		1407	0.342	3.13	41	78	FS	
JB30	5.0	8.05T		1403	0.353	3.13	40	78	FS	
JB31	5.0	7.84T		1402	0.347	3.26	46	83	FS	42.1
JC1	5.0	7.78T		1337	0.393	3.22	3	45	FS	
JC2	5.0	8.00T		1333	0.460	3.17	26	75	F	

TABLE A-1
EXPERIMENTAL SODIUM BOILING INITIATION DATA

Run (1)	Argon Cover Gas Pressure in Condenser (psia) (2)	Test Section Pressure (psia) (3)	Maximum Test Section Pressure (psia) & time (min) (4)	Test Section Inlet Temperature (°F)	Heat Flux (Btu/hr-ft^2 10^6)	Velocity (ft/sec)	Bulk Superheat (°F)	Wall Superheat (°F) (5)	Type of Trip (6)	Heater Operating Time (min)
JC3	5.0	7.83T		1324	0.441	3.15	17	64	F	
JC4	5.0	7.97T		1320	0.431	3.15	12	58	F	
JC5	5.0	8.10T		1317	0.469	3.17	30	80	F	
JC6[1]	5.0	7.81T	15.0 (5.0)	1318	0.393	3.15	-3	39	S	
JC7	5.0	7.86T		1313	0.385	3.17	-14	27	S	
JC8	5.0	7.93T		1310	0.502	3.15	43	97	F	
JC9	5.0	7.92T		1308	0.511	3.13	44	99	F	
JC10	5.0	7.91T	15.0 (5.0)	1313	0.503	3.11	48	102	F	
JC11	5.0	8.00T		1308	0.539	3.17	60	118	FS	
JC12	5.0	7.83T		1304	0.520	3.20	49	105	FS	
JC13	5.0	7.92T		1304	0.518	3.20	40	96	FS	25.3
JC14	5.0	7.98T	10.0 (18 hrs)	1217	0.758	3.20	95	176	S	
JC15	5.0	7.74T		1214	0.588	3.20	0	63	S	
JC16	5.0	8.11T		1216	0.661	3.15	34	105	FS	
JC17	5.0	7.98T		1218	0.552	3.11	-30	29	S	
JC18	5.0	7.61T		1223	0.676	3.11	57	130	F	
JC19	5.0	7.76T		1223	0.627	3.20	12	79	FS	
JC20	5.0	7.40T	15.0 (5.0)	1216	0.740	3.20	66	147	FS	
JC21	5.0	6.39T		1210	0.688	3.20	72	147	F	
JC22	5.0	8.47T		1209	0.763	3.22	68	153	FS	
JC23	5.0	7.72T		1211	0.593	3.15	-18	49	S	
JC24	5.0	6.45T	15.0 (5.0)	1212	0.505	3.26	-33	22	S	
JC25	5.0	7.93T		1207	0.680	3.22	11	86	FS	
JC26	5.0	7.86T		1204	0.629	3.22	-14	55	S	
JC27	5.0	7.80T		1207	0.654	3.24	-2	70	S	
JC28	5.0	7.95T	15.0 (5.0)	1212	0.790	3.24	90	177	FS	
JC29	5.0	7.95T		1208	0.739	3.13	56	137	F	
JC30	5.0	7.92T		1209	0.711	3.20	38	116	F	
JC31	5.0	7.89T		1212	0.731	3.22	53	134	F	70.2
JD1	5.0	5.45		1137	0.813	3.20	8	95	S	

TABLE A-1
EXPERIMENTAL SODIUM BOILING INITIATION DATA

Run (1)	Argon Cover Gas Pressure in Condenser (psia) (2)	Test Section Pressure (psia) (3)	Maximum Test Section Pressure (psia) & time (min) (4)	Test Section Inlet Temperature (°F)	Heat Flux (Btu/hr-ft^2 10^6)	Velocity (ft/sec)	Bulk Superheat (°F)	Wall Superheat (°F) (5)	Type of Trip (6)	Heater Operating Time (min)
JD2	5.0	5.09		1138	0.792	3.20	59	143	FS	
JD3	5.0	5.08		1148	0.727	3.24	30	107	F	
JD4	4.9	4.98		1149	0.588	3.20	-24	38	S	
JD5	5.0	5.13	15.0 (5.0)	1158	0.716	3.20	36	112	F	
JD6	5.0	5.05		1148	0.807	3.17	78	164	F	
JD7	5.0	5.26		1146	0.716	3.17	21	97	F	
JD8	4.9	4.95		1147	0.705	3.15	24	99	F	
JD9	4.8	4.86	15.0 (5.0)	1140	0.752	3.20	37	117	F	30
JD10	5.0	5.10		1229	0.520	3.17	2	57	FS	
JD11	5.0	5.03		1229	0.438	3.17	-9	37	S	
JD12	5.0	5.12		1232	0.551	3.20	27	85	P	
JD13	5.0	5.19		1294	0.381	3.15	15	55	F	
JD14	5.0	5.15		1291	0.388	3.17	18	59	F	
JD15	5.0	5.06	15.0 (5.0)	1291	0.378	3.20	19	59	F	
JD16	5.0	5.06		1285	0.394	3.15	20	62	F	
JD17	5.0	5.10		1287	0.359	3.22	2	40	F	
K1P	5.0	11.34T	15.0 (3.0)	1308	0.485	3.00	15	70	F	
K2P	5.0	9.63T	12.0 (3.0)	1305	0.496	3.28	20	76	F	
K3P	5.0	8.07T	12.0 (3.0)	1302	0.537	3.39	62	121	F	
K4P	5.0	8.35T	10.0 (3.0)	1300	0.496	3.39	50	105	F	
K5P	5.0	9.65T	10.0 (3.0)	1302	0.538	3.20	36	97	F	
K6P	5.0	9.45T	10.0 (3.0)	1308	0.538	3.17	44	105	FS	
K7P	5.0	10.00T	11.0 (3.0)	1312	0.539	3.17	21	82	F	
K8P	5.0	9.75T	11.0 (3.0)	1315	0.542	3.20	36	97	FS	
K9P	5.0	9.70T	11.0 (3.0)	1311	0.538	3.20	36	96	F	
K10P	5.0	9.70T	10.0	1306	0.536	3.22	33	93	F	
K11P	5.0	8.40T	10.0	1305	0.541	3.20	56	116	FS	
K12P	5.0	9.62T	10.0	1302	0.536	3.17	29	89	F	
K13P	5.0	9.30T	10.0	1300	0.548	3.20	40	101	F	
K14P	5.0	8.28T	10.0	1302	0.538	3.24	33	92	F	

TABLE A-1
EXPERIMENTAL SODIUM BOILING INITIATION DATA

Run (1)	Argon Cover Gas Pressure in Condenser (psia) (2)	Test Section Pressure (psia) (3)	Maximum Test Section Pressure (psia) & time (min) (4)	Test Section Inlet Temperature (°F)	Heat Flux (Btu/hr-ft^2 10^6)	Velocity (ft/sec)	Bulk Superheat (°F)	Wall Superheat (°F) (5)	Type of Trip (6)	Heater Operating Time (min)
K15P	5.0	8.29T	10.0	1302	0.536	3.22	31	90	F	
K16P	5.0	7.05T	10.0	1304	0.536	3.30	79	133	F	
K17P	5.0	8.79T	10.0	1304	0.540	3.26	44	104	FS	39.7
K18P	5.0	10.73T	11.0	1215	0.719	3.24	25	107	F	
K19P	5.0	9.00T	11.0	1213	0.712	3.34	39	119	F	
K20P	5.0	8.78T	12.0	1214	0.721	3.26	47	128	FS	
K21P	5.0	7.91T	13.0	1219	0.728	3.34	75	156	F	
K22P	5.0	8.70T	12.0	1221	0.730	3.28	59	141	FS	
K23P	5.0	7.88T	12.0	1225	0.731	3.34	76	157	FS	
K24P	5.0	7.70T	12.0	1226	0.731	3.37	80	161	F	
K25P	5.0	9.12T	12.0	1225	0.741	3.30	56	139	F	
K26P	5.0	8.22T	11.0	1219	0.745	3.30	74	157	FS	
K27P	5.0	10.06T	12.0	1217	0.738	3.26	-2	81	FS	
K28P	5.0	9.70T	13.0	1218	0.759	3.30	45	130	F	
K29P	5.0	10.18T	12.0	1216	0.683	3.26	-27	50	S	
K30P	5.0	11.27T	12.0	1216	0.743	3.28	-12	73	S	
K31P	5.0	10.46T	12.0	1216	0.719	3.24	-7	75	S	
K32P	5.0	12.45T	12.0	1216	0.766	3.15	-9	79	S	63.7
K33P	5.0	11.19T	12.0(12 days)	1214	0.729	3.11	31	114	F	
K34P	5.0	10.35T	16.0 (3.0)	1213	0.737	3.28	26	110	F	
K35P	5.0	9.54T	12.0	1215	0.737	3.29	54	137	F	
K36P	5.0	9.89T	12.0	1218	0.740	3.30	48	131	F	
K37P	5.0	9.30T	12.0	1222	0.739	3.24	73	156	F	
K38P	5.0	6.84T	11.0	1230	0.538	3.28	22	71	F	
K39P	5.0	6.69T	10.0	1225	0.541	3.37	25	84	F	
K40P	5.0	5.85T	10.0	1227	0.550	3.30	44	103	F	
K41P	5.0	6.41T	8.0	1226	0.547	3.37	34	93	F	
K42P	5.0	6.56T	8.0	1219	0.546	3.37	21	81	F	85
L1P	5.0	10.71T	12.0 (3.0)	1157	0.429	3.07	-21	28	F	
L2	7.9	7.93		1168	0.398	3.26	21	64	F	

TABLE A-1
EXPERIMENTAL SODIUM BOILING INITIATION DATA

Run (1)	Argon Cover Gas Pressure in Condenser (psia) (2)	Test Section Pressure (psia) (3)	Maximum Test Section Pressure (psia) & time (min) (4)	Test Section Inlet Temperature (°F)	Heat Flux (Btu/hr-ft^2 10^6)	Velocity (ft/sec)	Bulk Superheat (°F)	Wall Superheat (°F) (5)	Type of Trip (6)	Heater Operating Time (min)
L3	7.9	7.94		1162	0.402	3.24	10	53	F	
L4	8.0	8.04		1162	0.402	3.24	3	46	F	
L5	7.9	7.99		1163	0.424	3.26	47	92	F	
L6	8.0	8.00		1168	0.393	3.24	29	71	F	
L7	8.0	8.00		1165	0.382	3.26	-4	37	F	
L8	8.0	8.00		1164	0.363	3.22	-6	33	F	
L9	7.7	7.79		1162	0.408	3.22	25	69	F	
L10	8.0	8.04		1163	0.412	3.20	30	74	F	35.6
KA1	8.0	14.96T	~15.0(~24 hrs)	1422	0.563	3.20	56	122	F S	
KA2	8.0	14.85T		1424	0.521	3.22	44	105	F S	
KA3	8.0	15.00T		1430	0.563	3.26	73	139	F S	15.1
KA4	8.0	14.69T	~15.0(~24 hrs)	1424	0.586	3.20	125	194	F S P	
KA5	8.0	14.80T		1427	0.533	3.20	88	150	F	
KA6	8.0	14.79T		1425	0.461	3.18	34	88	S	
KA7	8.0	14.38T		1427	0.476	3.20	26	92	F S	
KA8	8.0	14.90T		1428	0.400	3.22	-1	46	S	
KA9	8.0	14.75T		1429	0.413	3.22	-3	45	S	
KA10	8.0	15.07T		1427	0.464	3.24	15	69	S	
KA11	8.0	14.61T		1429	0.531	3.24	86	148	F	
KA12	8.0	14.67T		1427	0.489	3.24	56	113	F	
KA13	8.0	14.75T		1428	0.471	3.24	40	95	F	
KA14	8.0	14.93T		1428	0.452	3.24	17	70	F S	
KA15	8.0	15.07T		1430	0.510	3.24	56	116	F	
KA16	8.0	14.88T		1430	0.432	3.24	17	68	S	
KA17	8.0	15.26T		1430	0.486	3.24	46	103	F S	
KA18	8.0	14.62T		1430	0.484	3.26	51	108	F S	
KA19	8.0	14.91T		1431	0.461	3.22	40	94	F S	
KA20	8.0	15.12T		1431	0.492	3.26	46	104	F	29.8
KA21	5.0	5.02	15.0(60)	1131	0.651	3.28	38	107	S	
KA22	4.9	4.95		1130	0.600	3.24	-20	44	S	

TABLE A-1
EXPERIMENTAL SODIUM BOILING INITIATION DATA

Run (1)	Argon Cover Gas Pressure in Condenser (psia) (2)	Test Section Pressure (psia) (3)	Maximum Test Section Pressure (psia) & time (min) (4)	Test Section Inlet Temperature (°F)	Heat Flux (Btu/hr-ft^2 10^6)	Velocity (ft/sec)	Bulk Superheat (°F)	Wall Superheat (°F) (5)	Type of Trip (6)	Heater Operating Time (min)
KA23	4.9	4.95		1131	0.599	3.22	-21	43	S	
KA24	4.9	4.92		1134	0.698	3.26	42	116	F	
KA25	4.9	4.94		1135	0.733	3.24	59	137	F	
KA26	4.9	4.92		1138	0.730	3.24	68	144	F	
KA27	4.9	4.98		1139	0.746	3.24	53	132	F	
KA28	5.0	5.00		1137	0.575	3.28	-26	35	S	
KA29	5.0	5.03		1137	0.734	3.24	57	135	F S	
KA30	5.0	5.00		1137	0.634	3.26	-3	64	S	
KA31	5.0	5.03		1135	0.825	3.26	98	185	F S	
KA32	5.0	5.00		1132	0.577	3.30	-54	7	S	
KA33	5.0	5.06		1132	0.736	3.26	31	109	F S	
KA34	5.0	5.02		1129	0.661	3.26	-1	69	F S	
KA35	5.0	5.04		1129	0.599	3.26	-53	10	S	52
KB1	4.9	4.98	15.0 (60)	1238	0.399	3.17	-9	33	S	
KB2	5.0	5.00		1237	0.470	3.26	17	67	F S	
KB3	5.0	5.01		1237	0.460	3.26	13	62	F	
KB4	5.0	5.02		1239	0.536	3.15	60	117	F S	
KB5	5.0	5.02		1240	0.453	3.11	10	58	S	
KB6	5.0	5.01		1241	0.533	3.22	54	110	F	
KB7	5.0	5.02		1239	0.590	3.24	84	146	F S	
KB8	5.0	5.01		1238	0.470	3.26	24	74	S	
KB9	5.0	5.03		1238	0.500	3.22	35	88	F S	
KB10	5.0	5.02		1237	0.435	3.22	-2	44	S	
KB11	5.0	5.02		1238	0.543	3.20	58	115	F S	
KB12	5.0	5.03		1239	0.600	3.28	96	160	F	
KB13	5.0	5.03		1239	0.596	3.15	85	148	F S	
KB14	5.0	5.04		1238	0.759	3.26	161	241	F S	
KB15	5.0	5.01		1237	0.536	3.28	55	112	F	
KB16	5.0	5.12		1237	0.547	3.26	63	121	F	
KB17	5.0	5.06		1237	0.627	3.20	95	161	F S	

TABLE A-1
EXPERIMENTAL SODIUM BOILING INITIATION DATA

Run (1)	Argon Cover Gas Pressure in Condenser (psia) (2)	Test Section Pressure (psia) (3)	Maximum Test Section Pressure (psia) & time (min) (4)	Test Section Inlet Temperature (°F)	Heat Flux (Btu/hr-ft^2 10^6)	Velocity (ft/sec)	Bulk Superheat (°F)	Wall Superheat (°F) (5)	Type of Trip (6)	Heater Operating Time (min)
KB18	5.0	5.02		1238	0.557	3.26	73	132	F S	
KB19	5.0	5.02		1238	0.410	3.26	-1	42	S	
KB20	5.0	5.03		1239	0.539	3.26	62	119	F S	23.8
KB21	5.0	5.01	18.0 (60)	1333	0.287	3.20	18	48	F	
KB22	5.0	5.19		1334	0.350	3.20	1	38	S	
KB23	4.9	4.93		1335	0.240	3.17	3	28	S	
KB24	5.0	5.40		1333	0.358	3.20	-1	37	S	
KB25	4.9	4.98		1334	0.306	3.17	50	82	F S	
KB26	4.9	4.98		1332	0.490	3.22	146	198	F S	
KB27	5.0	5.02		1333	0.266	3.24	21	49	S	
KB28	5.0	5.00		1334	0.238	3.22	7	32	S	
KB29	5.0	5.01		1335	0.282	3.24	29	59	F S	
KB30	5.0	5.04		1335	0.389	3.26	95	136	F S	
KB31	5.0	5.03		1337	0.490	3.24	129	181	F S	
KB32	5.0	5.04		1337	0.349	3.22	66	103	F S	
KB33	5.0	5.03		1336	0.410	3.26	105	148	F	
KB34	5.0	5.04		1336	0.588	3.32	143	205	F S	
KB35	5.0	5.07		1334	0.365	3.20	77	116	F S	
KB36	4.9	4.95		1333	0.327	3.22	59	94	F S	
KB37	4.9	4.96		1333	0.393	3.22	100	142	F S	
KB38	4.9	4.96		1331	0.262	3.26	11	39	S	
KB39	4.9	4.97		1332	0.279	3.20	28	57	S	
KB40	5.0	5.00		1330	0.252	3.22	13	40	S	37.2
KC 1	5.0	5.10	~15.0 (~24 hrs)	1408	0.132	3.17	18	32	S	
KC 2	5.0	5.01		1406	0.090	3.26	-2	7	F S	
KC 3	5.0	5.01		1405	0.140	3.26	24	39	F	
KC 4	5.0	5.00		1404	0.139	3.26	13	28	F	
KC 5	4.9	4.97		1405	0.191	3.24	43	63	F	
KC 6	5.0	5.01		1404	0.235	3.26	60	85	F	
KC 7	5.0	5.10		1406	0.203	3.28	50	71	F	

TABLE A-1
EXPERIMENTAL SODIUM BOILING INITIATION DATA

Run (1)	Argon Cover Gas Pressure in Condenser (psia) (2)	Test Section Pressure (psia) (3)	Maximum Test Section Pressure (psia) and time (4)	Test Section Inlet Temperature (°F)	Heat Flux (Btu/hr-ft^2 10^6)	Velocity (ft/sec)	Bulk Superheat (°F)	Wall Superheat (°F) (5)	Type of Trip (6)	Heater Operating Time (min)
KC8	5.0	5.03		1406	0.173	3.22	45	63	F	
KC9	5.0	5.00		1407	0.183	3.26	42	61	F	
KC10	5.0	5.03		1408	0.093	3.26	-2	8	F	
KC11	5.0	5.05		1408	0.183	3.28	39	58	F	
KC12	5.0	5.01		1408	0.219	3.30	66	89	F	
KC13	5.0	5.10		1407	0.249	3.22	65	91	F	
KC14	5.0	5.03		1406	0.176	3.22	40	59	F	
KC15	5.0	5.03		1405	0.154	3.26	36	52	F	
KC16	5.0	5.00		1406	0.169	3.26	42	60	F	
KC17	4.9	4.98		1406	0.170	3.28	43	61	F	
KC18	5.0	5.00		1406	0.171	3.30	39	55	F	
KC19	5.0	5.01		1406	0.112	3.26	8	20	F	
KC20	5.0	5.03		1408	0.143	3.26	18	33	F	
KC21	5.0	5.03		1406	0.196	3.24	50	71	F	
KC22	5.0	5.16		1407	0.230	3.26	65	89	F	
KC23	5.0	5.07		1407	0.164	3.30	30	47	F	
KC24	5.0	5.07		1408	0.219	3.28	51	74	F	
KC25	5.0	5.02		1407	0.203	3.28	45	66	F	9.1
KD1	5.0	5.70	12 (~24 hr)	1342	0.400	5.92	-8	35	S	0.7
KD2	5.0	4.75		1341	0.322	5.96	9	43	F	1.9
KD3	5.0	4.74		1338	0.251	5.99	-9	17	S	2.3
KD4	5.0	4.74		1337	0.302	5.96	-5	27	S	2.8
KD5	5.0	5.00		1335	0.371	6.00	23	62	F	3.5
KD6	5.0	4.97		1334	0.322	6.00	-4	30	S	4.1
KD7	5.0	5.37		1332	0.451	5.99	34	82	F	5.0
KD8	5.0	5.22		1329	0.397	6.00	6	48	S	5.8
KD9	5.0	4.97		1329	0.346	5.99	-3	33	S	6.5
KD10	5.0	4.97		1329	0.306	5.96	-17	15	S	7.0
KD11	5.0	5.01		1329	0.293	5.99	-13	18	S	7.6
KD12	5.0	5.01		1330	0.392	5.96	23	64	F	8.3

TABLE A-1
EXPERIMENTAL SODIUM BOILING INITIATION DATA

Run (1)	Argon Cover Gas Pressure in Condenser (psia) (2)	Test Section Pressure (psia) (3)	Maximum Test Section Pressure (psia) and time (4)	Test Section Inlet Temperature (°F)	Heat Flux (Btu/hr-ft^2 10^6)	Velocity (ft/sec)	Bulk Superheat (°F)	Wall Superheat (°F) (5)	Type of Trip (6)	Heater Operating Time (min)
KD13	5.0	5.12		1328	0.410	5.96	19	62	F	9.1
KD14	5.0	4.95		1327	0.326	5.94	-7	27	S	9.8
KD15	5.0	4.97		1327	0.304	5.96	-13	19	S	10.3
KD16	5.0	5.40		1332	0.412	5.94	10	54	F	11.0
KD17	5.0	5.92		1332	0.559	5.99	55	115	F	12.0
KD18	5.0	4.90		1328	0.283	5.96	-20	10	S	12.5
KD19	5.0	5.27		1328	0.496	5.96	43	95	F	13.3
KD20	5.0	4.98		1328	0.333	6.35	-10	25	S	13.9
KD21	5.0	4.95		1327	0.281	6.11	-19	11	S	14.6
KD22	5.0	4.95		1332	0.308	5.99	-10	22	S	15.1
KD23	5.0	5.42		1333	0.488	5.96	39	91	F S	16.0
KD24	5.0	4.90		1337	0.266	5.96	-15	13	S	16.5
KD25	5.0	5.27		1335	0.423	5.92	26	71	F S	17.2
KD26	5.0	4.87	8 (~20 hr)	1235	0.408	4.07	-24	19	S	17.9
KD27	5.0	5.15		1235	0.503	4.05	22	75	F	19.0
KD28	5.0	4.90		1236	0.490	4.09	13	65	F	19.8
KD29	5.0	4.94		1237	0.554	4.05	50	109	F	20.9
KD30	5.0	4.91		1238	0.500	4.11	25	78	F	21.9
KD31	5.0	4.90		1240	0.430	4.09	-4	42	S	22.6
KD32	5.0	4.90		1241	0.544	4.05	42	99	P	23.4
KD33	5.0	4.92		1238	0.486	4.07	22	73	F	24.3
KD34	5.0	5.01		1235	0.595	4.03	71	134	F	25.3
KD35	5.0	4.93		1235	0.552	4.03	45	103	F	26.4
KD36	5.0	4.94		1235	0.431	4.01	-19	27	S	27.9
KD37	5.0	4.95		1239	0.522	4.07	27	82	F	28.9
KD38	5.0	4.97		1240	0.463	4.09	-2	47	S	29.8
KD39	5.0	4.97		1241	0.456	4.03	-5	43	S	30.6
KD40	5.0	4.96		1243	0.453	4.07	-1	47	S	31.4
KD41	5.0	4.94		1240	0.466	4.07	-11	38	S	32.2
KD42	5.0	4.91		1239	0.518	4.03	28	83	F	34.1
KD43	5.0	4.93		1240	0.517	4.07	21	75	F	35.1

TABLE A-1
EXPERIMENTAL SODIUM BOILING INITIATION DATA

Run (1)	Argon Cover Gas Pressure in Condenser (psia) (2)	Test Section Pressure (psia) (3)	Maximum Test Section Pressure (psia) and time (4)	Test Section Inlet Temperature (°F)	Heat Flux (Btu/hr-ft^2 10^6)	Velocity (ft/sec)	Bulk Superheat (°F)	Wall Superheat (°F) (5)	Type of Trip (6)	Heater Operating Time (min)
MA1	5.0	5.37	13 (~24 hrs)	1239	0.509	3.22	0	54	F	0.7
MA2	5.0	5.10		1233	0.525	3.26	12	68	F	1.4
MA3	5.0	5.35		1232	0.563	3.26	35	95	F	2.1
MA4	5.0	5.13		1235	0.478	3.22	-1	50	F	2.6
MA5	5.0	5.33		1237	0.513	3.13	25	80	F	3.2
MA6	5.0	5.45		1238	0.596	3.15	43	107	F S	3.9
MA7	5.0	5.10		1237	0.505	3.15	23	77	F	4.5
MA8	5.0	4.97		1237	0.530	3.13	33	89	F	5.1
MA9	5.0	5.06		1237	0.433	3.13	-13	33	F	5.6
MA10	5.0	4.98		1236	0.482	3.13	-5	46	F	6.2
MA11	5.0	5.10		1237	0.509	3.13	25	79	F	6.8
MA12	5.0	5.21		1238	0.571	3.11	52	113	F	7.5
MA13	5.0	5.00		1239	0.513	3.15	40	94	F	8.1
MA14	5.0	4.95		1239	0.440	3.13	-3	44	F	8.6
MA15	5.0	5.04		1237	0.406	3.15	-24	19	F	9.1
MA16	5.0	5.05		1239	0.502	3.11	20	73	F	9.7
MA17	5.0	4.98		1237	0.435	3.13	-16	30	F	10.1
MA18	5.0	5.00		1238	0.497	3.13	20	73	F	10.7
MA19	5.0	5.00		1239	0.496	3.15	24	77	F	11.3
MA20	5.0	5.01		1237	0.503	3.13	27	80	F	11.9
MA21	5.0	5.42	5 (~24 hrs)	1238	0.647	4.03	57	126	F	12.8
MA22	5.0	6.54		1238	0.710	3.98	33	110	F	13.7
MA23	5.0	5.20		1237	0.616	4.07	8	74	F	14.3
MA24	5.0	5.25		1237	0.623	4.07	36	102	F	15.1
MA25	5.0	5.21		1237	0.586	4.09	5	67	F	15.7
MA26	5.0	6.00		1237	0.718	4.03	44	121	F	16.5
MA27	5.0	5.30		1236	0.613	4.09	12	77	F	17.2
MA28	5.0	5.08		1236	0.553	4.07	-9	50	F	17.9

TABLE A-1
EXPERIMENTAL SODIUM BOILING INITIATION DATA

Run (1)	Argon Cover Gas Pressure in Condenser (psia) (2)	Test Section Pressure (psia) (3)	Maximum Test Section Pressure (psia) and time (4)	Test Section Inlet Temperature (°F)	Heat Flux (Btu/hr-ft^2 10^6)	Velocity (ft/sec)	Bulk Superheat (°F)	Wall Superheat (°F) (5)	Type of Trip (6)	Heater Operating Time (min)
NA1	5.0	5.14	6 (~24 hrs)	1226	0.611	4.00	23	76	F	3.6
NA2	5.0	5.00		1228	0.579	4.00	33	79	F	4.3
NA3	5.0	5.00		1227	0.479	3.98	-9	30	S	4.9
NA4	5.0	5.04		1225	0.491	4.00	-11	28	S	5.5
NA5	5.0	5.16		1228	0.720	4.03	80	143	F	6.3
NA6	5.0	5.04		1226	0.568	4.03	17	64	F	7.0
NA7	5.0	5.13		1224	0.641	3.90	40	95	F	7.8
NA8	5.0	5.16		1224	0.739	3.92	83	148	F	8.6
NA9	5.0	5.13		1223	0.681	3.88	46	105	F	9.5
NA10	5.0	5.22		1223	0.748	3.94	85	151	F	10.4
NA11	5.0	5.28	12 (~24 hrs)	1236	0.690	2.91	52	126		
NA12	5.0	5.11		1234	0.521	2.94	5	61		
NA13	5.0	7.61		1233	0.917	2.91	13	114		

APPENDIX 2
COMPARISON OF ALL-LIQUID HEAT TRANSFER CORRELATIONS

The correlations for heat transfer in turbulent flow of liquid metals proposed by Dwyer[17] and by Dwyer and Tu[18] are successful in presenting the Peclet number,* Pe, as a characteristic parameter of the system. Because of their simplified treatment, however, the correlations have introduced an artificial discontinuity in the behavior of the Nusselt number, Nu. This discontinuity is in the derivative of the Nusselt number and is due to the fact that the correlations are either for dominant heat convection or dominant thermal conduction. The location of this discontinuity is not determined by a single dimensionless parameter. A minimum Nusselt number, which is only geometry-dependent, should be observed when thermal convection prevails.

Caution should be exercised in using Dwyer's expressions to assure that the appropriate equation is used for the data range considered. For example, for the tests covered here, the maximum liquid velocity was 6 ft/sec at 1430°F; this value corresponds to a channel Reynolds number of 50,600. As explained below, the use of the conduction expression of Dwyer is required rather than Dwyer's expression for the region where convection effects are significant, i.e., where $Nu = \alpha + \beta(\psi Pe)^{\gamma}$.

For an annulus, it is possible to determine the minimum Reynolds number required for convection effects to be significant,

$$Re_c = \left[\left(\frac{1.82}{Pr}\right)^{0.715} - 4\right]^{1.089} \qquad (576)$$

where Re_c is the channel Reynolds number as solved for from the expression for ψ, (Reference 17), and Pr is the Prandtl number. For the present experiments, Pr = 0.0042 at 1430°F, and Re_c = 60,600. Since this value of channel

*The Peclet number is by definition the product of the Reynolds number times the Prandtl number, i.e., Pe = RePr. In the literature, the Peclet number is sometimes referred to as the thermal Reynolds number,[48] because the thermal diffusivity, α, takes the place of the kinematic viscosity, ν, in the expression for the Reynolds number.

Reynolds number exceeds that corresponding to the maximum velocity conditions (50,600), the conduction region, not the convection region, is appropriate.*

The heat transfer correlations derived by Kays and Leung[19] are more general than those of Dwyer[17,18] not only as far as flow regimes are concerned but also because they are not restricted to liquid metals. In addition, the correlations proposed by Kays and Leung do not possess discontinuous behavior, except at the transition of flow regimes. The discontinuity at the transition of flow regimes is zero at r = 1 (flow between parallel plates), and its magnitude increases with decreasing values of r, as can be inferred from Figure 11 in Reference 19.†

*In analyzing experiments performed previously with the geometry used for the present experiment for similar flow conditions, both Noyes and Lurie[38] and Kosky[15] inappropriately used the Dwyer convection equation.

†The nomenclature used in Reference 19 is not entirely consistent with the nomenclature in the present study.

APPENDIX 3
UNUSUAL SUPERHEAT PATTERN

During the present experimental study, flow, inlet temperature, pressure or heat flux, surface finish, and cold trapping temperature were controlled and superheating occurred in a random manner, as might be expected in an engineering scale loop and/or a reactor system where heterogeneous nucleation can occur at wall cavities as well as at gas bubbles and at oxide or corrosion product particulates. However, one unusual superheat pattern occurred during the K runs.* The K1 to K17 runs were made at heat fluxes of approximately 540,000 Btu/hr-ft^2. The superheating value obtained exhibited a random scatter from 15 to 79°F bulk superheat. Runs K18 and K32 were made two days later at heat fluxes of approximately 740,000 Btu/hr-ft^2 and, as expected, superheating values showed a random scatter, from 25 to 80°F (bulk superheat) for the first nine runs; but then, without any variation in test method or change in controllable parameters, the superheating dropped to -2°F bulk superheat. The next run returned to the normal scatter range with 45°F bulk superheat. The superheating values then dropped to negative bulk superheats for all following runs.

For the next 12 days the heater was left in the flowing sodium in the loop at a temperature of approximately 700°F. Ten additional runs, K33 to K42, were then made with control parameters as close as possible to those of runs K1 to K32. The random scatter superheat values for these additional runs were normal, with a range of 21 to 73°F bulk superheat.

Whatever phenomenon had occurred within runs K27 to K32 had ceased to exist during the 700°F storage for the 12-day interim between tests.

*All of the K runs were made using procedure P.

APPENDIX 4
HEAT LOSS CALIBRATION

The bulk superheat data of Figure 20 permit a determination of the test section heat loss, $(Q/A)_L$. Since zero bulk superheat represents the lowest practical heat flux, the test section heat loss would be most pronounced for these conditions. Inlet subcooling as a function of gross heat flux for zero bulk superheating is shown in Figure 44.

The Figure 44 extrapolation maintains the slope established by the 100, 200, and 300°F inlet subcooling points and, as a result, produces a low test section heat loss (0.02×10^6 Btu/hr-ft^2). This loss closely compares with the heat loss obtained from Equation 4. It is believed that the deviation of the 20°F inlet subcooling point from the curve established by the higher subcoolings is the result of reporting the maximum, not average, values of bulk superheat, as previously explained in Section III. As the difference in indicated bulk superheat between the thermocouples located at the end of the heater generally increased with heat flux, varying from 0 to 45°F, there would be a tendency for the lowest heat fluxes (20°F inlet subcooling) to indicate a somewhat lower bulk superheat then the higher heat fluxes (100 to 300°F inlet subcooling). If this reasoning were applied to Figure 20, the 20°F inlet subcooling curve would shift upward by about 20°F (half of the maximum difference). This, in turn, would move the 20°F inlet subcooling point of Figure 44 to the left.

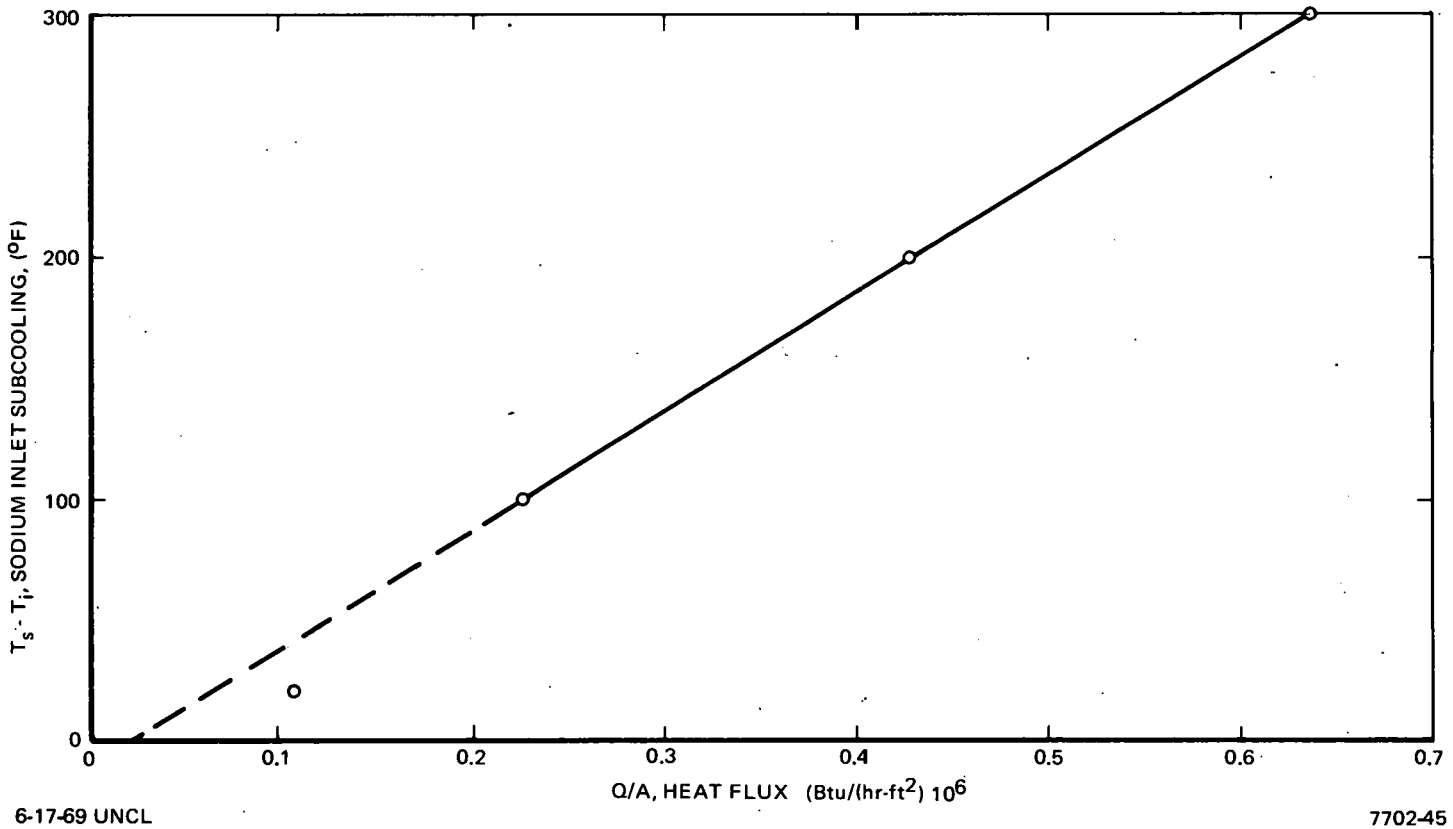

Figure 44. Inlet Subcooling vs Heat Flux for Zero Bulk Superheat

REFERENCES

1. H. K. Fauske, "Liquid Metal Boiling in Relation to LMFBR Safety Design," AIChE, Preprint 17, Tenth National Heat Transfer Conference, August 11-14, 1968

2. C. J. Baroczy, "Pressure Drop for Two-Phase Potassium Flowing Through a Circular Tube and an Orifice," Chem. Eng'g. Prog. Symp., Series No. 82, 64, 1968

3. R. E. Balzhiser, "Investigation of Liquid Metal Boiling Heat Transfer," AFAPL-TR-66-85, January 1967

4. Y. Y. Hsu, "On the Size Range of Active Nucleation Cavities on a Heating Surface," Trans. ASME, Journal of Heat Transfer, 84, p 207 (1962)

5. R. E. Holtz, "The Effect of the Pressure-Temperature History Upon Incipient Boiling Superheats in Liquid Metals," ANL-7184 (1966)

6. J. C. Chen, "Incipient Boiling Superheats in Liquid Metals," Trans. ASME, Journal of Heat Transfer, 90, p 303 (1968)

7. O. E. Dwyer, "On Incipient-Boiling Wall Superheats in Liquid Metals," BNL-13039 (1968)

8. J. Hopenfeld, "Corrosion Studies of Stainless Steel in Flowing Sodium at High Heat Flux," Proceedings of the International Conference on Sodium Technology and Large Fast Reactor Design, November 7-9, 1968, ANL-7520, Part I, p 163 (1968)

9. H. Lurie and R. C. Noyes, "Boiling Studies for Sodium Reactor Safety, Part II Pool Boiling and Initial Forced Convection Tests and Analyses," NAA-SR-9477 (October 1964)

10. H. Lurie, "Steady-State Sodium Boiling and Hydrodynamics," NAA-SR-11586 (January 1966)

11. R. L. Randall and D. Logan, "Application of Noise-Analysis Techniques to Hydraulic Measurements in Liquid-Metal Systems," Proceedings of the Symposium on Liquid Metal Instrumentation and Control, Idaho Falls, Idaho, March 1-2, 1967, ANL-7380

12. D. Logan, R. L. Randall, C. J. Baroczy and J. A. Landoni, "Boiling Liquid Metals and Two-Phase Flow Investigations," Proceedings of the International Conference on the Safety of Fast Reactors, Aix-en-Provence, France, September 19-22, 1967

13. R. L. Randall, "Application of Noise Analysis Techniques to Detection of Incipient Malfunctions," Incipient Failure Diagnosis for Assuring Safety and Availability of Nuclear Power Plants, Gatlinburg, Tennessee, October 30-November 1, 1967, CONF-671011

14. R. E. Holtz and R. M. Singer, "On the Initiation of Pool Boiling in Sodium," AIChE, Preprint No. 15, Tenth National Heat Transfer Conference, Phila., Pa., August 11-14, 1968

15. P. G. Kosky, "Some Aspects of Boiling and Vapor Voidage Growth Problems in a Liquid Metal Cooled Reactor," Proceedings of the International Conference on the Safety of Fast Reactors, Aix-en-Provence, France, September 19-22, 1967

16. G. H. Golden and J. V. Tokar, "Thermophysical Properties of Sodium," ANL-7323 (August 1967)

17. O. E. Dwyer, "On the Transfer of Heat to Fluids Flowing Through Pipes, Annuli, and Parallel Plates," Nucl. Sci. Eng., 17, p 336 (1963)

18. O. E. Dwyer and P. S. Tu, "Unilateral Heat Transfer to Liquid Metals Flowing in Annuli," Nucl. Sci. Eng., 15, p 58 (1963)

19. W. M. Kays and E. Y. Leung, "Heat Transfer in Annular Passages-Hydrodynamically Developed Turbulent Flow With Arbitrarily Prescribed Heat Flux," Int. Jour Heat Mass Transfer, 6, pp 537-557 (1963)

20. J. B. Heineman, "Forced Convection Boiling Sodium Studies at Low Pressure," Proceedings of the Conference on Application of High Temperature Instrumentation to Liquid-Metal Experiments, Argonne, Illinois, September 28-29, 1965, ANL-7100

21. G. C. Pinchera, G. Tomassetti, G. Gambardella and G. Farello, "Experimental Boiling Studies Related to Fast Reactor Safety," International Conference on the Safety of Fast Reactors, Aix-en-Provence, France, September 19-22, 1967

22. G. Grass, H. Kottowski, K. H. Spiller, "Measurement of the Superheating and Studies About Boiling Phenomena in Liquid Metals," International Conference on the Safety of Fast Reactors, Aix-en-Provence, France, September 19-22, 1967

23. P. J. Marto and W. M. Rohsenow, "Nucleate Boiling Instability of Alkali Metals," Journal of Heat Transfer, Trans. ASME, Series C, 88, p 183 (May 1966)

24. G. C. Pinchera, G. Tomassetti, L. Falzetti and G. Fornari, "Sodium Boiling Researches Related to Fast Reactor Safety," ANS Transactions, 11, No. 2, 1968

25. L. Bernath and W. Begell, "Forced-Convection, Local Boiling Heat Transfer in Narrow Annuli," Chem. Eng'g. Prog. Sym. Series, No. 29, 55, 1958

26. "1000-Mwe Liquid Metal Fast Breeder Follow-On Study Conceptual Design Study," AI-AEC-12792, III (1969)

27. R. E. Holtz and R. M. Singer, "On the Superheat of Sodium at Low Heat Fluxes," ANL-7383 (1967)

28. E. J. Davis and G. H. Anderson, "The Incipience of Nucleate Boiling in Forced Convection Flow," AIChE Jour, 12, p 774 (1966)

29. E. S. Sowa, "The Investigation of Sodium Penetration Into 304 Stainless Steel With the Laser Microspectrophotometer," ANS Transactions, 11, No. 2, 1968

30. L. Bernath, Private Communication

31. S. Dushman, "Vacuum Technique," Table 34, p 611, Wiley and Sons, Inc 1949

32. T. Theofanous, L. Biasi, H. S. Isbin and H. Fauske, "A Theoretical Study on Bubble Growth in Constant and Time-Dependent Pressure Fields," ANS Transactions, 11, No. 2, 1968

33. K. T. Claxton, "The Influence of Radiation on the Inception of Boiling in Liquid Sodium," AERE-R 5308 (1967)

34. A. M. Judd, "Sodium Boiling and Fast Reactor Safety Analysis," AEEW-R 561 (1967)

35. J. G. Collier and P. G. Kosky, "Natural Convective Boiling of the Alkaline Metals – A Critical Review," AERE-R 5436 (1967)

36. P. J. Marto and W. M. Rohsenow, "Effects of Surface Conditions on Nucleate Pool Boiling of Sodium," Journal of Heat Transfer, Trans. ASME, Series C, 88, p 196 (May 1966)

37. E. R. G. Eckert and R. M. Drake, Jr., "Heat and Mass Transfer," Appendix of Property Values, 2nd Edition, McGraw-Hill Book Co., 1959

38. R. C. Noyes and H. Lurie, "Boiling Sodium Heat Transfer," 3rd International Heat Transfer Conference, V, Chicago, 1966

39. R. C. Martinelli, Trans. ASME, 69, pp 947-959 (1947)

40. W. H. McAdams, "Heat Transmission," McGraw-Hill Book Co., 1954

41. M. Dalle Donne, "A New and Simple Method of Estimating the Liquid Superheat due to Surface Conditions in Nucleate Boiling and Its Application to Sodium," Nukleonik, Band 8, Heft 3, pp 133-137 (1966)

42. S. S. Kutateladze, V. M. Borishanskii, I. I. Novikov and O. S. Fedynskii, "Liquid-Metal Heat Transfer Media," Chapter 8, Heat Exchange During Free Convection, Consultants Bureau Inc., New York, 1959

43. R. E. Lundberg, W. C. Reynolds and W. M. Kays, "Heat Transfer With Laminar Flow in Concentric Annuli With Constant and Variable Wall Temperature and Heat Flux," NASA TN D-1972 (August 1963)

44. N. Koumoutsos, R. Moissis and A. Spyridonos, "A Study of Bubble Departure in Forced-Convection Boiling," Journal of Heat Transfer, Trans. ASME, Series C, 90, p 223 (May 1968)

45. L. D. Landau and E. M. Lifschitz, "Fluid Mechanics," Pergamon Press, 1959

46. D. B. R. Kenning and M. G. Cooper, "Flow Patterns Near Nuclei and the Initiation of Boiling During Forced Flow Convection Heat Transfer," Paper 11, Proceedings of the Institution of Mechanical Engineers, 1965-1966

47. V. L. Streeter, "Handbook of Fluid Dynamics," Chapter 12, McGraw-Hill Book Co., 1961

48. T. A. Shercliff, "A Textbook of Magnetohydrodynamics," p 42, Pergamon Press, 1965

THIS PAGE

WAS INTENTIONALLY

LEFT BLANK

A	heated surface area (ft^2)
a	radius of bubble (in.)
c	specific heat of liquid (Btu/lb-°F)
D	diameter (in.)
Eu	Euler number (dimensionless)
F	force (lb)
f	friction factor (dimensionless)
g	gravitational acceleration (ft/hr^2)
Gr	Grashof number (dimensionless)
h	heat transfer coefficient (Btu/hr-ft^2-°F)
k	thermal conductivity (Btu/hr-ft-°F)
L	length (ft)
Nu	Nusselt number (dimensionless)
p	absolute pressure (psia)
Pe	Peclet number (dimensionless)
Pr	Prandtl number (dimensionless)
q	specific kinetic energy of flow (lb/ft^2)
Q/A	heat flux (Btu/ft^2-hr)
$r = D_s/D_o$	diameter ratio (dimensionless)
Re	Reynolds number (dimensionless)
$s = D_s/D_o$	diameter ratio (dimensionless)
T	temperature (°F)
u	velocity (ft/sec)
u*	friction velocity (ft/sec)
u+	dimensionless velocity (dimensionless)
W	mass flowrate (lb/hr)
y	distance from wall (in.)
y^+	dimensionless distance (dimensionless)
β	contact angle (dimensionless)
$\varkappa$	thermal diffusivity (ft^2/sec)
μ	dynamic viscosity (lb/ft-hr)
ν	kinematic viscosity (ft^2/sec)
ρ	density (lb/ft^3)
σ	surface tension (lb/ft)
τ	shear stress (lb/ft^2)
$\tau^* = \tau_o/\tau_w$	shear stress ratio (dimensionless)

Subscripts

b	bulk flow
c	channel
d	drag
e	equivalent (diameter)
i	inlet temperature
L	heat loss
l	limiting value
o	outer wall (adiabatic surface)
s	system (saturation)
sp	sphere
t	surface tension
w	inner wall (heated surface)
z	zero shear stress

Atomics International
North American Rockwell